# Proteome profile of peripheral myelin in healthy mice and in a neuropathy model

24 Hills Road, **P** 01223 855346
Cambridge **W** elifesciences.org
CB2 1JP **T** @elife_sciences

FOR PEER REVIEW - CONFIDENTIAL

# Proteome profile of peripheral myelin in healthy mice and in a neuropathy model

Tracking no: 27-08-2019-TR-eLife-51406R2

**Impact statement:** Comprehensive compendium of myelin proteins in the peripheral nervous system and method to address molecular diversity of myelin sheaths in health and disease.

**Competing interests:** No competing interests declared

**Author contributions:**
Sophie Siems: Sophie B. Siems performed all experiments not specified otherwise, conducted statistical analysis, contributed to analysis and interpretation of data. Olaf Jahn: Olaf Jahn performed proteome analysis, contributed to analysis and interpretation of data. Maria Eichel: Maria A. Eichel performed teased fiber labeling and microscopy. Nirmal Kannaiyan: Nirmal Kannaiyan performed bioinformatic analysis of RNA-Seq data. Lai Man Wu: Lai Man N. Wu performed histological analysis. Diane Sherman: Diane L. Sherman performed histological analysis. Kathrin Kusch: Kathrin Kusch provided unpublished reagents. Dörte Hesse: Dörte Hesse contributed to proteome analysis. Ramona Jung: Ramona B. Jung performed biochemical purification of myelin. Robert Fledrich: Robert Fledrich provided an unpublished RNA-Seq dataset. Michael Sereda: Michael W. Sereda provided an unpublished RNA-Seq dataset. Moritz Rossner: Moritz J. Rossner supervised bioinformatic analysis of RNA-Seq data. Peter Brophy: Peter J. Brophy supervised histological analysis. Hauke Werner: Hauke B. Werner conceived, designed and directed the study, analyzed and interpreted data and wrote the article.

**Funding:**
Deutsche Forschungsgemeinschaft (DFG): Hauke B. Werner, WE 2720/2-2; Deutsche Forschungsgemeinschaft (DFG): Hauke B. Werner, WE 2720/4-1; Deutsche Forschungsgemeinschaft (DFG): Hauke B. Werner, WE 2720/5-1; Deutsche Forschungsgemeinschaft (DFG): Moritz J. Rossner, RO 4076/3-2; Wellcome: Peter Brophy, 0842424 The funders had no role in study design, data collection and interpretation, or the decision to submit the work for publication.

**Data Availability:**
All data generated or analysed during this study are included in the manuscript and supporting files. This includes the mass spectrometry proteomics data. Source data files have been provided for Figures 1, 3 and 5. Additional to being provided in the source data files, mass spectrometry proteomics data have been deposited to the PRIDE/ProteomeXchange Consortium with dataset identifier PXD015960 and are available to the reviewers. Please use username: reviewer94825@ebi.ac.uk and password: C5r5SVMi. Upon acceptance of the manuscript, we will notify PRIDE support to make the dataset publicly available.
N/A

**Ethics:**
Human Subjects: No Animal Subjects: Yes Ethics Statement: All animal work conformed to United Kingdom legislation (Scientific Procedures) Act 1986 and to the University of Edinburgh Ethical Review Committee policy; Home Office project license No. P0F4A25E9.

**Information for reviewers (full submissions):**

eLife aims to publish work of the highest scientific standards and importance in all areas of the life and biomedical sciences, from the most basic and theoretical work through to translational, applied and clinical research. Articles must be methodologically and scientifically rigorous, ethically conducted, and objectively presented according to the appropriate community standards.

You will be asked for a general assessment and a summary of any major concerns (ideally in fewer than 500 words), as well as a list of any minor comments (optional). You will also have the opportunity to comment on the statistical rigour of the work (optional).

In your general assessment, please articulate what is exciting and whether the work represents a significant contribution. Please note our guidelines about requests for additional work:

1. We will only request new work, such as experiments, analyses, or data collection, if the new data are essential to support the major conclusions. The authors must be able to do any new work in a reasonable time frame (additional work should be conducted and written up within two months); otherwise, we will usually reject the manuscript.
2. Any requests for new work must fall within the scope of the current submission and the technical expertise of the authors.

Our goal is to make peer review constructive and collaborative: after the reviews have been submitted independently, there is an online discussion between the reviewers in which each reviewer will see the identity of the other reviewers.

***TOOLS AND RESOURCES***
*eLife-51406R2*

# Proteome profile of peripheral myelin in healthy mice and in a neuropathy model

Sophie B. Siems[1,7], Olaf Jahn[2,7], Maria A. Eichel[1], Nirmal Kannaiyan[3], Lai Man N. Wu[4], Diane L. Sherman[4], Kathrin Kusch[1], Dörte Hesse[2], Ramona B. Jung[1], Robert Fledrich[1,5], Michael W. Sereda[1,6], Moritz J. Rossner[3], Peter J. Brophy[4], Hauke B. Werner[1,*]

**Affiliations**
[1]Department of Neurogenetics, Max Planck Institute of Experimental Medicine, 37075 Göttingen, Germany
[2]Proteomics Group, Max Planck Institute of Experimental Medicine, 37075 Göttingen, Germany
[3]Department of Psychiatry and Psychotherapy, University Hospital, LMU Munich, 80336 Munich, Germany
[4]Centre for Discovery Brain Sciences, University of Edinburgh, Edinburgh, EH16 4SB, UK
[5]Institute of Anatomy, University of Leipzig, 04103 Leipzig, Germany
[6]Department of Clinical Neurophysiology, University Medical Center, 37075 Göttingen, Germany
[7]These authors contributed equally to this work

*** Corresponding author**
Dr. Hauke Werner
Max Planck Institute of Experimental Medicine
Department of Neurogenetics
Hermann-Rein-Str. 3
D-37075 Göttingen, Germany
Tel.: +49 (551) 3899-759; Fax.: +49 (551) 3899-758
E-mail: Hauke@em.mpg.de

**Key words**
Schwann cell, peripheral nervous system (PNS), myelin proteome, neuropathy, Charcot-Marie-Tooth disease (CMT4F), periaxin (PRX), MCT1/SLC16A1, demyelination, axon degeneration, transcriptome

**Word and figure count**
Abstract 149 words; Introduction/results/discussion 4786 words
6 main figures; 2 figure supplements; 2 main tables; 4 source data files

**ABSTRACT**

Proteome and transcriptome analyses aim at comprehending the molecular profiles of the brain, its cell-types and subcellular compartments including myelin. Despite the relevance of the peripheral nervous system for normal sensory and motor capabilities, analogous approaches to peripheral nerves and peripheral myelin have fallen behind evolving technical standards. Here we assess the peripheral myelin proteome by gel-free, label-free mass-spectrometry for deep quantitative coverage. Integration with RNA-Sequencing-based developmental mRNA-abundance profiles and neuropathy disease genes illustrates the utility of this resource. Notably, the periaxin-deficient mouse model of the neuropathy Charcot-Marie-Tooth 4F displays a highly pathological myelin proteome profile, exemplified by the discovery of reduced levels of the monocarboxylate transporter MCT1/SLC16A1 as a novel facet of the neuropathology. This work provides the most comprehensive proteome resource thus far to approach development, function and pathology of peripheral myelin, and a straightforward, accurate and sensitive workflow to address myelin diversity in health and disease.

## INTRODUCTION

The ensheathment of axons with myelin enables rapid impulse propagation, a prerequisite for normal motor and sensory capabilities of vertebrates (1,2). This is illustrated by demyelinating neuropathies of the Charcot-Marie-Tooth (CMT) spectrum, in which mutations affecting myelin genes as *MPZ, PMP22, GJB1* and *PRX* impair myelin integrity and reduce the velocity of nerve conduction in the peripheral nervous system (PNS) (3). Developmentally, myelination by Schwann cells in peripheral nerves is regulated by axonal neuregulin-1 (4,5) and the basal lamina (6–8) that is molecularly linked to the abaxonal Schwann cell membrane via integrins and the dystroglycan complex (9–12). In adulthood, the basal lamina continues to enclose all axon/myelin-units (13), probably to maintain myelin. Beyond regulation by extracellular cues, myelination involves multiple proteins mediating radial sorting of axons out of Remak bundles, myelin membrane growth and layer compaction (14–18). For example, the Ig-domain containing myelin protein zero (MPZ; also termed P0) mediates adhesion between adjacent extracellular membrane surfaces in compact myelin (19). At their intracellular surfaces, myelin membranes are compacted by the cytosolic domain of MPZ/P0 together with myelin basic protein (MBP; previously termed P1) (20,21). Not surprisingly, MPZ/P0 and MBP were early identified as the most abundant peripheral myelin proteins (22,23).

A system of cytoplasmic channels through the otherwise compacted myelin sheath remains non-compacted throughout life, i.e. the adaxonal myelin layer, paranodal loops, Schmidt-Lanterman incisures (SLI), and abaxonal longitudinal and transverse bands of cytoplasm termed bands of Cajal (14,24,25). Non-compacted myelin comprises cytoplasm, cytoskeletal elements, vesicles and lipid-modifying enzymes, and thus numerous proteins involved in maintaining the myelin sheath. The cytosolic channels probably also represent transport routes toward Schwann cell-dependent metabolic support of myelinated axons (26–31).

Considering that Schwann cells constitute a major proportion of the cells in the PNS, oligonucleotide microarray analyses have been used for mRNA abundance profiling of total sciatic nerves (32,33). Indeed, these systematic approaches allowed the identification of novel myelin constituents including non-compact myelin-associated protein (NCMAP/MP11) (34). Notwithstanding that the number of known peripheral myelin proteins has grown in recent years, a comprehensive molecular inventory has been difficult to achieve because applications of systematic ('omics') approaches specifically to Schwann cells and peripheral myelin remained comparatively scarce, different from studies addressing oligodendrocytes and CNS myelin (35–40). One main reason may be that the available techniques were not

sufficiently straightforward for general application. For example, the protein composition of peripheral myelin was previously assessed by proteome analysis (41). However, at that time the workflow of sample preparation and data acquisition (schematically depicted in **Figure 1A**) was very labor-intense and required a substantial amount of input material; yet the depth of the resulting datasets remained limited. In particular, differential myelin proteome analysis by 2-dimensional fluorescence intensity gel electrophoresis (2D-DIGE) requires considerable hands-on-time and technical expertise (41,42). While this method is powerful for the separation of proteoforms (43), it typically suffers from under-representation of highly basic and transmembrane proteins. It thus allows comparing the abundance of only few myelin proteins rather than quantitatively covering the entire myelin proteome. Because of these limitations and an only modest sample-to-sample reproducibility, 2D-DIGE analysis of myelin, although unbiased, has not been commonly applied beyond specialized laboratories.

The aim of the present study was to establish a straightforward and readily applicable workflow to facilitate both comprehensive knowledge about the protein composition of peripheral myelin and systematic assessment of differences between two states, e.g., pathological alterations in a neuropathy model. The major prerequisites were the biochemical purification of myelin, its solubilization with the detergent ASB-14 and the subsequent automated digestion with trypsin during filter-aided sample preparation (FASP). The tryptic peptides were fractionated by liquid chromatography and analyzed by mass spectrometry for gel-free, label-free quantitative proteome analysis. More specifically, we used nano-flow ultra-performance liquid chromatography (nanoUPLC) coupled to an electrospray-ionization quadrupole time-of-flight (ESI-QTOF) mass spectrometer with ion mobility option, providing an orthogonal dimension of peptide separation. The utilized data-independent acquisition (DIA) strategy relies on collecting data in an alternating low and elevated energy mode ($MS^E$); it enables simultaneous sequencing and quantification of all peptides entering the mass spectrometer without prior precursor selection (reviewed in (44,45)). With their high-duty cycle utilized for the acquisition of precursor ions, $MS^E$-type methods are ideally suited to reliably quantify proteins based on peptide intensities. Notably, these methods do not involve the use of spectral libraries in the identification of proteins, different from other DIA strategies. Instead, the achieved high-complexity fragmentation spectra are deconvoluted before submission to dedicated search engines for peptide and protein identification (46,47). In the $MS^E$ mode, this deconvolution involves precursor-fragment ion alignment solely on the basis of chromatographic elution profiles; on top, drift times of ion mobility-separated precursors are used in the high-definition (HD)$MS^E$ mode. An expansion of the latter referred to as the ultra-definition (UD)$MS^E$ mode, additionally implements drift time-dependent collision energy profiles for more effective precursor fragmentation (48,49).

Indeed, compared to the previously used manual handling and in-gel digestion, the current workflow (schematically depicted in **Figure 1A)** is considerably less labor-intense, and automated FASP increases sample-to-sample reproducibility. Moreover, differential analysis by quantitative mass spectrometry (MS) facilitates reproducible quantification of hundreds rather than a few distinct myelin proteins. Together, the present workflow increases the efficacy of assessing the peripheral myelin proteome while shifting the main workload from manual sample preparation and gel-separation to automated acquisition and processing of data. We propose that comprehending the expression profiles of all myelin proteins in the healthy PNS and in myelin-related disorders can contribute to advancing our understanding of the physiology and pathophysiology of peripheral nerves.

## RESULTS

### Purification of peripheral myelin

We biochemically enriched myelin as a light-weight membrane fraction from pools of sciatic nerves dissected from mice at postnatal day 21 (P21) using an established protocol of discontinuous sucrose density gradient centrifugation (41,50), in which myelin membranes accumulate at the interface between 0.29 and 0.85 M sucrose. By immunoblotting, proteins specific for both compact (MPZ/P0, MBP, PMP2) and non-compact (PRX) myelin were substantially enriched in the myelin fraction compared to nerve lysates (**Figure 1B**). Conversely, axonal (NEFH, KCNA1) and mitochondrial (VDAC) proteins and a marker for the Schwann cell nucleus (KROX20/EGR2) were strongly reduced in purified myelin. Together, these results imply that biochemically purified peripheral myelin is suitable for systematic analysis of its protein composition.

### Proteome analysis of peripheral myelin

It has long been difficult to accurately quantify the most abundant myelin proteins both in the CNS (PLP, MBP, CNP (51)) and the PNS (MPZ/P0, MBP, PRX; this work), probably owing to their exceptionally high relative abundance. For example, the major CNS myelin constituents PLP, MBP and CNP comprise 17, 8 and 4% of the total myelin protein, respectively (51). We have recently provided proof of principle (52) that the mass spectrometric quantification of these high-abundant myelin proteins is accurate and precise when data are acquired in the $MS^E$ data acquisition mode and proteins are quantified according to the TOP3 method, i.e. if their abundance values are obtained based on the proven correlation between the average intensity of the three peptides exhibiting the most intense mass spectrometry response and the absolute amount of their source protein (53,54). Using data acquisition by $MS^E$ we confirmed that CNP constitutes about 4% of the total CNS myelin proteome and that the abundance of CNP in myelin from mice heterozygous for the *Cnp* gene ($Cnp^{WT/null}$) compared to wild-type mice is 50.7% (±0.4%), in agreement with the halved gene dosage and gel-based quantification by silver staining or immunoblotting (52).

When applying the $MS^E$ mode to PNS myelin, we quantified 351 proteins with a false discovery rate (FDR) of <1% at peptide and protein level and an average sequence coverage of 35.5% (**Figure 1-source data 1**). While $MS^E$ (labeled in orange in **Figure 1C**) indeed provided a dynamic range of more than four orders of magnitude and thus quantitatively covered the exceptionally abundant myelin proteins MPZ/P0, MBP and PRX, the number of quantified proteins appeared limited when spectral complexity was deconvoluted solely on the basis of chromatographic elution profiles. Accordingly, by using the $UDMS^E$ mode, which

comprises ion mobility for additional peptide separation as well as drift time-specific collision energies for peptide fragmentation, proteome coverage was increased about three-fold (1078 proteins quantified; average sequence coverage 34.3%; **Figure 1-source data 1**). However, the dynamic range of UDMS$^E$ (labeled in blue in **Figure 1C**) was found to be somewhat compressed compared to that of MS$^E$, which can be considered an expectable feature of traveling wave ion mobility devices (55), where the analysis of pulsed ion packages leads to a temporal and spatial binning of peptides during ion mobility separation. Indeed, this manifests as a ceiling effect for the detection of exceptionally intense peptide signals, which results in an underestimation of the relative abundance of MPZ/P0, MBP and PRX by UDMS$^E$.

The complementary nature of the MS$^E$ and UDMS$^E$ data acquisition modes led us to conclude that a comprehensive analysis of the myelin proteome that facilitates both correct quantification of the most abundant proteins and deep quantitative coverage of the proteome would require analyzing the same set of samples with two different instrument settings for MS$^E$ and UDMS$^E$, respectively. Considering that instrument time is a bottleneck for the routine differential proteome analysis of myelin from mutant mice, we aimed to combine the strengths of MS$^E$ and UDMS$^E$ into a single data acquisition mode. Based on a gene ontology enrichment analysis for cellular components of the 200 proteins of highest and lowest abundance from the UDMS$^E$ dataset, we realized that the ‘bottom‘ of the quantified proteome is probably largely unrelated to myelin but dominated by contaminants from other subcellular sources including mitochondria. We thus reasoned that for a myelin-directed data acquisition mode, proteome depth may be traded in for a gain in dynamic range and devised a novel method referred to as dynamic range enhancement (DRE)-UDMS$^E$, in which a deflection lens is used to cycle between full and reduced ion transmission during mass spectrometric scanning. Indeed, DRE-UDMS$^E$ quantified an intermediate number of proteins in PNS myelin (554 proteins; average sequence coverage 30.6%; **Figure 1-source data 1**) while providing an intermediate dynamic range (labeled in green in **Figure 1C**). We thus consider DRE-UDMS$^E$ as the data acquisition mode of choice most suitable for routine differential myelin proteome profiling (see below).

Overall, we found a high reproducibility between replicates and even among the different data acquisition modes as indicated by Pearson’s correlation coefficients for protein abundance in the range of 0.765-0.997 (**Figure 1-supplement 1**). When comparing the proteins identified in PNS myelin using the three data acquisition modes, we found a very high overlap (**Figure 1D**). We also found a high overlap (**Figure 1E**) between the proteins identified in the present study by UDMS$^E$ and those detected in previous proteomic

approaches to PNS myelin (41,42), thus allowing a high level of confidence. Together, the three data acquisition modes exhibit distinct strengths in the efficient quantification of exceptionally abundant proteins ($MS^E$), establishing a comprehensive inventory ($UDMS^E$) and gel-free, label-free differential analysis of hundreds of distinct proteins (DRE-$UDMS^E$) in peripheral myelin (see **Figure 1A**). Yet, analyzing the same set of samples by different modes may not always be feasible in all routine applications when considering required instrument time.

**Relative abundance of peripheral myelin proteins**

Considering that $MS^E$ provides the high dynamic range required for the quantification of the most abundant myelin proteins, we calculated the relative abundance of the 351 proteins identified in myelin by $MS^E$ (**Figure 1-source data 1**). According to quantitative assessment of this dataset, the most abundant PNS myelin protein, myelin protein zero (MPZ/P0), constitutes 44% (+/-4% relative standard deviation (RSD)) of the total myelin protein (**Figure 2**). Myelin basic protein (MBP), periaxin (PRX) and tetraspanin-29 (CD9) constitute 18% (+/-1% RSD), 15% (+/-1%) and 1% (+/-0.2%) of the total myelin protein, respectively (**Figure 2**). For MPZ/P0 and MBP, our quantification by $MS^E$ is in agreement with but specifies prior estimations upon gel-separation and protein labeling by Sudan-Black, Fast-Green or Coomassie-Blue, in which they were judged to constitute 45–70% and 2–26% of the total myelin protein, respectively (22,56–58). However, gel-based estimates of the relative abundance of myelin proteins were not very precise with respect to many other proteins, including those of high molecular weight. Indeed, periaxin was identified as a constituent of peripheral myelin after the advent of gradient SDS-PAGE gels (59), which allowed improved migration of large proteins into gels. The present $MS^E$-based quantification of myelin proteins also extends beyond and partially adjusts an earlier mass spectrometric approach (41). Indeed, the current approach identified and quantified more myelin proteins, probably owing to improved protein solubilization during sample preparation and higher dynamic range of the used mass spectrometer. By $MS^E$, known myelin proteins (**Table 1**) collectively constitute over 85% of the total myelin protein (**Figure 2**) while proteins not yet associated with myelin account for the remaining 15% of the total myelin protein.

**Comprehensive compendium and comparison to the transcriptome**

To systematically elucidate the developmental abundance profiles of the transcripts that encode peripheral myelin proteins (**Figure 3**), we used our combined proteome inventory of peripheral myelin (**Figure 1-source data 1**) to filter mRNA abundance data of all genes expressed in sciatic nerves. By this strategy, **Figure 3** displays only those transcripts of which the protein product was identified in peripheral myelin rather than all transcripts in the

nerve, thereby discriminating myelin-related mRNAs from other mRNAs such as those present in peripheral axons, fibroblasts, immune cells etc. In this assessment we additionally included PMP22 although it was not detected by MS as well as 45 proteins exclusively identified by LC-MS of myelin separated by SDS-PAGE (**Figure 1-source data 1**). For mRNA abundance profiles, we exploited a recently established RNA sequencing analysis (RNA-Seq; platform Illumina HiSeq 2000) of sciatic nerves dissected form wild type Sprague Dawley rats at embryonic day 21 (E21), P6, P18 and 6 months (60). RNA-Seq provides reliable information about the relative abundance of all significantly expressed genes and is thus not limited to those represented on the previously used oligonucleotide microarrays (41). The raw data (accessible under GEO accession number GSE115930) were normalized (**Figure 3-source data 1**) and standardized. When comparing the proteome and transcriptome datasets, significant mRNA abundance was detected for all 1046 transcripts for which an unambiguous unique gene identifier was found (**Figure 3**). 126 transcripts displayed developmentally unchanged abundance levels, i.e., abundance changes below a threshold of 10% coefficient of variation (**Figure 3B; Figure 3-source data 1**).

By fuzzy c-means clustering, those 920 transcripts that showed developmental abundance changes were grouped into 5 clusters (**Figure 3A; Figure 3-source data 1**). Among those, one cluster corresponds to an mRNA-abundance peak coinciding with an early phase of myelin biogenesis (cluster ‘P6-UP‘), which includes the highest proportion of known myelin proteins (**Table 1**) such as MPZ/P0, MBP, PRX, cyclic nucleotide phosphodiesterase (CNP), fatty acid synthase (FASN), myelin-associated glycoprotein (MAG), proteolipid protein (PLP/DM20), cell adhesion molecule-4 (CADM4/NECL4), connexin-29 (GJC3), claudin-19 (CLDN19) and CKLF-like MARVEL-transmembrane domain containing protein-5 (CMTM5). However, many known myelin proteins clustered together according to their mRNA-abundance peak coinciding with a later phase of myelination (cluster ‘P18-UP‘), including peripheral myelin protein 2 (PMP2), tetraspanin-29 (CD9), tetraspanin-28 (CD81), connexin-32 (GJB1), plasmolipin (PLLP), junctional adhesion molecule-3 (JAM3), CD59 and dystrophin-related protein-2 (DRP2). The proportion of known myelin proteins was lower in the clusters corresponding to mRNA-abundance peaks in adulthood (clusters ‘late-UP‘, ‘U-shaped‘). Yet, a considerable number of transcripts displayed abundance peaks at the embryonic time-point (cluster ‘Descending‘), including carbonic anhydrase 2 (CA2), cofilin-1 CFL1), tubulin beta-4 (TUBB4b) and band 4.1-protein B (EPB41L3). Generalized, the clusters were roughly similar when comparing previous oligonucleotide microarray analysis of mouse sciatic nerves (41) and the RNA-Seq analysis of rat sciatic nerves (this study); yet, the latter provides information on a larger number of genes and with a higher level of

confidence. Together, clustering of mRNA abundance profiles allows categorizing peripheral myelin proteins into developmentally co-regulated groups.

When systematically assessing the proteins identified in myelin by gene ontology (GO)-term analysis, the functional categories over-represented in the entire myelin proteome included cell adhesion, cytoskeleton and extracellular matrix (labeled in turquoise in **Figure 4**). When analyzing the clusters of developmentally co-expressed transcripts (from **Figure 3**), proteins associated with the lipid metabolism were particularly enriched in the P6-UP and P18-UP clusters, while those associated with the extracellular matrix (ECM) were over-represented in the U-shaped and Descending clusters (**Figure 4**). For comparison, known myelin proteins (**Table 1**) were over-represented in the P6-UP and P18-UP clusters (**Figure 4**). Together, our proteome dataset provides comprehensive in-depth coverage of the protein constituents of peripheral myelin purified from the sciatic nerves of wild type mice, and comparison to the transcriptome allows identifying developmentally co-regulated and functional groups of myelin proteins. Our data thus supply a solid resource for the molecular characterization of myelin and for discovering functionally relevant myelin proteins.

**Neuropathy genes encoding myelin proteins**

Heritable neuropathies can be caused by mutations affecting genes preferentially expressed in neurons, Schwann cells or both (3,61–63). To systematically assess which neuropathy-causing genes encode peripheral myelin proteins, we compared our myelin proteome dataset with a current overview about disease genes at the NIH National Library of Medicine at https://ghr.nlm.nih.gov/condition/charcot-marie-tooth-disease#genes. Indeed, 31 myelin proteins were identified to be encoded by a proven neuropathy gene (**Table 2**), a considerable increase compared to eight disease genes found in a similar previous approach (41). Notably, this increase is owing to both the larger size of the current myelin proteome dataset (**Figure 1E**) and the recent discovery of numerous neuropathy genes by the widespread application of next generation sequencing.

**Pathological proteomic profile of peripheral myelin in a neuropathy model**

The results presented thus far were based on analyzing myelin of healthy wild type mice; yet we also sought to establish a straightforward method to systematically assess myelin diversity, as exemplified by alterations in a pathological situation. As a model we chose mice carrying a homozygous deletion of the periaxin gene (*Prx*$^{-/-}$) (26,64). Periaxin (PRX) is the third-most abundant peripheral myelin protein (**Figure 2**) and scaffolds the dystroglycan complex in Schwann cells. *Prx*$^{-/-}$ mice represent an established model of Charcot-Marie-Tooth disease type 4F (65–67). Aiming to assess the myelin proteome, we purified myelin

from pools of sciatic nerves dissected from *Prx*$^{-/-}$ and control mice at P21. Upon SDS-PAGE separation and silver staining the band patterns appeared roughly similar (**Figure 5A**), with the most obvious exception of the absence of the high-molecular weight band constituted by periaxin in *Prx*$^{-/-}$ myelin. Yet, several other bands also displayed genotype-dependent differences in intensity. As expected, PRX was also undetectable by MS$^{E}$ in *Prx*$^{-/-}$ myelin, in which most of the total myelin protein was constituted by MPZ/P0 and MBP (**Figure 5B; Figure 5-source data 1**).

Upon differential analysis by DRE-UDMS$^{E}$ (**Figure 5-source data 2**), multiple proteins displayed genotype-dependent differences as visualized in a heatmap displaying those 40 proteins of which the abundance was reduced or increased with the highest statistical significance in *Prx*$^{-/-}$ compared to control myelin (**Figure 5C**). For example, the abundance of the periaxin-associated dystrophin-related protein 2 (DRP2) was strongly reduced in *Prx*$^{-/-}$ myelin, as previously shown by immunoblotting (9). Notably, the abundance of multiple other proteins was also significantly reduced in *Prx*$^{-/-}$ myelin, including the extracellular matrix protein laminin C1 (LAMC1; previously termed LAMB2), the laminin-associated protein nidogen (NID1), Ig-like cell adhesion molecules (CADM4, MAG), the desmosomal junction protein desmin (DES), cytoskeletal and cytoskeleton-associated proteins (EPB41L3, MAP1A, CORO1A, SPTBN1, various microtubular and intermediate filament monomers), the monocarboxylate transporter MCT1 (also termed SLC16A1) and the MCT1-associated (68) immunoglobulin superfamily protein basigin (BSG, also termed CD147). On the other hand, proteins displaying the strongest abundance increase in *Prx*$^{-/-}$ myelin included immune-related proteins (LGALS3, LYZ2, CTSD), cytoskeletal and cytoskeleton-associated proteins (CAPG, CORO1C, CNN3, several myosin heavy chain subunits), peroxisomal enzymes (CAT, HSD17B4, MDH1) and known myelin proteins (PLLP/plasmolipin, CRYAB, GJB1/CX32). For comparison, the abundance of the marker proteolipid protein (PLP/DM20) (69) and the periaxin-associated integrin beta-4 (ITGB4) (12) in myelin was unaltered in *Prx*$^{-/-}$ myelin. Together, differential proteome analysis finds considerably more proteins and protein groups to be altered in *Prx*$^{-/-}$ myelin than previously known (**Figure 5C, D-D‘‘‘**), probably reflecting the complex pathology observed in this model (26,64).

The monocarboxylate transporter MCT1/SLC16A1 expressed by myelinating oligodendrocytes (70,71) and Schwann cells (28,72) has been proposed to supply lactate or other glucose breakdown products to axons, in which they may serve as substrate for the mitochondrial production of ATP (73–75). In this respect it was striking to find the abundance of MCT1 significantly reduced in peripheral myelin when PRX is lacking (**Figure 5C**), a result that we were able to confirm by immunoblotting (**Figure 5E**) and immunolabeling of teased

374 fiber preparations of sciatic nerves (**Figure 5F**). Notably, reduced expression of MCT1 in
375 *Slc16a1*$^{+/-}$ mice impairs axonal integrity at least in the CNS (70,76). The reduced abundance
376 of MCT1 thus represents an interesting novel facet of the complex pathology in *Prx*$^{-/-}$ mice.
377 Considering that the integrity of peripheral axons may be impaired in *Prx*$^{-/-}$ mice, we
378 assessed their quadriceps nerves. Indeed, *Prx*$^{-/-}$ mice displayed reduced axonal diameters, a
379 progressively reduced total number of axons and a considerable number of myelin whorls
380 lacking a visible axon (**Figure 6**), indicative of impaired axonal integrity (77). Yet we note that
381 molecular or neuropathological features other than the reduced abundance of MCT1
382 probably also contribute to the axonopathy in *Prx*$^{-/-}$ mice.
383
384 Together, gel-free, label free proteome analysis provides a cost- and time-efficient method
385 that provides an accurate, sensitive tool to gain systematic insight into the protein
386 composition of healthy peripheral myelin and its alterations in pathological situations. Indeed,
387 gel-free proteome analysis is particularly powerful and comprehensive compared to 2D-
388 DIGE; the workflow presented here appears readily applicable to other neuropathy models,
389 thereby promising discovery of relevant novel features of their neuropathology.
390
391

## DISCUSSION

We used gel-free, label-free quantitative mass spectrometry to assess the protein composition of myelin biochemically purified from the sciatic nerves of wild-type mice, thereby establishing a straightforward and readily applicable workflow to approach the peripheral myelin proteome. The key to comprehensiveness was to combine the strengths of three data acquisition modes, i.e., $MS^E$ for correct quantification of high-abundant proteins, $UDMS^E$ for deep quantitative proteome coverage including low-abundant proteins and DRE-$UDMS^E$ for differential analysis. We suggest that DRE-$UDMS^E$ provides a good compromise between dynamic range, identification rate and instrument run time for routine differential myelin proteome profiling as a prerequisite for a molecular understanding of myelin (patho)biology. We have also integrated the resulting compendium with RNA-Seq-based mRNA abundance profiles in peripheral nerves and neuropathy disease loci. Beyond providing the largest peripheral myelin proteome dataset thus far, the workflow is appropriate to serve as starting point for assessing relevant variations of myelin protein composition, e.g., in different nerves, ages, species and in pathological conditions. The identification of numerous pathological alterations of myelin protein composition in the *Prx*$^{-/-}$ neuropathy model indicates that the method is well suited to assess such diversity.

Aiming to understand nervous system function at the molecular level, multiple 'omics'-scale projects assess the spatio-temporal expression profiles of all mRNAs and proteins in the CNS including oligodendrocytes and myelin (35–39). Yet, peripheral nerves are also essential for normal sensory and motor capabilities. Prior approaches to the molecular profiles of Schwann cells and PNS myelin thus far, however, were performed >8 years ago (32–34,41,78–80), and the techniques have considerably advanced since. For example, current gel-free, label-free mass spectrometry can simultaneously identify and quantify the vast majority of proteins in a sample, thereby providing comprehensive in depth-information. Moreover, RNA-Seq technology has overcome limitations of the previously used microarrays for characterizing mRNA abundance profiles with respect to the number of represented genes and the suitability of the oligonucleotide probes. The present compendium thus provides high confidence with respect to the identification of myelin proteins, their relative abundance and their developmental mRNA expression profiles. This view is supported by the finding that over 80% of the total myelin proteome is constituted by approximately 50 previously known myelin proteins. We believe that the majority of the other identified proteins represent low-abundant myelin-associated constituents in line with the high efficiency of biochemical myelin purification. Doubtless, however, the myelin proteome also comprises

contaminants from other cellular sources, underscoring the need of independent validation for establishing newly identified constituents as true myelin proteins.

Do myelin proteins exist that escape identification by standard proteomic approaches? Indeed, some proteins display atypically distributed lysine and arginine residues, which represent the cleavage sites of the commonly used protease trypsin. The tryptic digest of these proteins leads to peptides that are not well suited for chromatographic separation and/or mass spectrometric detection/sequencing, as exemplified by the small hydrophobic tetraspan-transmembrane myelin proteins MAL (81) and PMP22 (82). We can thus not exclude that additional proteins with atypical tryptic digest patterns exist in peripheral myelin, which would need to be addressed by the use of alternative proteases. Moreover, potent signaling molecules including erbB receptor tyrosine kinases (83,84) and G-protein coupled receptors (GPRs) (85–87) display exceptionally low abundance. Such proteins may be identified when applying less stringent identification criteria, e.g., by requiring the sequencing of only one unique peptide per protein. However, lower stringency would also result in identifying false-positive proteins, which we wished to avoid for the purpose of the present compendium. We note that a truly comprehensive spatio-temporally resolved myelin proteome should preferentially also include systematic information about protein isoforms and post-translational modifications, which still poses technical challenges.

Mutations affecting the periaxin (*PRX*) gene in humans cause CMT type 4F (65,88–90); the neuropathology resulting from mutations affecting periaxin has been mainly investigated in the *Prx*$^{-/-}$ mouse model. Indeed, *Prx*$^{-/-}$ mice display a progressive peripheral neuropathy including axon/myelin-units with abnormal myelin thickness, demyelination, tomaculae, onion bulbs, reduced nerve conduction velocity (64), reduced abundance and mislocalization of the periaxin-associated DRP2 (9) and reduced internode length (26). Absence of SLIs (64) and bands of Cajal (26) imply that the non-compact myelin compartments are impaired when PRX is lacking. In the differential analysis of myelin purified from *Prx*$^{-/-}$ and control mice we find that the previously reported reduced abundance of DRP2 (9) represents one of the strongest molecular changes in the myelin proteome when PRX is lacking. Notably, the reported morphological changes in this neuropathy model (9,26,64) go along with alterations affecting the abundance of multiple other myelin-associated proteins, including junctional, cytoskeletal, extracellular matrix and immune-related proteins as well as lipid-modifying enzymes. Thus, the neuropathology in *Prx*$^{-/-}$ mice at the molecular level is more complex than previously anticipated. It is striking that the abundance of the monocarboxylate transporter MCT1/SLC16A1 that may contribute to the metabolic supply of lactate from myelinating cells to axons (27–31) is strongly reduced in *Prx*$^{-/-}$ myelin. Considering that

MCT1 in Schwann cells mainly localizes to Schmidt Lanterman incisures (SLI) (28) and that SLI are largely absent from myelin when PRX is lacking (64), the reduced abundance of MCT1 in *Prx*$^{-/-}$ myelin may be a consequence of the impaired myelin ultrastructure. Yet, considering that SLI are part of the cytosolic channels that may represent transport routes toward Schwann cell-dependent metabolic support of myelinated axons, the diminishment of MCT1 may contribute to reduced axonal diameters or axonal loss in *Prx*$^{-/-}$ mice, probably in conjunction with other molecular or morphological defects. Together, the in depth-analysis of proteins altered in neuropathy models can contribute to an improved understanding of nerve pathophysiology.

Compared to a previous approach (41), the number of proven neuropathy genes of which the encoded protein is mass spectrometrically identified in peripheral myelin has increased four-fold from eight to 32 in the present study. This reflects both that the number of proteins identified in myelin has approximately doubled and that more neuropathy genes are known due to the common use of genome sequencing. We note that our compendium comprises not only myelin-associated proteins causing (when mutated) demyelinating CMT1 (e.g., MPZ/P0, NEFL, PMP2) or intermediate CMT4 (GDAP1, NDRG1, PRX) but also axonal CMT2 (RAB7, GARS, HSPB1). Yet, the expression of genes causative of CMT2 is not necessarily limited to neurons, as exemplified by the classical myelin protein MPZ/P0. Indeed, a subset of *MPZ*-mutations causes axonal CMT2I or CMT2J (91–95), probably reflecting impaired axonal integrity as consequence of a mutation primarily affecting Schwann cells. We also note that the nuclear EGR2/KROX20 causative of demyelinating CMT1D has not been mass spectrometrically identified in myelin, reflecting that Schwann cell nuclei are efficiently removed during myelin purification.

While morphological analysis of peripheral nerves by light and electron microscopy is routine in numerous laboratories, systematic molecular analysis has been less straightforward. Using the sciatic nerve as a model, we show that systematic assessment of the myelin proteome and the total nerve transcriptome are suited to determine comprehensive molecular profiles in healthy nerves and in myelin-related disorders. Myelin proteome analysis can thus complement transcriptome analysis in assessing development, function and pathophysiology of peripheral nerves.

## MATERIALS AND METHODS

### Mouse models

*Prx*$^{-/-}$ mice (64) were kept on c57Bl/6 background in the animal facility of the University of Edinburgh (United Kingdom). Genotyping was by PCR on genomic DNA using the forward primers 5‘-CAGATTTGCT CTGCCCAAGT and 5‘-CGCCTTCTAT CGCCTTCTTGAC in combination with reverse primer 5‘-ATGCCCTCAC CCACTAACAG. The PCR yielded a 0.5 kb fragment for the wildtype allele and a 0.75 kb product for the mutant allele. The age of experimental animals is given in the figure legends. All animal work conformed to United Kingdom legislation (Scientific Procedures) Act 1986 and to the University of Edinburgh Ethical Review Committee policy; Home Office project license No. P0F4A25E9.

### Myelin purification

A light-weight membrane fraction enriched for myelin was purified from sciatic nerves of mice by sucrose density centrifugation and osmotic shocks as described (41,52). Myelin accumulates at the interface between 0.29 and 0.85 M sucrose. *Prx*$^{-/-}$ and wild type control C57Bl/6 mice were sacrificed by cervical dislocation at postnatal day 21 (P21). For each genotype, myelin was purified as three biological replicates (n=3); each biological replicate representing a pool of 20 sciatic nerves dissected from 10 mice. Protein concentration was determined using the DC Protein Assay Kit (Bio-Rad).

### Filter-aided sample preparation for proteome analysis

Protein fractions corresponding to 10 µg myelin protein were dissolved and processed according to a filter-aided sample preparation (FASP) protocol essentially as previously described for synaptic protein fractions (96) and as adapted to CNS myelin (52,97). Unless stated otherwise, all steps were automated on a liquid-handling workstation equipped with a vacuum manifold (Freedom EVO 150, Tecan) by using an adaptor device constructed in-house. Briefly, myelin protein samples were lysed and reduced in lysis buffer (7 M urea, 2 M thiourea, 10 mM DTT, 0.1 M Tris pH 8.5) containing 1% ASB-14 by shaking for 30 min at 37°C. Subsequently, the sample was diluted with ~10 volumes lysis buffer containing 2% CHAPS to reduce the ASB-14 concentration and loaded on centrifugal filter units (30 kDa MWCO, Merck Millipore). After removal of the detergents by washing twice with wash buffer (8 M urea, 10 mM DTT, 0.1 M Tris pH 8.5), proteins were alkylated with 50 mM iodoacetamide in 8 M urea, 0.1 M Tris pH 8.5 (20 min at RT), followed by two washes with wash buffer to remove excess reagent. Buffer was exchanged by washing three times with 50 mM ammonium bicarbonate (ABC) containing 10 % acetonitrile. After three additional washes with 50 mM ABC/10% acetonitrile, which were performed by centrifugation to ensure

quantitative removal of liquids potentially remaining underneath the ultrafiltration membrane, proteins were digested overnight at 37°C with 400 ng trypsin in 40 µl of the same buffer. Tryptic peptides were recovered by centrifugation followed by two additional extraction steps with 40 µl of 50 mM ABC and 40 µl of 1% trifluoroacetic acid (TFA), respectively. Aliquots of the combined flow-throughs were spiked with 10 fmol/µl of yeast enolase-1 tryptic digest standard (Waters Corporation) for quantification purposes and directly subjected to analysis by liquid chromatography coupled to electrospray mass spectrometry (LC-MS). A pool of all samples was injected at least before and after any sample set to monitor stability of instrument performance.

**Mass spectrometry**

Nanoscale reversed-phase UPLC separation of tryptic peptides was performed with a nanoAcquity UPLC system equipped with a Symmetry C18 5 µm, 180 µm × 20 mm trap column and a HSS T3 C18 1.8 µm, 75 µm × 250 mm analytical column (Waters Corporation) maintained at 45°C. Injected peptides were trapped for 4 min at a flow rate of 8 µl/min 0.1% TFA and then separated over 120 min at a flow rate of 300 nl/min with a gradient comprising two linear steps of 3-35% mobile phase B in 105 min and 35-60% mobile phase B in 15 min, respectively. Mobile phase A was water containing 0.1% formic acid while mobile phase B was acetonitrile containing 0.1% formic acid. Mass spectrometric analysis of tryptic peptides was performed using a Synapt G2-S quadrupole time-of-flight mass spectrometer equipped with ion mobility option (Waters Corporation). Positive ions in the mass range m/z 50 to 2000 were acquired with a typical resolution of at least 20.000 FWHM (full width at half maximum) and data were lock mass corrected post-acquisition. $UDMS^E$ and $DRE\text{-}UDMS^E$ analyses were performed in the ion mobility-enhanced data-independent acquisition mode with drift time-specific collision energies as described in detail by Distler et al. (48,49). Specifically, for $DRE\text{-}UDMS^E$ a deflection device (DRE lens) localized between the quadrupole and the ion mobility cell of the mass spectrometer was cycled between full (100% for 0.4 sec) and reduced (5% for 0.4 sec) ion transmission during one 0.8 sec full scan. Continuum LC-MS data were processed for signal detection, peak picking, and isotope and charge state deconvolution using Waters ProteinLynx Global Server (PLGS) version 3.0.2 (47). For protein identification, a custom database was compiled by adding the sequence information for yeast enolase 1 and porcine trypsin to the UniProtKB/Swiss-Prot mouse proteome and by appending the reversed sequence of each entry to enable the determination of false discovery rate (FDR). Precursor and fragment ion mass tolerances were automatically determined by PLGS 3.0.2 and were typically below 5 ppm for precursor ions and below 10 ppm (root mean square) for fragment ions. Carbamidomethylation of cysteine was specified as fixed and oxidation of methionine as variable modification. One missed trypsin cleavage

was allowed. Minimal ion matching requirements were two fragments per peptide, five fragments per protein, and one peptide per protein. The FDR for protein identification was set to 1% threshold.

**Analysis of proteomic data**

For each genotype (*Prx*$^{-/-}$ and wild type control mice sacrificed at P21), biochemical fractions enriched for PNS myelin were analyzed as three biological replicates (n=3 per condition); each biological replicate representing a pool of 20 sciatic nerves dissected from 10 mice. The samples were processed with replicate digestion and injection, resulting in four technical replicates per biological replicate and thus a total of 12 LC-MS runs per condition to be compared, essentially as previously reported for CNS myelin (36,97). The freely available software ISOQuant (www.isoquant.net) was used for post-identification analysis including retention time alignment, exact mass and retention time (EMRT) and ion mobility clustering, peak intensity normalization, isoform/homology filtering and calculation of absolute in-sample amounts for each detected protein (48,49,98) according to the TOP3 quantification approach (53,54). Only peptides with a minimum length of seven amino acids that were identified with scores above or equal to 5.5 in at least two runs were considered. FDR for both peptides and proteins was set to 1% threshold and only proteins reported by at least two peptides (one of which unique) were quantified using the TOP3 method. The parts per million (ppm) abundance values (i.e. the relative amount (w/w) of each protein in respect to the sum over all detected proteins) were log2-transformed and normalized by subtraction of the median derived from all data points for the given protein. Significant changes in protein abundance were detected by moderated t-statistics essentially as described (96,97) across all technical replicates using an empirical Bayes approach and false discovery (FDR)-based correction for multiple comparisons (100). For this purpose, the Bioconductor R packages "limma" (101) and "q-value" (102) were used in RStudio, an integrated development environment for the open source programming language R. Proteins identified as contaminants (e.g. components of blood or hair cells) were removed from the analysis. Proteins with ppm values below 100 which were not identified in one genotype were considered as just above detection level and also removed from the analysis. The relative abundance of a protein in myelin was accepted as altered if both statistically significant (q-value <0.05). Pie charts, heatmaps and volcano plots were prepared in Microsoft Excel 2013 and GraphPad Prism 7. Pearson's correlation coefficients derived from log2-transformed ppm abundance values were clustered and visualized with the tool heatmap.2 contained in the R package gplots (CRAN.R-project.org/package=gplots). Only pairwise complete observations were considered to reduce the influence of missing values on clustering behavior. The mass spectrometry proteomics data have been deposited to the ProteomeXchange Consortium

(proteomecentral.proteomexchange.org) via the PRIDE partner repository (103) with the dataset identifier PXD015960.

**Gel electrophoresis and silver staining of gels**

Protein concentration was determined using the DC Protein Assay kit (BioRad). Samples were separated on a 12% SDS-PAGE for 1 h at 200 V using the BioRad system, fixated overnight in 10% [v/v] acetic acid and 40 % [v/v] ethanol and then washed in 30% ethanol (2x 20 min) and dd$H_2O$ (1x 20 min). For sensitization, gels were incubated 1 min in 0.012% [v/v] $Na_2S_2O_3$ and subsequently washed with dd$H_2O$ (3x 20 sec). For silver staining, gels were impregnated for 20 min in 0.2 % [w/v] $AgNO_3$ / 0.04% formaldehyde, washed with dd$H_2O$ (3x 20 sec) and developed in 3% [w/v] $Na_2CO_3$ / 0.02% [w/v] formaldehyde. The reaction was stopped by exchanging the solution with 5% [v/v] acetic acid.

**Immunoblotting**

Immunoblotting was performed as described (104,105). Primary antibodies were specific for dystrophin-related-protein 2 (DRP2; Sigma; 1:1000), peripheral myelin protein 2 (PMP2; ProteinTech Group 12717-1-AP; 1:1000), proteolipid protein (PLP/DM20; A431 (106); 1:5000), Monocarboxylate transporter 1 (MCT1/SLC16A1; (107); 1:1000), periaxin (PRX; (59); 1:1000), sodium/potassium-transporting ATPase subunit alpha-1 (ATP1A1; 1:2000; Abcam #13736-1-AP), myelin protein zero (MPZ/P0; (108); kind gift by J. Archelos-Garcia; 1:10.000), voltage-dependent anion-selective channel protein (VDAC; Abcam #ab15895; 1:1000), basigin (BSG/CD147; ProteinTech Group #ab64616; 1:1000), neurofilament H (NEFH/NF-H; Covance #SMI-32P; 1:1000), voltage-gated potassium channel subunit A member 1 (KCNA1; Neuromab #73-007; 1:1000), EGR2/KROX20 ((109); kind gift by D. Meijer, Edinburgh; 1:1000) and myelin basic protein (MBP; 1:2000). To generate the latter antisera, rabbits were immunized (Pineda Antikörper Service, Berlin, Germany) with the KLH-coupled peptide CQDENPVVHFFK corresponding to amino acids 212-222 of mouse MBP isoform 1 (Swisprot/Uniprot-identifier P04370-1). Anti-MBP antisera were purified by affinity chromatography and extensively tested for specificity by immunoblot analysis of homogenate of brains dissected from wild-type mice compared to *Mbp*$^{shiverer/shiverer}$ mice that lack expression of MBP. Appropriate secondary anti-mouse or -rabbit antibodies conjugated to HRP were from dianova. Immunoblots were developed using the Enhanced Chemiluminescence Detection kit (Western Lightning® Plus, Perkin Elmer) and detected with the Intas ChemoCam system (INTAS Science Imaging Instruments GmbH, Göttingen, Germany).

**Immunolabelling of teased fibers**

Teased fibers were prepared as previously described (9,110). For each genotype, one male mouse was sacrificed by cervical dislocation at P17. Immunolabelling of teased fibers was performed as described (69). Briefly, teased fibers were fixed for 5 min in 4% paraformaldehyde, permeabilized 5 min with ice-cold methanol, washed in PBS (3x 5 min) and blocked for 1 h at 21°C in blocking buffer (10% horse serum, 0.25% Triton X-100, 1% bovine serum albumin in PBS). Primary antibodies were applied overnight at 4°C in incubation buffer (1.5% horse serum, 0.25% Triton X-100 in PBS). Samples were washed in PBS (3x 5 min) and secondary antibodies were applied in incubation buffer (1 h, RT). Samples were again washed in PBS (2x 5 min), and 4‘,6-diamidino-2-phenylindole (DAPI; 1:50 000 in PBS) was applied for 10 min at RT. Samples were briefly washed 2x with $ddH_2O$ and mounted using Aqua-Poly/Mount (Polysciences, Eppelheim, Germany). Antibodies were specific for myelin-associated glycoprotein (MAG clone 513; Chemicon MAB1567; 1:50) and MCT1/SLC16A1 (107). Secondary antibodies were donkey α-rabbit-Alexa488 (Invitrogen A21206; 1:1000) and donkey α-mouse-Alexa555 (Invitrogen A21202; 1:1000). Labeled teased fibers were imaged using the confocal microscope Leica SP5. The signal was collected with the objective HCX PL APO lambda blue 63.0.x1.20. DAPI staining was excited with 405 nm and collected between 417 nm - 480 nm. To excite the Alexa488 fluorophore an Argon laser with the excitation of 488 nm was used and the emission was set to 500 nm - 560 nm. Alexa555 was excited by using the DPSS561 laser at an excitation of 561 nm and the emission was set to 573 nm - 630 nm. To export and process the images LAS AF lite and Adobe Photoshop were used.

**mRNA abundance profiles**

Raw data were previously established (60) from the sciatic nerves of wild type Sprague Dawley rats at the indicated ages (E21, P6, P18; n=4 per time point). Briefly, sciatic nerves were dissected, the epineurium was removed, total RNA was extracted with the RNeasy Kit (Qiagen), concentration and quality (ratio of absorption at 260/280 nm) of RNA samples were determined using the NanoDrop spectrophotometer (ThermoScientific), integrity of the extracted RNA was determined with the Agilent 2100 Bioanalyser (Agilent Technologies) and RNA-Seq was performed using the Illumina HiSeq2000 platform. RNA-Seq raw data are available under the GEO accession number GSE115930 (60). For the present analysis, the fastqfiles were mapped to *rattus norvegicus* rn6 using Tophat Aligner and then quantified based on the Ensemble Transcripts release v96. The raw read counts were then normalized using the R package DESeq2. The normalized gene expression data was then standardized to a mean of zero and a standard deviation of one, therefore genes with similar changes in expression are close in the euclidian space. Clustering was performed on the standardized

682 data using the R package mfuzz. Transcripts displaying abundance differences of less than
683 10% coefficient of variation were considered developmentally unchanged.
684
685 **Venn diagrams**
686 Area-proportional Venn diagrams were prepared using BioVenn (111) at www.biovenn.nl/.
687
688 **GO-term**
689 For functional categorization of the myelin proteome the associated gene ontology terms
690 were systematically analyzed on the mRNA abundance cluster using the Database for
691 Annotation, Visualization and Integrated Discovery (DAVID; https://david.ncifcrf.gov). For
692 comparison known myelin proteins according to literature were added.
693
694 **Histological analysis**
695 *Prx*$^{-/-}$ and control mice were perfused at the indicated ages intravascularly with fixative
696 solution (2.5% glutaraldehyde, 4% paraformaldehyde, 0.1 M sodium cacodylate buffer, pH
697 7.4). Quadriceps nerves were removed, fixed for 2 h at room temperature, followed by 18 h
698 at 4°C in the same fixative, postfixed in $OsO_4$, dehydrated a graded series of ethanol,
699 followed by propylene oxide and embedded in Araldite. All axons not associated with a
700 Remak bundle were counted and categorized as myelinated or non-myelinated. All myelin
701 profiles lacking a recognizable axon were counted. The total number of axons were counted
702 on micrographs of toluidine blue stained Araldite sections (0.5 µm) of quadriceps nerves.
703 Precise p-values for the quantitative comparison between Ctrl and *Prx*$^{-/-}$ mice were: Total
704 number of axons (**Figure 6B**; Student's unpaired t-test): 2 mo p=0.01734; 4 mo p=2.1E-05; 9
705 mo p=0.007625; Number of myelinated axons (**Figure 6C**; Student's unpaired t-test): 2 mo
706 p=0.00444; 4 mo p=2.12E-05; 9 mo p=0.005766; Number of empty myelin profiles (**Figure**
707 **6D**; Student's unpaired t-test): 2 mo p=0.004445; 4 mo p=0.001461; 9 mo p=0.000695;
708 Axonal diameters (**Figure 6E-G**; two-sided Kolmogorow-Smirnow test): 2 mo p=2.20E-16; 4
709 mo p=2.20E-16; 9 mo p=2.20E-16.
710
711

**ACKNOWLEDGMENTS**

We thank J. Archelos-Garcia and D. Meijer for antibodies, T. Buscham and J. Edgar for discussions, L. Piepkorn for support in data analysis, K.-A. Nave for support made possible by a European Research Council Advanced Grant (‘MyeliNano‘ to K.-A.N.) and the International Max Planck Research School for Genome Science (IMPRS-GS) for supporting S.B.S..

**FUNDING**

Our work is supported by the Deutsche Forschungsgemeinschaft (DFG; Grants WE 2720/2-2, WE 2720/4-1 and WE 2720/5-1 to H.B.W. and RO 4076/3-2 to M.J.R.) and the Wellcome Trust (Grant No 0842424 to P.J.B.).

**CONFLICT OF INTEREST STATEMENT**

The authors declare no conflict of interest.

## REFERENCES


1. Weil M-T, Heibeck S, Töpperwien M, tom Dieck S, Ruhwedel T, Salditt T, et al. Axonal Ensheathment in the Nervous System of Lamprey: Implications for the Evolution of Myelinating Glia. J Neurosci [Internet]. 2018 Jul 18;38(29):6586–96. Available from: http://www.jneurosci.org/lookup/doi/10.1523/JNEUROSCI.1034-18.2018
2. Hartline DK, Colman DR. Rapid Conduction and the Evolution of Giant Axons and Myelinated Fibers. Curr Biol [Internet]. 2007 Jan;17(1):R29–35. Available from: https://linkinghub.elsevier.com/retrieve/pii/S0960982206025231
3. Rossor AM, Polke JM, Houlden H, Reilly MM. Clinical implications of genetic advances in Charcot–Marie–Tooth disease. Nat Rev Neurol [Internet]. 2013 Oct 10;9(10):562–71. Available from: http://www.nature.com/articles/nrneurol.2013.179
4. Michailov G V. Axonal Neuregulin-1 Regulates Myelin Sheath Thickness. Science (80- ) [Internet]. 2004 Apr 30;304(5671):700–3. Available from: http://www.sciencemag.org/cgi/doi/10.1126/science.1095862
5. Taveggia C, Zanazzi G, Petrylak A, Yano H, Rosenbluth J, Einheber S, et al. Neuregulin-1 Type III Determines the Ensheathment Fate of Axons. Neuron [Internet]. 2005 Sep;47(5):681–94. Available from: https://linkinghub.elsevier.com/retrieve/pii/S0896627305006926
6. Chernousov MA, Yu W-M, Chen Z-L, Carey DJ, Strickland S. Regulation of Schwann cell function by the extracellular matrix. Glia [Internet]. 2008 Nov 1;56(14):1498–507. Available from: http://doi.wiley.com/10.1002/glia.20740
7. Petersen SC, Luo R, Liebscher I, Giera S, Jeong S-J, Mogha A, et al. The Adhesion GPCR GPR126 Has Distinct, Domain-Dependent Functions in Schwann Cell Development Mediated by Interaction with Laminin-211. Neuron [Internet]. 2015 Feb;85(4):755–69. Available from: https://linkinghub.elsevier.com/retrieve/pii/S0896627314011660
8. Ghidinelli M, Poitelon Y, Shin YK, Ameroso D, Williamson C, Ferri C, et al. Laminin 211 inhibits protein kinase A in Schwann cells to modulate neuregulin 1 type III-driven myelination. Emery B, editor. PLOS Biol [Internet]. 2017 Jun 21;15(6):e2001408. Available from: https://dx.plos.org/10.1371/journal.pbio.2001408
9. Sherman DL, Fabrizi C, Gillespie CS, Brophy PJ. Specific Disruption of a Schwann Cell Dystrophin-Related Protein Complex in a Demyelinating Neuropathy. Neuron [Internet]. 2001 May;30(3):677–87. Available from: https://linkinghub.elsevier.com/retrieve/pii/S0896627301003270
10. Masaki T, Matsumura K, Hirata A, Yamada H, Hase A, Arai K, et al. Expression of Dystroglycan and the Laminin-α2 Chain in the Rat Peripheral Nerve during Development. Exp Neurol [Internet]. 2002 Mar;174(1):109–17. Available from: https://linkinghub.elsevier.com/retrieve/pii/S0014488601978562
11. Nodari A, Previtali SC, Dati G, Occhi S, Court FA, Colombelli C, et al. 6 4 Integrin and Dystroglycan Cooperate to Stabilize the Myelin Sheath. J Neurosci [Internet]. 2008 Jun 25;28(26):6714–9. Available from: http://www.jneurosci.org/cgi/doi/10.1523/JNEUROSCI.0326-08.2008

12. Raasakka A, Linxweiler H, Brophy PJ, Sherman DL, Kursula P. Direct Binding of the Flexible C-Terminal Segment of Periaxin to β4 Integrin Suggests a Molecular Basis for CMT4F. Front Mol Neurosci [Internet]. 2019 Apr 9;12. Available from: https://www.frontiersin.org/article/10.3389/fnmol.2019.00084/full
13. Hess A, Lansing AI. The fine structure of peripheral nerve fibers. Anat Rec. 1953;
14. Sherman DL, Brophy PJ. Mechanisms of axon ensheathment and myelin growth. Nat Rev Neurosci [Internet]. 2005 Sep;6(9):683–90. Available from: http://www.nature.com/articles/nrn1743
15. Pereira JA, Lebrun-Julien F, Suter U. Molecular mechanisms regulating myelination in the peripheral nervous system. Trends Neurosci [Internet]. 2012 Feb;35(2):123–34. Available from: https://linkinghub.elsevier.com/retrieve/pii/S0166223611001937
16. Grove M, Brophy PJ. FAK Is Required for Schwann Cell Spreading on Immature Basal Lamina to Coordinate the Radial Sorting of Peripheral Axons with Myelination. J Neurosci [Internet]. 2014 Oct 1;34(40):13422–34. Available from: http://www.jneurosci.org/cgi/doi/10.1523/JNEUROSCI.1764-14.2014
17. Monk KR, Feltri ML, Taveggia C. New insights on schwann cell development. Glia [Internet]. 2015 Aug;63(8):1376–93. Available from: http://doi.wiley.com/10.1002/glia.22852
18. Feltri ML, Poitelon Y, Previtali SC. How Schwann Cells Sort Axons. Neurosci [Internet]. 2016 Jun 16;22(3):252–65. Available from: http://journals.sagepub.com/doi/10.1177/1073858415572361
19. Giese KP, Martini R, Lemke G, Soriano P, Schachner M. Mouse P0 gene disruption leads to hypomyelination, abnormal expression of recognition molecules, and degeneration of myelin and axons. Cell [Internet]. 1992 Nov;71(4):565–76. Available from: https://linkinghub.elsevier.com/retrieve/pii/009286749290591Y
20. Martini R, Mohajeri MH, Kasper S, Giese KP, Schachner M. Mice doubly deficient in the genes for P0 and myelin basic protein show that both proteins contribute to the formation of the major dense line in peripheral nerve myelin. J Neurosci. 1995;
21. Nawaz S, Schweitzer J, Jahn O, Werner HB. Molecular evolution of myelin basic protein, an abundant structural myelin component. Glia [Internet]. 2013 Aug;61(8):1364–77. Available from: http://doi.wiley.com/10.1002/glia.22520
22. Greenfield S, Brostoff S, Eylar EH, Morell P. PROTEIN COMPOSITION OF MYELIN OF THE PERIPHERAL NERVOUS SYSTEM. J Neurochem [Internet]. 1973 Apr;20(4):1207–16. Available from: http://doi.wiley.com/10.1111/j.1471-4159.1973.tb00089.x
23. Brostoff SW, Karkhanis YD, Carlo DJ, Reuter W, Eylar EH. Isolation and partial characterization of the major proteins of rabbit sciatic nerve myelin. Brain Res [Internet]. 1975 Mar;86(3):449–58. Available from: https://linkinghub.elsevier.com/retrieve/pii/0006899375908951
24. Nave K-A, Werner HB. Myelination of the Nervous System: Mechanisms and Functions. Annu Rev Cell Dev Biol [Internet]. 2014 Oct 11;30(1):503–33. Available from: http://www.annualreviews.org/doi/10.1146/annurev-cellbio-100913-013101
25. Kleopa KA, Sargiannidou I. Connexins, gap junctions and peripheral neuropathy. Neurosci Lett

[Internet]. 2015 Jun;596:27–32. Available from: https://linkinghub.elsevier.com/retrieve/pii/S0304394014008453

26. Court FA, Sherman DL, Pratt T, Garry EM, Ribchester RR, Cottrell DF, et al. Restricted growth of Schwann cells lacking Cajal bands slows conduction in myelinated nerves. Nature [Internet]. 2004 Sep;431(7005):191–5. Available from: http://www.nature.com/articles/nature02841

27. Beirowski B, Babetto E, Golden JP, Chen Y-J, Yang K, Gross RW, et al. Metabolic regulator LKB1 is crucial for Schwann cell–mediated axon maintenance. Nat Neurosci [Internet]. 2014 Oct 7;17(10):1351–61. Available from: http://www.nature.com/articles/nn.3809

28. Domenech-Estevez E, Baloui H, Repond C, Rosafio K, Medard J-J, Tricaud N, et al. Distribution of Monocarboxylate Transporters in the Peripheral Nervous System Suggests Putative Roles in Lactate Shuttling and Myelination. J Neurosci [Internet]. 2015 Mar 11;35(10):4151–6. Available from: http://www.jneurosci.org/cgi/doi/10.1523/JNEUROSCI.3534-14.2015

29. Kim S, Maynard JC, Sasaki Y, Strickland A, Sherman DL, Brophy PJ, et al. Schwann Cell O-GlcNAc Glycosylation Is Required for Myelin Maintenance and Axon Integrity. J Neurosci [Internet]. 2016 Sep 14;36(37):9633–46. Available from: http://www.jneurosci.org/cgi/doi/10.1523/JNEUROSCI.1235-16.2016

30. Gonçalves NP, Vægter CB, Andersen H, Østergaard L, Calcutt NA, Jensen TS. Schwann cell interactions with axons and microvessels in diabetic neuropathy. Nat Rev Neurol [Internet]. 2017 Mar 30;13(3):135–47. Available from: http://www.nature.com/articles/nrneurol.2016.201

31. Stassart RM, Möbius W, Nave K-A, Edgar JM. The Axon-Myelin Unit in Development and Degenerative Disease. Front Neurosci [Internet]. 2018 Jul 11;12. Available from: https://www.frontiersin.org/article/10.3389/fnins.2018.00467/full

32. Nagarajan R, Le N, Mahoney H, Araki T, Milbrandt J. Deciphering peripheral nerve myelination by using Schwann cell expression profiling. Proc Natl Acad Sci [Internet]. 2002 Jun 25;99(13):8998–9003. Available from: http://www.pnas.org/cgi/doi/10.1073/pnas.132080999

33. Le N, Nagarajan R, Wang JYT, Araki T, Schmidt RE, Milbrandt J. Analysis of congenital hypomyelinating Egr2Lo/Lo nerves identifies Sox2 as an inhibitor of Schwann cell differentiation and myelination. Proc Natl Acad Sci [Internet]. 2005 Feb 15;102(7):2596–601. Available from: http://www.pnas.org/cgi/doi/10.1073/pnas.0407836102

34. Ryu EJ, Yang M, Gustin JA, Chang L-W, Freimuth RR, Nagarajan R, et al. Analysis of Peripheral Nerve Expression Profiles Identifies a Novel Myelin Glycoprotein, MP11. J Neurosci [Internet]. 2008 Jul 23;28(30):7563–73. Available from: http://www.jneurosci.org/cgi/doi/10.1523/JNEUROSCI.1659-08.2008

35. Zhang Y, Chen K, Sloan SA, Bennett ML, Scholze AR, O'Keeffe S, et al. An RNA-Sequencing Transcriptome and Splicing Database of Glia, Neurons, and Vascular Cells of the Cerebral Cortex. J Neurosci [Internet]. 2014 Sep 3;34(36):11929–47. Available from: http://www.jneurosci.org/cgi/doi/10.1523/JNEUROSCI.1860-14.2014

36. Patzig J, Erwig MS, Tenzer S, Kusch K, Dibaj P, Möbius W, et al. Septin/anillin filaments scaffold central nervous system myelin to accelerate nerve conduction. Elife. 2016;5:e17119.

37. Sharma K, Schmitt S, Bergner CG, Tyanova S, Kannaiyan N, Manrique-Hoyos N, et al. Cell

type– and brain region–resolved mouse brain proteome. Nat Neurosci [Internet]. 2015 Dec 2;18(12):1819–31. Available from: http://www.nature.com/articles/nn.4160

38. Thakurela S, Garding A, Jung RB, Müller C, Goebbels S, White R, et al. The transcriptome of mouse central nervous system myelin. Sci Rep [Internet]. 2016 May 13;6(1):25828. Available from: http://www.nature.com/articles/srep25828

39. Marques S, Zeisel A, Codeluppi S, van Bruggen D, Mendanha Falcao A, Xiao L, et al. Oligodendrocyte heterogeneity in the mouse juvenile and adult central nervous system. Science (80- ) [Internet]. 2016 Jun 10;352(6291):1326–9. Available from: http://www.sciencemag.org/cgi/doi/10.1126/science.aaf6463

40. De Monasterio-Schrader P, Jahn O, Tenzer S, Wichert SP, Patzig J, Werner HB. Systematic approaches to central nervous system myelin. Cellular and Molecular Life Sciences. 2012.

41. Patzig J, Jahn O, Tenzer S, Wichert SP, de Monasterio-Schrader P, Rosfa S, et al. Quantitative and Integrative Proteome Analysis of Peripheral Nerve Myelin Identifies Novel Myelin Proteins and Candidate Neuropathy Loci. J Neurosci [Internet]. 2011 Nov 9;31(45):16369–86. Available from: http://www.jneurosci.org/cgi/doi/10.1523/JNEUROSCI.4016-11.2011

42. Kangas SM, Ohlmeier S, Sormunen R, Jouhilahti E-M, Peltonen S, Peltonen J, et al. An approach to comprehensive genome and proteome expression analyses in Schwann cells and neurons during peripheral nerve myelin formation. J Neurochem [Internet]. 2016 Sep;138(6):830–44. Available from: http://doi.wiley.com/10.1111/jnc.13722

43. Kusch K, Uecker M, Liepold T, Möbius W, Hoffmann C, Neumann H, et al. Partial Immunoblotting of 2D-Gels: A Novel Method to Identify Post-Translationally Modified Proteins Exemplified for the Myelin Acetylome. Proteomes [Internet]. 2017 Jan 12;5(4):3. Available from: http://www.mdpi.com/2227-7382/5/1/3

44. Neilson KA, Ali NA, Muralidharan S, Mirzaei M, Mariani M, Assadourian G, et al. Less label, more free: Approaches in label-free quantitative mass spectrometry. Proteomics. 2011.

45. Distler U, Kuharev J, Tenzer S. Biomedical applications of ion mobility-enhanced data-independent acquisition-based label-free quantitative proteomics. Expert Rev Proteomics. 2014;

46. Geromanos SJ, Vissers JPC, Silva JC, Dorschel CA, Li GZ, Gorenstein M V., et al. The detection, correlation, and comparison of peptide precursor and product ions from data independent LC-MS with data dependant LC-MS/MS. Proteomics. 2009;

47. Li GZ, Vissers JPC, Silva JC, Golick D, Gorenstein M V., Geromanos SJ. Database searching and accounting of multiplexed precursor and product ion spectra from the data independent analysis of simple and complex peptide mixtures. Proteomics. 2009;

48. Distler U, Kuharev J, Navarro P, Tenzer S. Label-free quantification in ion mobility–enhanced data-independent acquisition proteomics. Nat Protoc [Internet]. 2016 Apr 24;11(4):795–812. Available from: http://www.nature.com/articles/nprot.2016.042

49. Distler U, Kuharev J, Navarro P, Levin Y, Schild H, Tenzer S. Drift time-specific collision energies enable deep-coverage data-independent acquisition proteomics. Nat Methods [Internet]. 2014 Feb 15;11(2):167–70. Available from:

http://www.nature.com/articles/nmeth.2767
50. Larocca JN, Norton WT. Isolation of Myelin. Curr Protoc Cell Biol [Internet]. 2006 Dec;33(1):3.25.1-3.25.19. Available from: http://doi.wiley.com/10.1002/0471143030.cb0325s33
51. Jahn O, Tenzer S, Werner HB. Myelin proteomics: Molecular anatomy of an insulating sheath. Molecular Neurobiology. 2009.
52. Erwig MS, Hesse D, Jung RB, Uecker M, Kusch K, Tenzer S, et al. Myelin: Methods for Purification and Proteome Analysis. In: Methods in Molecular Biology [Internet]. 2019. p. 37–63. Available from: http://link.springer.com/10.1007/978-1-4939-9072-6_3
53. Silva JC, Gorenstein M V., Li G-Z, Vissers JPC, Geromanos SJ. Absolute Quantification of Proteins by LCMS E. Mol Cell Proteomics [Internet]. 2006 Jan;5(1):144–56. Available from: http://www.mcponline.org/lookup/doi/10.1074/mcp.M500230-MCP200
54. Ahrné E, Molzahn L, Glatter T, Schmidt A. Critical assessment of proteome-wide label-free absolute abundance estimation strategies. Proteomics. 2013;
55. Dodds JN, Baker ES. Ion Mobility Spectrometry: Fundamental Concepts, Instrumentation, Applications, and the Road Ahead. J Am Soc Mass Spectrom. 2019;
56. Micko S, Schlaepfer WW. PROTEIN COMPOSITION OF AXONS and MYELIN FROM RAT and HUMAN PERIPHERAL NERVES. J Neurochem [Internet]. 1978 May;30(5):1041–9. Available from: http://doi.wiley.com/10.1111/j.1471-4159.1978.tb12397.x
57. Smith ME, Curtis BM. FROG SCIATIC NERVE MYELIN: A CHEMICAL CHARACTERIZATION. J Neurochem [Internet]. 1979 Aug;33(2):447–52. Available from: http://doi.wiley.com/10.1111/j.1471-4159.1979.tb05174.x
58. Whitaker JN. The protein antigens of peripheral nerve myelin. Ann Neurol [Internet]. 1981;9(S1):56–64. Available from: http://doi.wiley.com/10.1002/ana.410090710
59. Gillespie CS, Sherman DL, Blair GE, Brophy PJ. Periaxin, a novel protein of myelinating schwann cells with a possible role in axonal ensheathment. Neuron [Internet]. 1994 Mar;12(3):497–508. Available from: https://linkinghub.elsevier.com/retrieve/pii/0896627394902089
60. Fledrich R, Abdelaal T, Rasch L, Bansal V, Schütza V, Brügger B, et al. Targeting myelin lipid metabolism as a potential therapeutic strategy in a model of CMT1A neuropathy. Nat Commun [Internet]. 2018 Dec 2;9(1):3025. Available from: http://www.nature.com/articles/s41467-018-05420-0
61. Pareyson D, Marchesi C. Diagnosis, natural history, and management of Charcot–Marie–Tooth disease. Lancet Neurol [Internet]. 2009 Jul;8(7):654–67. Available from: https://linkinghub.elsevier.com/retrieve/pii/S1474442209701103
62. Baets J, De Jonghe P, Timmerman V. Recent advances in Charcot–Marie–Tooth disease. Curr Opin Neurol [Internet]. 2014 Oct;27(5):532–40. Available from: http://content.wkhealth.com/linkback/openurl?sid=WKPTLP:landingpage&an=00019052-201410000-00006
63. Brennan KM, Bai Y, Shy ME. Demyelinating CMT–what's known, what's new and what's in store? Neurosci Lett [Internet]. 2015 Jun;596:14–26. Available from: https://linkinghub.elsevier.com/retrieve/pii/S0304394015000725

64. Gillespie CS, Sherman DL, Fleetwood-Walker SM, Cottrell DF, Tait S, Garry EM, et al. Peripheral Demyelination and Neuropathic Pain Behavior in Periaxin-Deficient Mice. Neuron [Internet]. 2000 May;26(2):523–31. Available from: https://linkinghub.elsevier.com/retrieve/pii/S0896627300811848
65. Guilbot A. A mutation in periaxin is responsible for CMT4F, an autosomal recessive form of Charcot-Marie-Tooth disease. Hum Mol Genet [Internet]. 2001 Feb 1;10(4):415–21. Available from: https://academic.oup.com/hmg/article-lookup/doi/10.1093/hmg/10.4.415
66. Berger P, Niemann A, Suter U. Schwann cells and the pathogenesis of inherited motor and sensory neuropathies (Charcot-Marie-Tooth disease). Glia [Internet]. 2006 Sep;54(4):243–57. Available from: http://doi.wiley.com/10.1002/glia.20386
67. Marchesi C, Milani M, Morbin M, Cesani M, Lauria G, Scaioli V, et al. Four novel cases of periaxin-related neuropathy and review of the literature. Neurology [Internet]. 2010 Nov 16;75(20):1830–8. Available from: http://www.neurology.org/cgi/doi/10.1212/WNL.0b013e3181fd6314
68. Philp NJ, Ochrietor JD, Rudoy C, Muramatsu T, Linser PJ. Loss of MCT1, MCT3, and MCT4 Expression in the Retinal Pigment Epithelium and Neural Retina of the 5A11/Basigin-Null Mouse. Investig Opthalmology Vis Sci [Internet]. 2003 Mar 1;44(3):1305. Available from: http://iovs.arvojournals.org/article.aspx?doi=10.1167/iovs.02-0552
69. Patzig J, Kusch K, Fledrich R, Eichel MA, Lüders KA, Möbius W, et al. Proteolipid protein modulates preservation of peripheral axons and premature death when myelin protein zero is lacking. Glia [Internet]. 2016 Jan;64(1):155–74. Available from: http://doi.wiley.com/10.1002/glia.22922
70. Lee Y, Morrison BM, Li Y, Lengacher S, Farah MH, Hoffman PN, et al. Oligodendroglia metabolically support axons and contribute to neurodegeneration. Nature [Internet]. 2012 Jul 11;487(7408):443–8. Available from: http://www.nature.com/articles/nature11314
71. Fünfschilling U, Supplie LM, Mahad D, Boretius S, Saab AS, Edgar J, et al. Glycolytic oligodendrocytes maintain myelin and long-term axonal integrity. Nature [Internet]. 2012 May 29;485(7399):517–21. Available from: http://www.nature.com/articles/nature11007
72. Morrison BM, Tsingalia A, Vidensky S, Lee Y, Jin L, Farah MH, et al. Deficiency in monocarboxylate transporter 1 (MCT1) in mice delays regeneration of peripheral nerves following sciatic nerve crush. Exp Neurol [Internet]. 2015 Jan;263:325–38. Available from: https://linkinghub.elsevier.com/retrieve/pii/S0014488614003549
73. Morrison BM, Lee Y, Rothstein JD. Oligodendroglia: Metabolic supporters of axons. Trends in Cell Biology. 2013.
74. Saab AS, Tzvetanova ID, Nave K-A. The role of myelin and oligodendrocytes in axonal energy metabolism. Curr Opin Neurobiol [Internet]. 2013 Dec;23(6):1065–72. Available from: https://linkinghub.elsevier.com/retrieve/pii/S0959438813001888
75. Rinholm JE, Bergersen LH. White matter lactate – Does it matter? Neuroscience [Internet]. 2014 Sep;276:109–16. Available from: https://linkinghub.elsevier.com/retrieve/pii/S0306452213008464
76. Jha MK, Lee Y, Russell KA, Yang F, Dastgheyb RM, Deme P, et al. Monocarboxylate

transporter 1 in Schwann cells contributes to maintenance of sensory nerve myelination during aging. Glia. 2019;

77. Edgar JM, McLaughlin M, Werner HB, McCulloch MC, Barrie JA, Brown A, et al. Early ultrastructural defects of axons and axon-glia junctions in mice lacking expression of Cnp1. Glia. 2009;

78. Verheijen MHG. Local regulation of fat metabolism in peripheral nerves. Genes Dev [Internet]. 2003 Oct 1;17(19):2450–64. Available from: http://www.genesdev.org/cgi/doi/10.1101/gad.1116203

79. Buchstaller J. Efficient Isolation and Gene Expression Profiling of Small Numbers of Neural Crest Stem Cells and Developing Schwann Cells. J Neurosci [Internet]. 2004 Mar 10;24(10):2357–65. Available from: http://www.jneurosci.org/cgi/doi/10.1523/JNEUROSCI.4083-03.2004

80. D'antonio M, Michalovich D, Paterson M, Droggiti A, Woodhoo A, Mirsky R, et al. Gene profiling and bioinformatic analysis of Schwann cell embryonic development and myelination. Glia [Internet]. 2006 Apr 1;53(5):501–15. Available from: http://doi.wiley.com/10.1002/glia.20309

81. Schaeren-Wiemers N, Bonnet A, Erb M, Erne B, Bartsch U, Kern F, et al. The raft-associated protein MAL is required for maintenance of proper axon–glia interactions in the central nervous system. J Cell Biol [Internet]. 2004 Aug 30;166(5):731–42. Available from: http://www.jcb.org/lookup/doi/10.1083/jcb.200406092

82. Adlkofer K, Martini R, Aguzzi A, Zielasek J, Toyka K V., Suter U. Hypermyelination and demyelinating peripheral neuropathy in Pmp22-deficient mice. Nat Genet [Internet]. 1995 Nov;11(3):274–80. Available from: http://www.nature.com/articles/ng1195-274

83. Riethmacher D, Sonnenberg-Riethmacher E, Brinkmann V, Yamaai T, Lewin GR, Birchmeier C. Severe neuropathies in mice with targeted mutations in the ErbB3 receptor. Nature [Internet]. 1997 Oct;389(6652):725–30. Available from: http://www.nature.com/articles/39593

84. Woldeyesus MT, Britsch S, Riethmacher D, Xu L, Sonnenberg-Riethmacher E, Abou-Rebyeh F, et al. Peripheral nervous system defects in erbB2 mutants following genetic rescue of heart development. Genes Dev [Internet]. 1999 Oct 1;13(19):2538–48. Available from: http://www.genesdev.org/cgi/doi/10.1101/gad.13.19.2538

85. Ackerman SD, Luo R, Poitelon Y, Mogha A, Harty BL, D'Rozario M, et al. GPR56/ADGRG1 regulates development and maintenance of peripheral myelin. J Exp Med [Internet]. 2018 Mar 5;215(3):941–61. Available from: http://www.jem.org/lookup/doi/10.1084/jem.20161714

86. Monk KR, Oshima K, Jors S, Heller S, Talbot WS. Gpr126 is essential for peripheral nerve development and myelination in mammals. Development [Internet]. 2011 Jul 1;138(13):2673–80. Available from: http://dev.biologists.org/cgi/doi/10.1242/dev.062224

87. Monk KR, Naylor SG, Glenn TD, Mercurio S, Perlin JR, Dominguez C, et al. A G Protein-Coupled Receptor Is Essential for Schwann Cells to Initiate Myelination. Science (80- ) [Internet]. 2009 Sep 11;325(5946):1402–5. Available from: http://www.sciencemag.org/cgi/doi/10.1126/science.1173474

88. Kabzinska D, Drac H, Sherman DL, Kostera-Pruszczyk A, Brophy PJ, Kochanski A, et al.

Charcot-Marie-Tooth type 4F disease caused by S399fsx410 mutation in the PRX gene. Neurology [Internet]. 2006 Mar 14;66(5):745–7. Available from: http://www.neurology.org/cgi/doi/10.1212/01.wnl.0000201269.46071.35

89. Baránková L, Šišková D, Hühne K, Vyhnálková E, Sakmaryová I, Bojar M, et al. A 71-nucleotide deletion in the periaxin gene in a Romani patient with early-onset slowly progressive demyelinating CMT. Eur J Neurol [Internet]. 2008 Jun;15(6):548–51. Available from: http://doi.wiley.com/10.1111/j.1468-1331.2008.02104.x

90. Tokunaga S, Hashiguchi A, Yoshimura A, Maeda K, Suzuki T, Haruki H, et al. Late-onset Charcot–Marie–Tooth disease 4F caused by periaxin gene mutation. Neurogenetics [Internet]. 2012 Nov 1;13(4):359–65. Available from: http://link.springer.com/10.1007/s10048-012-0338-5

91. Gallardo E, García A, Ramón C, Maraví E, Infante J, Gastón I, et al. Charcot–Marie–Tooth disease type 2J with MPZ Thr124Met mutation: clinico-electrophysiological and MRI study of a family. J Neurol [Internet]. 2009 Dec 22;256(12):2061–71. Available from: http://link.springer.com/10.1007/s00415-009-5251-y

92. Leal A, Berghoff C, Berghoff M, Rojas-Araya M, Ortiz C, Heuss D, et al. A Costa Rican family affected with Charcot-Marie-Tooth disease due to the myelin protein zero (MPZ) p.Thr124Met mutation shares the Belgian haplotype. Rev Biol Trop [Internet]. 2014 Dec 1;62(4):1285. Available from: http://revistas.ucr.ac.cr/index.php/rbt/article/view/13473

93. Tokuda N, Noto Y, Kitani-Morii F, Hamano A, Kasai T, Shiga K, et al. Parasympathetic Dominant Autonomic Dysfunction in Charcot-Marie-Tooth Disease Type 2J with the *MPZ* Thr124Met Mutation. Intern Med [Internet]. 2015;54(15):1919–22. Available from: https://www.jstage.jst.go.jp/article/internalmedicine/54/15/54_54.4259/_article

94. Duan X, Gu W, Hao Y, Wang R, Wen H, Sun S, et al. A Novel Asp121Asn Mutation of Myelin Protein Zero Is Associated with Late-Onset Axonal Charcot-Marie-Tooth Disease, Hearing Loss and Pupil Abnormalities. Front Aging Neurosci [Internet]. 2016 Sep 22;8. Available from: http://journal.frontiersin.org/Article/10.3389/fnagi.2016.00222/abstract

95. Fabrizi GM, Tamburin S, Cavallaro T, Cabrini I, Ferrarini M, Taioli F, et al. The spectrum of Charcot-Marie-Tooth disease due to myelin protein zero: An electrodiagnostic, nerve ultrasound and histological study. Clin Neurophysiol [Internet]. 2018 Jan;129(1):21–32. Available from: https://linkinghub.elsevier.com/retrieve/pii/S1388245717310854

96. Ambrozkiewicz MC, Schwark M, Kishimoto-Suga M, Borisova E, Hori K, Salazar-Lázaro A, et al. Polarity Acquisition in Cortical Neurons Is Driven by Synergistic Action of Sox9-Regulated Wwp1 and Wwp2 E3 Ubiquitin Ligases and Intronic miR-140. Neuron [Internet]. 2018 Dec;100(5):1097-1115.e15. Available from: https://linkinghub.elsevier.com/retrieve/pii/S0896627318308961

97. Erwig MS, Patzig J, Steyer AM, Dibaj P, Heilmann M, Heilmann I, et al. Anillin facilitates septin assembly to prevent pathological outfoldings of central nervous system myelin. Elife [Internet]. 2019 Jan 23;8. Available from: https://elifesciences.org/articles/43888

98. Kuharev J, Navarro P, Distler U, Jahn O, Tenzer S. In-depth evaluation of software tools for data-independent acquisition based label-free quantification. Proteomics [Internet]. 2015 Sep;15(18):3140–51. Available from: http://doi.wiley.com/10.1002/pmic.201400396

99. Silva JC, Denny R, Dorschel C, Gorenstein M V., Li G-Z, Richardson K, et al. Simultaneous Qualitative and Quantitative Analysis of the Escherichia coli Proteome. Mol Cell Proteomics [Internet]. 2006 Apr;5(4):589–607. Available from: http://www.mcponline.org/lookup/doi/10.1074/mcp.M500321-MCP200
100. Kammers K, Cole RN, Tiengwe C, Ruczinski I. Detecting significant changes in protein abundance. EuPA Open Proteomics [Internet]. 2015 Jun;7:11–9. Available from: https://linkinghub.elsevier.com/retrieve/pii/S2212968515000069
101. Ritchie ME, Phipson B, Wu D, Hu Y, Law CW, Shi W, et al. limma powers differential expression analyses for RNA-sequencing and microarray studies. Nucleic Acids Res [Internet]. 2015 Apr 20;43(7):e47–e47. Available from: http://academic.oup.com/nar/article/43/7/e47/2414268/limma-powers-differential-expression-analyses-for
102. Storey JD. The positive false discovery rate: a Bayesian interpretation and the q -value. Ann Stat [Internet]. 2003 Dec;31(6):2013–35. Available from: http://projecteuclid.org/euclid.aos/1074290335
103. Vizcaíno JA, Csordas A, Del-Toro N, Dianes JA, Griss J, Lavidas I, et al. 2016 update of the PRIDE database and its related tools. Nucleic Acids Res [Internet]. 2016 Jan 4;44(D1):D447–56. Available from: https://academic.oup.com/nar/article-lookup/doi/10.1093/nar/gkv1145
104. Schardt A, Brinkmann BG, Mitkovski M, Sereda MW, Werner HB, Nave K-A. The SNARE protein SNAP-29 interacts with the GTPase Rab3A: Implications for membrane trafficking in myelinating glia. J Neurosci Res [Internet]. 2009 Nov 15;87(15):3465–79. Available from: http://doi.wiley.com/10.1002/jnr.22005
105. de Monasterio-Schrader P, Patzig J, Möbius W, Barrette B, Wagner TL, Kusch K, et al. Uncoupling of neuroinflammation from axonal degeneration in mice lacking the myelin protein tetraspanin-2. Glia. 2013;
106. Jung M, Sommer I, Schachner M, Nave KA. Monoclonal antibody O10 defines a conformationally sensitive cell- surface epitope of proteolipid protein (PLP): Evidence that PLP misfolding underlies dysmyelination in mutant mice. J Neurosci. 1996;16(24):7920–9.
107. Stumpf SK, Berghoff SA, Trevisiol A, Spieth L, Düking T, Schneider L V., et al. Ketogenic diet ameliorates axonal defects and promotes myelination in Pelizaeus–Merzbacher disease. Acta Neuropathol [Internet]. 2019 Jul 27;138(1):147–61. Available from: http://link.springer.com/10.1007/s00401-019-01985-2
108. Archelos JJ, Roggenbuck K, Scheider-Schaulies J, Linington C, Toyka K V., Hartung H-P. Production and characterization of monoclonal antibodies to the extracellular domain of P0. J Neurosci Res [Internet]. 1993 May 1;35(1):46–53. Available from: http://doi.wiley.com/10.1002/jnr.490350107
109. Darbas A, Jaegle M, Walbeehm E, van den Burg H, Driegen S, Broos L, et al. Cell autonomy of the mouse claw paw mutation. Dev Biol [Internet]. 2004 Aug;272(2):470–82. Available from: https://linkinghub.elsevier.com/retrieve/pii/S0012160604003616
110. Catenaccio A, Court FA. Teased Fiber Preparation of Myelinated Nerve Fibers from Peripheral Nerves for Vital Dye Staining and Immunofluorescence Analysis. In: Methods in Molecular

Biology [Internet]. 2018. p. 329–37. Available from: http://link.springer.com/10.1007/978-1-4939-7649-2_21

111. Hulsen T, de Vlieg J, Alkema W. BioVenn – a web application for the comparison and visualization of biological lists using area-proportional Venn diagrams. BMC Genomics [Internet]. 2008;9(1):488. Available from: http://bmcgenomics.biomedcentral.com/articles/10.1186/1471-2164-9-488

## FIGURE LEGENDS

### Figure 1. Proteome analysis of peripheral myelin

**(A)** Schematic illustration of a previous approach to the peripheral myelin proteome (41) compared with the present workflow. Note that the current workflow allows largely automated sample processing and omits labor-intense 2-dimensional differential gel-electrophoresis, thereby considerably reducing hands-on time. Nano LC-MS analysis by data-independent acquisition (DIA) using three different data acquisition modes provides efficient identification and quantification of abundant myelin proteins ($MS^E$; see **Figure 2**), a comprehensive inventory ($UDMS^E$; see **Figures 3-4**) and gel-free differential analysis of hundreds of distinct proteins (DRE-$UDMS^E$; see **Figure 5**). Samples were analyzed in three biological replicates.

**(B)** Immunoblot of myelin biochemically enriched from sciatic nerves of wild-type mice at postnatal day 21 (P21). Equal amounts of corresponding nerve lysate were loaded to compare the abundance of marker proteins for compact myelin (MPZ/P0, MBP, PMP2), non-compact myelin (PRX), the Schwann cell nucleus (KROX20/EGR2), axons (NEFH, KCNA1) and mitochondria (VDAC). Blots show n=2 biological replicates representative of n=3 biological replicates. Note that myelin markers are enriched in purified myelin; other cellular markers are reduced.

**(C)** Number and relative abundance of proteins identified in myelin purified from the sciatic nerves of wild-type mice using three different data acquisition modes ($MS^E$, $UDMS^E$, DRE-$UDMS^E$). Note that $MS^E$ (orange) provides the best information about the relative abundance of high-abundant myelin proteins (dynamic range of more than four orders of magnitude) but identifies comparatively fewer proteins in purified myelin. $UDMS^E$ (blue) identifies the largest number of proteins but provides only a lower dynamic range of about three orders of magnitude. DRE-$UDMS^E$ (green) identifies an intermediate number of proteins with an intermediate dynamic range of about four orders of magnitude. Note that $MS^E$ with very high dynamic range is required for the quantification of the exceptionally abundant myelin protein zero (MPZ/P0), myelin basic protein (MBP) and periaxin (PRX). ppm, parts per million.

**(D)** Venn diagram comparing the number of proteins identified in PNS myelin by $MS^E$, $UDMS^E$ and DRE-$UDMS^E$. Note the high overlap of identified proteins.

**(E)** Venn diagram of the proteins identified in PNS myelin by $UDMS^E$ in this study compared with those identified in two previous approaches (41,42).

### Figure 1-supplement 1. Clustered heatmap of Pearson's correlation coefficients for protein abundance comparing data acquisition modes.

The heatmap compares the $log_2$ transformed ppm protein abundance values to assess peripheral myelin purified from wild type mice using three data acquisition modes ($MS^E$, $UDMS^E$, DRE-$UDMS^E$). The inset shows the color key and the histogram for the values of the correlation coefficients. Note that the runs cluster with a high overall correlation (>0.75) into three conditions defined by the acquisition mode, in agreement with the experimental design. Among the samples analyzed by different acquisition modes, DRE-$UDMS^E$ similarly correlates with both $MS^E$ and $UDMS^E$, reflecting its intermediate nature.

**Figure 2. Relative abundance of peripheral myelin proteins**

$MS^E$ was used to identify and quantify proteins in myelin purified from the sciatic nerves of wild-type mice at P21; their relative abundance is given as percent with relative standard deviation (% +/- RSD). Note that known myelin proteins constitute >80% of the total myelin protein; proteins not previously associated with myelin constitute <20%. Mass spectrometric quantification based on 3 biological replicates per genotype with 4 technical replicates each (see **Figure 1-source data 1**).

**Figure 3. Developmental mRNA abundance profiles of myelin-associated genes**

**(A)** K-means clustering was performed for the mRNA profiles of those 1046 proteins in our myelin proteome inventory for which significant mRNA expression was found by RNA-Seq in the sciatic nerve of rats dissected at ages E21, P6, P18 and 6 months (M6). Note that this filtering strategy allows to selectively display the developmental abundance profiles of those transcripts that encode myelin-associated proteins rather than of all transcripts present in the nerve. Standardized mRNA abundance profiles are shown (n=4 biological replicates per age). Known myelin genes are displayed in red. For comparison, *Pmp22* mRNA was included although the small tetraspan protein PMP22 was not mass spectrometrically identified due to its unfavorable distribution of tryptic cleavage sites. Normalized counts for all mRNAs including those displaying developmentally unchanged abundance are provided in **Figure 3-Source data 1**.

**(B)** Numbers of mRNAs per cluster.

**Figure 4. Categorization of annotated protein functions**

All proteins identified in peripheral myelin by $UDMS^E$ (turquoise) and the respective developmental expression clusters (**Figure 3**; shades of red) were analyzed for overrepresented functional annotations using gene ontology (GO) terms. The graph displays

the percentage of proteins in each cluster that were annotated with a particular function. For comparison, known myelin proteins were annotated. n.o., not over-represented.

**Figure 5. Molecular analysis of myelin in the *Prx*$^{-/-}$ mouse model of CMT4F**

**(A)** Myelin purified from sciatic nerves dissected from *Prx*$^{-/-}$ and control mice at P21 was separated by SDS-PAGE (0.5 µg protein load) and proteins were visualized by silver staining. Bands constituted by the most abundant myelin proteins (MPZ/P0, MBP, PRX) are annotated. Note that no band constituted by PRX was detected in *Prx*$^{-/-}$ myelin and that several other bands also display genotype-dependent differences in intensity. Gel shows n=2 biological replicates representative of n=3 biological replicates.

**(B)** The relative abundance of proteins in myelin purified from *Prx*$^{-/-}$ sciatic nerves as quantified by MS$^{E}$ is given as percent with relative standard deviation (% +/- RSD). Note the increased relative abundance of MPZ/P0 and MBP compared to wild-type myelin (see **Figure 2**) when PRX is lacking. Mass spectrometric quantification based on 3 biological replicates with 4 technical replicates each (see **Figure 5-source data 1**).

**(C,D)** Differential proteome analysis by DRE-UDMS$^{E}$ of myelin purified from *Prx*$^{-/-}$ and wild-type mice. Mass spectrometric quantification based on 3 biological replicates per genotype with 4 technical replicates each (see **Figure 5-source data 2**). **(C)** Top 40 proteins of which the abundance is reduced (blue) or increased (red) in peripheral myelin purified from *Prx*$^{-/-}$ compared to wild-type mice with the highest level of significance according to the -$\log_{10}$ transformed q-value (green). In the heatmaps, each horizontal line corresponds to the fold-change (FC) of a distinct protein compared to its average abundance in wild-type myelin plotted on a $\log_2$ color scale. Heatmaps display 12 replicates, i.e. 3 biological replicates per genotype with 4 technical replicates each. **(D-D‘‘‘)** Volcano plots representing genotype-dependent quantitative myelin proteome analysis. Data points represent quantified proteins in *Prx*$^{-/-}$ compared to wild-type myelin and are plotted as the log2-transformed fold-change (FC) on the x-axis against the -log10-transformed q-value on the y-axis. Stippled lines mark a -log10-transformed q-value of 1.301, reflecting a q-value of 0.05 as significance threshold. Highlighted are the datapoints representing the Top 10 proteins displaying highest zdist values (Euclidean distance between the two points (0,0) and (x,y) with x = log2(FC) and y = -log10(q-value) (red circles in **D**), immune-related proteins (purple circles in **D‘**), proteins of the extracellular matrix (ECM; yellow circles in **D‘‘**) and known myelin proteins (blue circles in **D‘‘‘**). n.d., not detected; n.q., no q-value computable due to protein identification in one genotype only. Also see **Figure 5-supplement 1.**

**(E)** Immunoblot of myelin purified from *Prx*$^{-/-}$ and control sciatic nerves confirms the reduced abundance of DRP2, SLC16A1/MCT1, BSG and PMP2 in *Prx*$^{-/-}$ myelin, as found by

differential DRE-UDMS$^{E}$ analysis (in **Figure 5C,D**). PRX was detected as genotype control; PLP/DM20 and ATP1A1 serve as markers. Blot shows n=2 biological replicates per genotype.

**(F)** Teased fiber preparations of sciatic nerves dissected from *Prx*$^{-/-}$ and control mice immunolabelled for MAG (red) and SLC16A1 (green). Note that SLC16A1 co-distributes with MAG in Schmidt-Lanterman incisures (SLI) in control but not in *Prx*$^{-/-}$ nerves, in accordance with the reduced abundance of SLC16A1 in *Prx*$^{-/-}$ myelin (**Figure 5C-E**). Also note that, in *Prx*$^{-/-}$ myelin, SLI were largely undetectable by MAG immunolabeling.

**Figure 5-supplement 1. Clustered heatmap of Pearson's correlation coefficients for protein abundance comparing genotypes.**

**(A)** The heatmap compares the $\log_2$ transformed ppm protein abundance values from the DRE-UDMS$^{E}$ runs to assess peripheral myelin purified from wild type and *Prx*$^{-/-}$ mice. The inset shows the color key and the histogram for the values of the correlation coefficients. Note that the runs cluster with a high overall correlation (>0.85) into two conditions defined by the genotype, in agreement with the experimental design.

**(B)** Volcano plot representing genotype-dependent quantitative myelin proteome analysis. Data points represent quantified proteins in *Prx*$^{-/-}$ compared to wild-type myelin plotted as the log2-transformed fold-change (FC) on the x-axis against the -log10-transformed q-value on the y-axis. Note the different axis scale compared to **Figure 5D**. Stippled line marks a -log10-transformed q-value of 1.301, reflecting a q-value of 0.05 as significance threshold. Highlighted is the datapoint for PRX to illustrate that only trace amounts of PRX were detected when assessing *Prx*$^{-/-}$ myelin. ATP2A1, ATP1A4 and PLCD1 were not detected in *Prx*$^{-/-}$ myelin.

**Figure 6. Progressive loss and reduced diameters of peripheral axons in *Prx*$^{-/-}$ mice**

**(A-D)** Genotype-dependent quantitative assessment of light micrographs of toluidine-stained semi-thin sectioned quadriceps nerve dissected at 2, 4 and 9 months of age reveals progressive loss of peripheral axons in *Prx*$^{-/-}$ compared to control mice.

**(A)** Representative micrographs. Arrows point at myelinated axons; asterisk denotes an unmyelinated axon; arrowhead points at a myelin whorl lacking a recognizable axon. Scale bars, 10 µm.

**(B)** Total number of axons per nerve that are not associated with a Remak bundle.

**(C)** Total number of myelinated axons per nerve.

**(D)** Total number per nerve of myelin whorls that lack a recognizable axon.

Mean +/ SD, n=3-4 mice per genotype and age; *P<0.05, **P<0.01, ***P<0.001 by Student's unpaired t-test.

(**E-G**) Genotype-dependent assessment of myelinated axons shows a shift toward reduced axonal diameters in quadriceps nerves of *Prx*$^{-/-}$ compared to control mice at 2 months **(E)**, 4 months **(F)** and 9 months **(G)** of age. Data are presented as frequency distribution with 0.5 µm bin width. ***, p<0.001 by two-sided Kolmogorow-Smirnow test. For precise p-values see methods section.

**Figure 1-source data 1. Label-free quantification of proteins in wild-type PNS myelin fractions by three different data acquisition modes**

Identification and quantification data of detected myelin-associated proteins. Tryptic peptides derived from four technical replicates (replicate digestion and replicate injection) per three biological replicate (20 sciatic nerves pooled from 10 animals) were analyzed by LC-MS (12 runs in total). Proteins (FDR < 1%; 2 peptides/protein) and peptides (FDR < 1%; ≥7 amino acids) were identified by database search against the UniprotKB/SwissProt mouse database using PLGS. Data were post-processed with the software package ISOQuant to calculate absolute in-sample amounts for each detected protein based on the TOP3 approach. Reported abundance values are defined as the relative amount of each protein in respect to the sum over all detected proteins (ppm: parts per million (w/w) of total protein). Typical contaminant proteins like keratins were filtered.

→ sheet 1: protein identification details

→ sheet 2: WT myelin proteome by MS$^{E}$

→ sheet 3: WT myelin proteome by UD-MS$^{E}$

→ sheet 4: WT myelin proteome by DRE UD-MS$^{E}$

→ sheet 5: 45 proteins additionally identified in WT myelin by 1D-gel-LC-MS

**Figure 3-source data 1. Normalized developmental mRNA abundance data**

→ sheet 1: normalized values for all individual 4 biological replicates per age

→ sheet 2: normalized values for biological replicates averaged to give mean per age

**Figure 5-source data 1. Label-free quantification of proteins in PNS myelin fractions from *Prx*$^{-/-}$ mice by MSe**

Identification and quantification data of detected myelin-associated proteins. Tryptic peptides derived from four technical replicates (replicate digestion and replicate injection) per three

biological replicate (20 sciatic nerves pooled from 10 animals) were analyzed by LC-MS (12 runs in total). Proteins (FDR < 1%; 2 peptides/protein) and peptides (FDR < 1%; ≥7 amino acids) were identified by database search against the UniprotKB/SwissProt mouse database using PLGS. Data were post-processed with the software package ISOQuant to calculate absolute in-sample amounts for each detected protein based on the TOP3 approach. Reported abundance values are defined as the relative amount of each protein in respect to the sum over all detected proteins (ppm: parts per million (w/w) of total protein). Typical contaminant proteins like keratins were filtered.

→ sheet 1: protein identification details

→ sheet 2: *Prx*$^{-/-}$ myelin proteome by MS$^{E}$

**Figure 5-source data 2. Label-free quantification of proteins in PNS myelin fractions from WT and *Prx*$^{-/-}$ mice by DRE-UDMSe**

Identification and quantification data of detected myelin-associated proteins by DRE-UDMSe. For each genotype, tryptic peptides derived from four technical replicates (replicate digestion and replicate injection) per three biological replicate (20 sciatic nerves pooled from 10 animals) were analyzed by LC-MS (24 runs in total). Proteins (FDR < 1%; 2 peptides/protein) and peptides (FDR < 1%; ≥7 amino acids) were identified by database search against the UniprotKB/SwissProt mouse database using PLGS. Data were post-processed with the software package ISOQuant to calculate absolute in-sample amounts for each detected protein based on the TOP3 approach. Reported abundance values are defined as the relative amount of each protein in respect to the sum over all detected proteins (ppm: parts per million (w/w) of total protein). Typical contaminant proteins like keratins were filtered. The -log10-transformed q-value was plotted against the log2-transformed fold change to obtain the volcano plot shown in Figure 5D. As no imputation of missing values was performed, proteins exclusive for only one of the conditions do not appear in the volcano plot, but are appended at the end of the list. Criteria for statistically significant regulation were as follows: fold change of at least 1.5 and q-value below 0.05.

→ sheet 1: protein identification details

→ sheet 2: comparison of WT vs. *Prx*$^{-/-}$ myelin proteome by DRE-UDMS$^{E}$

| Protein name | Gene | Reference | TMD | Cluster |
|---|---|---|---|---|
| 2-hydroxyacylsphingosine 1-beta-galactosyltransferase | *Ugt8* | Bosio et al., 1996 | 2 | P6-up |
| Syntrophin α1 | *Snta1* | Fuhrmann-Stroissnigg et al., 2012 | - | P18-up |
| Annexin A2 | *Anxa2* | Hayashi et al., 2007 | - | Descending |
| Band 4.1 protein B / 4.1B | *Epb41l3* | Ivanovic et al., 2012 | - | Descending |
| Band 4.1 protein G / 4.1G | *Epb41l2* | Ohno et al., 2006 | - | P6-up |
| Breast carcinoma-amplified sequence 1 | *Bcas1* | Ishimoto et al., 2017 | - | P6-up |
| Cadherin 1/ E-Cadherin | *Cdh1* | Fannon et al., 1995 | 1 | P18-up |
| Carbonic anhydrase 2 | *Ca2* | Cammer et al., 1987 | - | Descending |
| Catenin α1 | *Ctnna1* | Murata et al., 2006 | - | U-shaped |
| Catenin ß1 | *Ctnnb1* | Fannon et al., 1995 | - | Descending |
| Caveolin 1 | *Cav1* | Mikol et al., 2002 | 1 | P18-up |
| CD9, tetraspanin 29 | *Cd9* | Ishibashi et al., 2004 | 4 | P18-p |
| CD59A | *Cd59a* | Funabashi et al., 1994 | 1 | P18-up |
| CD47, integrin-associated signal transducer | *Cd47* | Gitik et al., 2011 | 5 | P6-up |
| CD81, tetraspanin 28 | *Cd81* | Ishibashi et al., 2004 | 4 | P18-up |
| CD82, tetraspanin 27 | *Cd82* | Chernousov et al., 2013 | 4 | P18-up |
| CD151, tetraspanin 24 | *Cd151* | Patzig et al., 2011 | 4 | P18-up |
| Cell adhesion molecule 4/ NECL4 | *Cadm4* | Spiegel et al., 2007 | 1 | P6-up |
| Cell division control protein 42 | *Cdc42* | Benninger et al., 2007 | - | P6-up |
| Cell surface glycoprotein MUC18 | *Mcam* | Shi et al., 1998 | 1 | Descending |
| Ciliary neurotrophic factor | *Cntf* | Rende et al., 1992 | - | Late-up |
| CKLF-like MARVEL TMD-containing 5 | *Cmtm5* | Patzig et al., 2011 | 4 | P6-up |
| Claudin-19 | *Cldn19* | Miyamoto et al., 2005 | 4 | P6-up |
| Cofilin 1 | *Cfl1* | Sparrow et al., 2012 | - | Descending |
| Crystallin α2 | *Cryab* | d'Antonio et al., 2006 | - | P18-up |
| Cyclic nucleotide phosphodiesterase | *Cnp* | Matthieu et al., 1980 | - | P6-up |
| Sarcoglycan δ | *Sgcd* | Cai et al., 2007 | 1 | Late-up |
| Dihydropyrimidinase related protein 1 | *Crmp1* | d'Antonio et al., 2006 | - | Descending |
| Disks large homolog 1 | *Dlg1* | Cotter et al., 2010 | - | Descending |
| Dynein light chain 1 | *Dynll1* | Myllykoski et al. 2018 | - | P6-up |
| Dystroglycan | *Dag1* | Yamada et al, 1994 | 1 | P6-up |
| Dystrophin/DP116 | *Dmd* | Cai et al., 2007 | - | P6-up |
| Dystrophin-related protein 2 | *Drp2* | Sherman et al., 2001 | - | P18-up |
| E3 ubiquitin-protein ligase NEDD4 | *Nedd4* | Liu et al., 2009 | - | Descending |
| Ezrin | *Ezr* | Scherer et al., 2001 | - | P6-up |
| Fatty acid synthase | *Fasn* | Salles et al., 2002 | - | P6-up |
| Flotillin 1 | *Flot1* | Lee et al., 2014 | - | P18-up |
| Gap junction ß1 protein / Cx32 | *Gjb1* | Li et al., 2002 | 4 | P18-up |
| Gap junction γ3 protein / Cx29 | *Gjc3* | Li et al., 2002 | 1 | P6-up |
| Gelsolin | *Gsn* | Gonçalves et al., 2010 | - | Late-up |
| Glycogen synthase kinase 3ß | *Gsk3b* | Ogata et al., 2004 | - | P6-up |
| Integrin α6 | *Itga6* | Nodari et al., 2008 | 1 | P6-up |
| Integrin αV | *Itgav* | Chernousov & Carey, 2003 | 1 | Descending |
| Integrin ß1 | *Itgb1* | Feltri et al., 2002 | 1 | Descending |
| Integrin ß4 | *Itgb4* | Quattrini et al., 1996 | 2 | P18-up |
| Junctional adhesion molecule C | *Jam3* | Scheiermann et al., 2007 | 1 | P18-up |
| Laminin α2 | *Lama2* | Yang et al., 2005 | - | P6-up |
| Laminin α4 | *Lama4* | Yang et al., 2005 | - | Descending |
| Laminin ß1 | *Lamb1* | LeBeau et al., 1994 | - | Descending |
| Laminin ß2 | *Lamb2* | LeBeau et al., 1994 | - | P18-up |
| Laminin γ1 | *Lamc1* | Chen & Strickland, 2003 | - | Descending |
| Membrane Palmitoylated Protein 6 | *Mpp6* | Saitoh et al., 2019 | - | P6-up |
| Microtubule-associated protein 1A | *Map1a* | Fuhrmann-Stroissnigg et al., 2012 | - | P18-up |
| Microtubule-associated protein 1B | *Map1b* | Fuhrmann-Stroissnigg et al., 2012 | - | P6-up |
| Mitogen-activated protein kinase 1/ ERK2 | *Mapk1* | Mantuano et al., 2015 | - | Descending |
| Mitogen-activated protein kinase 3/ ERK1 | *Mapk3* | Mantuano et al., 2015 | - | P18-up |
| Moesin | *Msn* | Scherer et al., 2001 | - | Unchanged |
| Monocarboxylate transporter 1 | *Slc16a1* | Domenech-Estevez et al., 2015 | 11 | P18-up |

| | | | | |
|---|---|---|---|---|
| Myelin associated glycoprotein | *Mag* | Figlewicz et al., 1981 | 1 | P6-up |
| Myelin basic protein | *Mbp* | Boggs, 2006 | - | P6-up |
| Myelin protein 2 | *Pmp2* | Trapp et al., 1984 | - | P18-up |
| Myelin protein zero/ P0 | *Mpz* | Giese et al., 1992 | 1 | P6-up |
| Myelin proteolipid protein | *Plp1* | Garbern et al., 1997 | 4 | P6-up |
| Myotubularin-related protein 2 | *Mtmr2* | Bolino et al., 2004 | - | P6-up |
| Noncompact myelin-associated protein | *Ncmap* | Ryu et al., 2008 | 1 | P18-up |
| NDRG1, N-myc downstream regulated | *Ndrg1* | Berger et al., 2004 | - | P18-uP |
| Neurofascin | *Nfasc* | Tait et al., 2000 | 2 | P18-up |
| Nidogen 1 | *Nid1* | Lee et al., 2007 | - | Descending |
| P2X purinoceptor 7 | *P2rx7* | Faroni et al., 2014 | - | P6-up |
| Paxillin | *Pxn* | Fernandez-Valle et al., 2002 | - | P6-up |
| Periaxin | *Prx* | Gillespie et al., 1994 | - | P6-up |
| Plasmolipin | *Pllp* | Bosse et al., 2003 | 4 | P18-up |
| Profilin 1 | *Pfn1* | Montani et al., 2014 | - | Descending |
| Lin-7 homolog C | *Lin7c* | Saitoh et al., 2017 | - | P6-up |
| Rac1 | *Rac1* | Benninger et al., 2007 | - | U-Shaped |
| Radixin | *Rdx* | Scherer et al., 2001 | - | Descending |
| RhoA | *Rhoa* | Brancolini et al., 1999 | - | U-Shaped |
| Septin 2 | *Sept 2* | Buser et al., 2009 | - | Descending |
| Septin 7 | *Sept 7* | Buser et al., 2009 | - | U-Shaped |
| Septin 8 | *Sept 8* | Patzig et al., 2011 | - | P18-up |
| Septin 9 | *Sept 9* | Patzig et al., 2011 | - | P6-up |
| Septin 11 | *Sept 11* | Buser et al., 2009 | - | Descending |
| Sirtuin 2, NAD-dependent deacetylase | *Sirt2* | Werner et al., 2007 | - | P18-up |
| Spectrin alpha chain, non-erythrocytic 1 | *Sptan1* | Susuki et al., 2018 | - | P18-up |
| Spectrin beta chain, non-erythrocytic 1 | *Sptbn1* | Susuki et al., 2018 | - | P18-up |
| Tight junction protein ZO-1 | *Tjp1* | Poliak et al., 2007 | - | P6-up |
| Tight junction protein ZO-2 | *Tjp2* | Poliak et al., 2007 | - | P6-up |
| Transferrin | *Tf* | Liu et al., 1990 | 2 | Late-up |
| Vimentin | *Vim* | Triolo et al., 2012 | - | Unchanged |
| Vinculin | *Vcl* | Beppu et al., 2015 | - | Descending |

**Table 1. Known myelin proteins in the myelin proteome.** Proteins mass-spectrometrically identified in peripheral myelin are compiled according to availability of prior references as myelin proteins. Given are the official gene name, one selected reference, the number of transmembrane domains (TMD) and the mRNA abundance profile cluster (see **Figure 3**).

| Protein name | Gene name | OMIM# | Gene Locus | Neuropathy |
|---|---|---|---|---|
| Monoacylglycerol lipase ABHD12 | *ABHD12* | 613599 | 20p11.21 | PHARC |
| Apoptosis-inducing factor 1 | *AIFM1* | 300169 | Xq26.1 | CMTX4, DFNX5 |
| Na+/K+ -transporting ATPase α1 | *ATP1A1* | 182310 | 1p13.1 | CMT2DD |
| Cytochrome c oxidase subunit 6A1 | *COX6A1* | 602072 | 12q24.31 | CMTRID |
| Dystrophin-related protein 2 | *DRP2* | 300052 | Xq22.1 | CMTX |
| Dynactin subunit 1 | *DCTN1* | 601143 | 2p13.1 | DHMN7B |
| Dynamin 2 | *DNM2* | 602378 | 19p13.2 | CMT2M, CMTDIB |
| Cytoplasmic dynein 1 heavy chain 1 | *DYNC1H1* | 600112 | 14q32.31 | CMT20, SMALED1 |
| E3 SUMO-protein ligase | *EGR2* | 129010 | 10q21.3 | CMT1D, CMT3, CMT4E |
| Glycine-tRNA ligase | *GARS* (Gart) | 600287 | 7p14.3 | CMT2D, HMN5A |
| Gap junction ß1 protein / Cx32 | *GJB1* | 304040 | Xq13.1 | CMTX1 |
| Guanine nucleotide-binding protein ß4 | *GNB4* | 610863 | 3q26.33 | CMTDIF |
| Histidine triad nucleotide-binding protein 1 | *HINT1* | 601314 | 5q23.3 | NMAN |
| Hexokinase 1 | *HK1* | 142600 | 10q22.1 | CMT4G |
| Heat shock protein ß1 | *HSPB1* | 602195 | 7q11.23 | CMT2F, DHMN2B |
| Kinesin heavy chain isoform 5A | *KIF5A* | 602821 | 12q13.3 | SPG10 |
| Prelamin A/C | *LMNA* | 150330 | 1q22 | CMT2B1 |
| Neprilysin | *MME* | 120520 | 3q25.2 | CMT2T, SCA43 |
| Myelin protein zero/ P0 | *MPZ* | 159440 | 1q23.3 | CHN2,CMT1B, CMT2I, CMT2J,CMT3, CMTDID, Roussy-Levy syndrome |
| Myotubularin-related protein 2 | *MTMR2* | 603557 | 11q21 | CMT4B1 |
| Alpha-N-acetylglucosaminidase | *NAGLU* (NAGA) | 609701 | 17q21.2 | CMT2V |
| NDRG1, N-myc downstream regulated | *NDRG1* | 605262 | 8q24.22 | CMT4D |
| Neurofilament heavy polypeptide | *NEFH* | 162230 | 22q12.2 | CMT2CC |
| Neurofilament light polypeptide | *NEFL* | 162280 | 8p21.2 | CMT2E, CMT1F, CMTDIG |
| Peripheral myelin protein 2 | *PMP2* | 170715 | 8q21.13 | CMT1G |
| Peripheral myelin protein 22 | *PMP22* | 601907 | 17p12 | CMT1A, CMT1E, CMT3, HNPP, Roussy-Levy syndrome |
| Ribose-phosphate pyrophosphokinase 1 | *PRPS1* | 311850 | Xq22.3 | Arts syndrome, CMTX5, DFNX1 |
| Periaxin | *PRX* | 605725 | 19q13.2 | CMT4F, CMT3 |
| Ras-related protein Rab 7a | *RAB7A* | 602298 | 3q21.3 | CMT2B |
| Septin 9 | *SEPT9* | 604061 | 17q25.3 | HNA |
| Transitional ER-ATPase | *VCP* | 601023 | 9p13.3 | CMT2Y |
| Tryptophan-tRNA ligase, cytoplasmic | *WARS* | 191050 | 14q32.32 | HMN9 |
| Tyrosine-tRNA ligase, cytoplasmic | *YARS* | 603623 | 1p35.1 | DI-CMTC |

**Table 2. Peripheral myelin proteins identified in PNS myelin involved in neuropathological diseases.** Proteins massspectrometically identified in peripheral myelin were analyzed regarding the involvement of the ortholog human gene in neuropathological diseases. PMP22 was added, though it was not identified by MS analyses due to its unfavorable distribution of tryptic cleavage sites. CMT, Charcot-Marie-Tooth disease; DHMN, distal hereditary motor neuropathy; DI-CMTC, dominant intermediate CMTC; DFN, X-linked deafness; HMN, hereditary motor neuropathy; HSAN, hereditary sensory and autonomic neuropathy; HNA, hereditary sensory and autonomic neuropathy; OMIM, Online Mendelian Inheritance in Man; PHARC, polyneuropathy, hearing loss, ataxia, retinitis pigmentosa and cataract; SCA, spinocerebellar ataxia; SPG, spastic paraplegia.

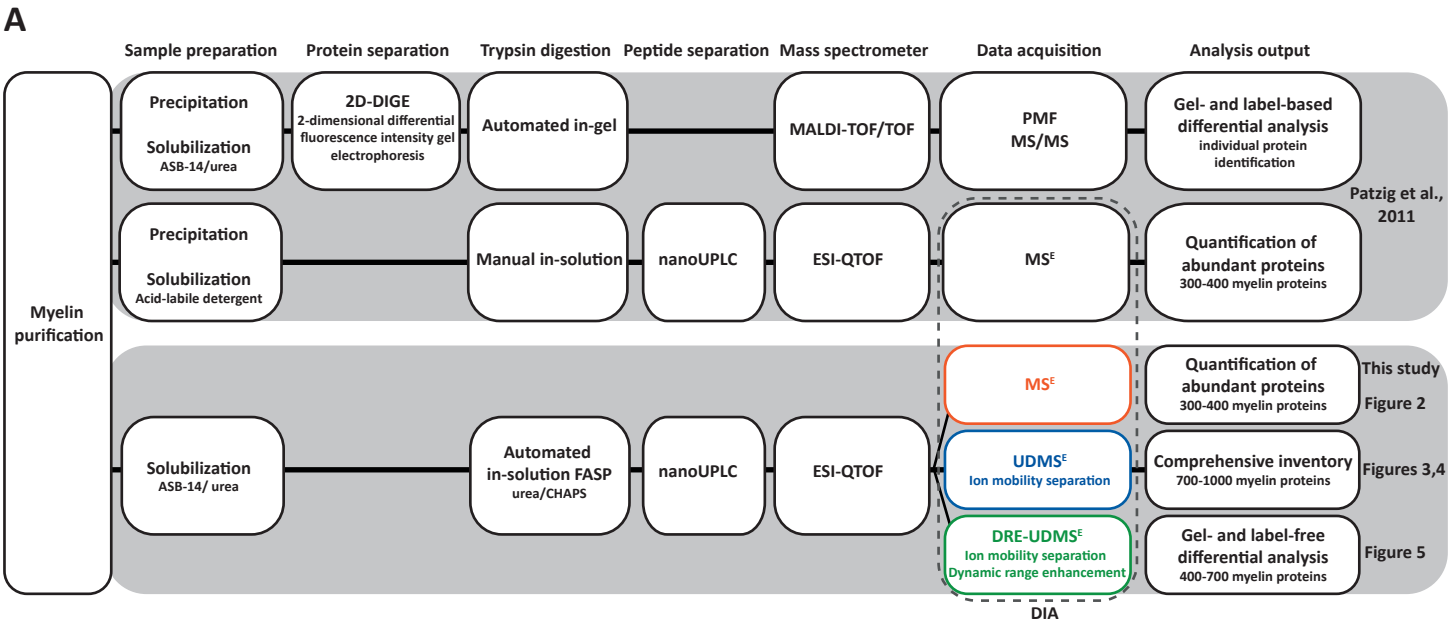
A
Sample preparation
Protein separation
Trypsin digestion
Peptide separation
Mass spectrometer
Data acquisition
Analysis output
Myelin purification
Precipitation
Solubilization
ASB-14/urea
2D-DIGE
2-dimensional differential fluorescence intensity gel electrophoresis
Automated in-gel
MALDI-TOF/TOF
PMF
MS/MS
Gel- and label-based differential analysis
individual protein identification
Patzig et al., 2011
Precipitation
Solubilization
Acid-labile detergent
Manual in-solution
nanoUPLC
ESI-QTOF
MSE
Quantification of abundant proteins
300-400 myelin proteins
Solubilization
ASB-14/ urea
Automated in-solution FASP
urea/CHAPS
nanoUPLC
ESI-QTOF
MSE
Quantification of abundant proteins
300-400 myelin proteins
This study
Figure 2
UDMSE
Ion mobility separation
Comprehensive inventory
700-1000 myelin proteins
Figures 3,4
DRE-UDMSE
Ion mobility separation
Dynamic range enhancement
Gel- and label-free differential analysis
400-700 myelin proteins
Figure 5
DIA

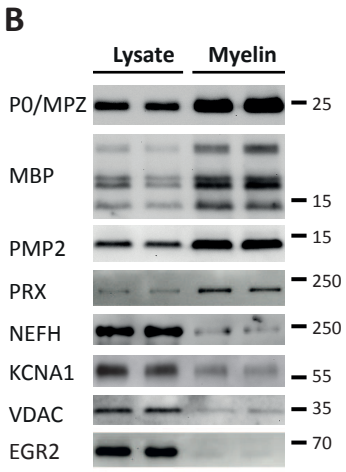
B
Lysate
Myelin
P0/MPZ
25
MBP
15
PMP2
15
PRX
250
NEFH
250
KCNA1
55
VDAC
35
EGR2
70

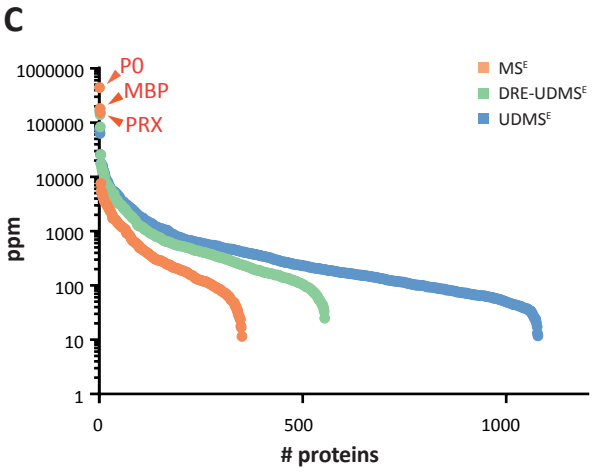
C
1000000
100000
10000
1000
100
10
1
ppm
0
500
1000
# proteins
P0
MBP
PRX
MSE
DRE-UDMSE
UDMSE

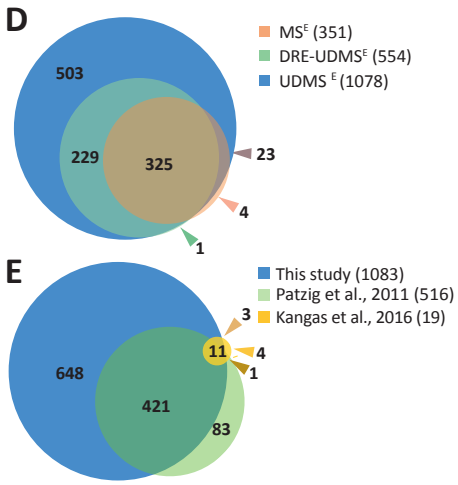
D
503
229
325
23
4
1
MSE (351)
DRE-UDMSE (554)
UDMS E (1078)
E
648
421
83
11
3
4
1
This study (1083)
Patzig et al., 2011 (516)
Kangas et al., 2016 (19)

**Siems et al., Figure 1-supplement 1**

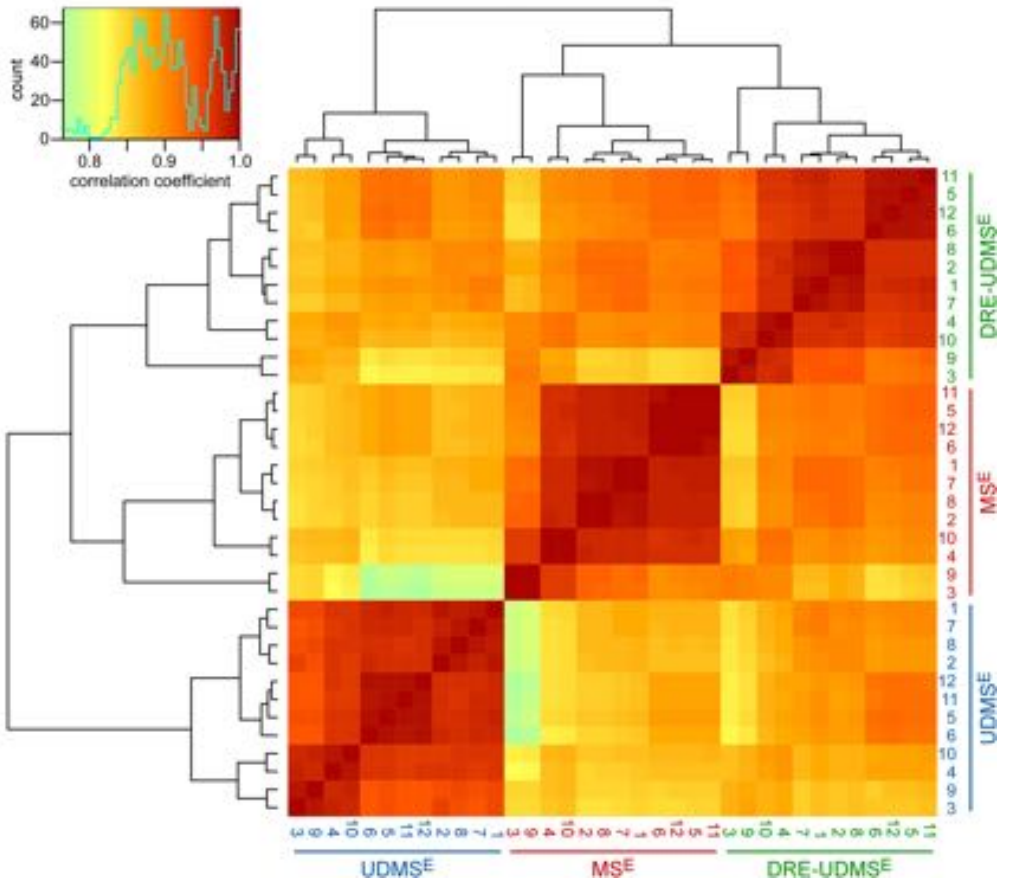

# Siems et al., Figure 2

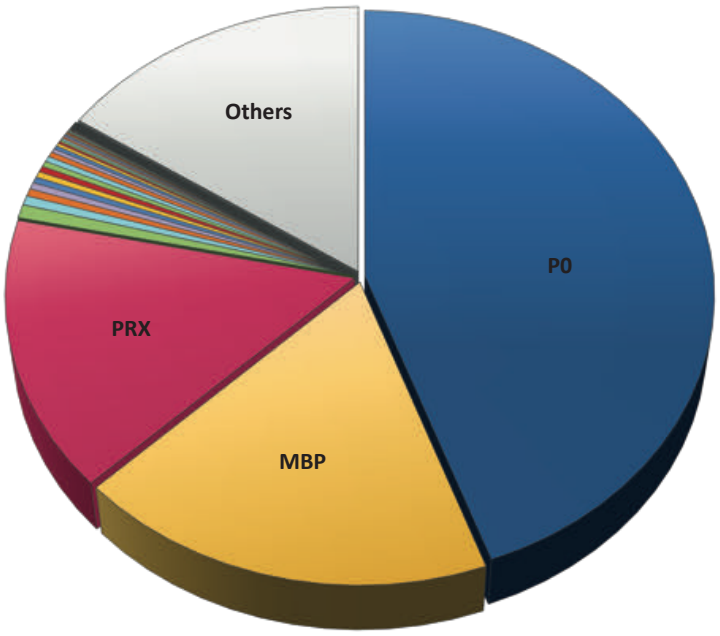


| Protein | % (+/- | RSD) | Protein | % (+/- | RSD) |
|---|---|---|---|---|---|
| P0/ MPZ | 44.48 | 4.15 | LAMC1 | 0.06 | 0.01 |
| MBP | 18.35 | 1.15 | RAC1 | 0.05 | 0.01 |
| PRX | 15.48 | 1.46 | VCL | 0.04 | 0.00 |
| CD9 | 0.77 | 0.15 | CA2 | 0.04 | 0.01 |
| SPTBN1 | 0.52 | 0.06 | SEPT2 | 0.04 | 0.00 |
| SPTAN1 | 0.42 | 0.07 | CFL1 | 0.04 | 0.01 |
| EPB41L2 | 0.38 | 0.05 | CRYAB | 0.03 | 0.00 |
| VIM | 0.34 | 0.07 | MPP6 | 0.03 | 0.00 |
| CNP | 0.33 | 0.06 | CAV1 | 0.03 | 0.00 |
| TF | 0.33 | 0.03 | SEPT7 | 0.02 | 0.00 |
| PMP2 | 0.32 | 0.03 | GJC3 | 0.02 | 0.00 |
| MAP1B | 0.31 | 0.06 | RDX | 0.02 | 0.00 |
| FASN | 0.29 | 0.04 | CDC42 | 0.02 | 0.01 |
| ANXA2 | 0.22 | 0.03 | PFN1 | 0.02 | 0.00 |
| MAG | 0.20 | 0.02 | SEPT11 | 0.02 | 0.00 |
| PLP1 | 0.17 | 0.02 | CRMP1 | 0.02 | 0.00 |
| CD81 | 0.12 | 0.01 | RHOA | 0.02 | 0.00 |
| GSN | 0.11 | 0.02 | MAPK3 | 0.02 | 0.00 |
| PLLP | 0.11 | 0.01 | MAPK1 | 0.01 | 0.00 |
| BCAS1 | 0.09 | 0.00 | CMTM5 | 0.01 | 0.00 |
| NDRG1 | 0.09 | 0.03 | JAM3 | 0.01 | 0.00 |
| MSN | 0.09 | 0.01 | DYNLL1 | 0.01 | 0.03 |
| EPB41L3 | 0.07 | 0.01 | EZR | 0.01 | 0.00 |
| NID1 | 0.07 | 0.01 | CD59A | 0.01 | 0.00 |
| CADM4 | 0.07 | 0.01 | Others | 15.39 | |

# A

## P6-up

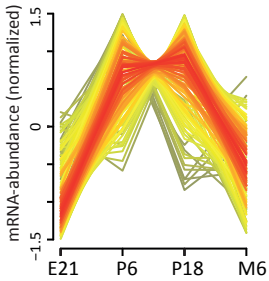


| | | | | | | | | | |
|---|---|---|---|---|---|---|---|---|---|
| Aacs | **Cd47** | Cpne3 | Eml1 | Gmfb | **Lama2** | **Mpp6** | Osbpl1a | Pygb | **Tjp1** |
| Abcd3 | **Cdc42** | Cpt1a | **Epb41l2** | Gna11 | Letm1 | **Mpz** | **P2rx7** | Rab8b | **Tjp2** |
| Acaca | Cfl2 | Csnk2a1 | **Ezr** | Gnai1 | **Lin7c** | **Mtmr2** | Pdhb | Rcn1 | Tspan15 |
| Acat2 | Ckb | Cyp51 | Fam177a1 | Gnaq | Lss | Mvk | Pgls | Rer1 | Tubb2a |
| Adam10 | **Cldn19** | **Dag1** | Far1 | Gng2 | M6pr | Myh14 | Plg | Rpl13 | Ubl3 |
| Agps | **Cmtm5** | Dhcr7 | **Fasn** | **Gsk3b** | **Mag** | Myo18a | **Plp1** | Rps16 | **Ugt8** |
| Appl1 | **Cnp** | Dhrs1 | Fdft1 | Gypc | **Map1b** | Naga | **Pmp22** | Rps2 | |
| Art3 | Col15a1 | **Dmd** | Fdps | Hmgcs1 | Map4 | Napb | Ppa2 | **Sept9** | |
| **Bcas1** | Col1a1 | Dusp15 | Fmnl2 | Hsd17b7 | Map6 | Ndufb7 | Prkacb | Slc25a10 | |
| Bdh1 | Col1a2 | Dync1h1 | Fscn1 | Idi1 | Mapre3 | Ndufs8 | **Prx** | Slc25a5 | |
| Brox | Col28a1 | **Dynll1** | Fut8 | **Itga6** | **Mbp** | Nefl | Psmb6 | Slc44a1 | |
| Cab39l | Col4a2 | Eci1 | Gamt | Itpr3 | Mical1 | Nefm | Psmc3 | Snap91 | |
| **Cadm4** | Col6a1 | Ehd3 | Gapdhs | Kif5b | Mlec | Nsdhl | Pura | Sorbs1 | |
| Camk2b | Col6a2 | Elovl1 | **Gjc3** | Klc2 | Mme | Opa1 | **Pxn** | Stk39 | |

## P18-up

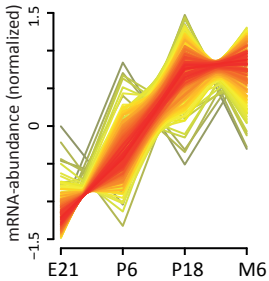


| | | | | | | | | | | | | | | |
|---|---|---|---|---|---|---|---|---|---|---|---|---|---|---|
| Abat | Aldh9a1 | Atp6v1e1 | **Cd59** | **Cryab** | Fkbp1a | Hibch | **Lamb2** | Mpc1 | Ndufs4 | **Pmp2** | Rab5b | Serpinf1 | Steap3 | Tst |
| Abhd12 | Anxa11 | Atp6v1h | **Cd81** | Ctsd | Flnb | Hk1 | Lamp1 | Mpp2 | Ndufs7 | Por | Rab7a | Sft2d2 | Stx12 | Tubb4a |
| Acaa1a | Anxa5 | Auh | **Cd82** | Cyb5a | **Flot1** | Hras | Lamp2 | Mpst | Ndufv2 | Prdx5 | Rdh11 | Sfxn3 | Stxbp1 | Vat1l |
| Acaa2 | Arl3 | Bcap31 | **Cd9** | Cyb5r3 | Gatm | Hsd17b10 | Lancl1 | Myh9 | Nes | Prelp | Reep5 | **Sirt2** | Sucla2 | Vps26a |
| Acadm | Arl8b | Bgn | **Cdh1** | Ddah1 | Gdi1 | Hsd17b11 | Ldhb | Myo1b | **Nfasc** | Prkca | Rida | **Slc16a1** | Sult1a1 | Vps29 |
| Acads | Asah1 | Bphl | Cdipt | Decr1 | **Gjb1** | Hsd17b12 | Limch1 | Myo1c | Nptn | Psmf1 | Rtkn | Slc25a1 | Susd2 | Vsnl1 |
| Acadvl | Asl | **Bsg** | Cers2 | Dnm1 | Glod4 | Hsd17b4 | Maoa | Ncdn | Ostf1 | Rab11b | Rtn4 | Slc2a1 | Svip | Ywhaq |
| Acsl1 | Atp1a1 | **Cadm3** | Chchd3 | Dpysl2 | Glul | Hspa12a | **Map1a** | **Ncmap** | Pcolce | Rab12 | Rufy3 | Slc3a2 | Sypl1 | |
| Acss2 | Atp1a2 | Canx | Clip2 | **Drp2** | Gnao1 | Hspa1a | Map1lc3a | **Ndrg1** | Pdcd6ip | Rab21 | S100a6 | Slc44a2 | Taldo1 | |
| Ak3 | Atp1a4 | Capn1 | Cmtm6 | Ech1 | Gpi | Hspa2 | Map1lc3b | Ndrg2 | Pfkm | Rab2a | Sacm1l | **Snta1** | Tecr | |
| Aldh1a1 | Atp1b3 | Capn2 | Cndp2 | Eno2 | Hadh | **Itgb4** | **Mapk3** | Ndrg4 | Phb | Rab2b | Sbds | Sod2 | Tkt | |
| Aldh1a7 | Atp6v0c | **Cav1** | Comt | Etfb | Hagh | **Jam3** | Marc2 | Ndufa13 | Plec | Rab3a | Scarb2 | Sparc | Tln1 | |
| Aldh3a2 | Atp6v1c1 | Cavin3 | Copg2 | Fam213a | Hepacam | Jup | Mgll | Ndufa7 | Plekhb1 | Rab43 | Scp2 | **Sptan1** | Tns3 | |
| Aldh6a1 | Atp6v1d | **Cd151** | Crip2 | Fis1 | Hibadh | Kit | Mgst3 | Ndufb4 | **Pllp** | Rab4b | **Sept8** | **Sptbn1** | Tom1l2 | |

## Late-up

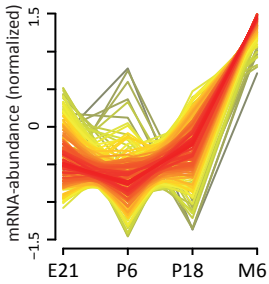


| | | | | | | | | | | | | | |
|---|---|---|---|---|---|---|---|---|---|---|---|---|---|
| Actn3 | Arpc4 | Cab39 | Cfh | Des | Esyt1 | Got2 | Idh3g | Myl6 | Pdha1 | Rab18 | Rras | Stx7 | Uqcrb |
| Ahcy | Aspa | Camk2g | Cisd1 | Dnajb4 | Etfa | Gpd1 | Ivd | Myl9 | Pdlim5 | Rab5c | Rras2 | Tagln | Vat1 |
| Akr1b1 | Atp12a | Capg | Ckm | Dnpep | F13a1 | Gpd1l | Lap3 | Ndufa5 | Pebp1 | Rhob | Rtn1 | Tagln3 | Vwa5a |
| Aldh2 | Atp1a3 | Capns1 | Ckmt1 | Dstn | Fabp4 | Gpx3 | Lcp1 | Ndufa6 | Pfkp | Rhog | S100b | **Tf** | Zc2hc1a |
| Aldoa | Atp1b1 | Capzb | **Cntf** | Dusp3 | Fam129b | Gpx4 | Lypla2 | Ndufa8 | Pgam2 | Rpl12 | Sbspon | Tomm34 | |
| Aldoc | Atp2b2 | Car3 | **Cntn1** | Dynll2 | Fbxo2 | **Gsn** | Lyz2 | Ndufb10 | Picalm | Rpl13a | Sdha | Tpi1 | |
| Anpep | Atp5f1d | Cast | Coro1a | Echs1 | Fgg | Gstk1 | Macrod1 | Ndufb3 | Pkm | Rpl19 | Serpinb6a | Tpm1 | |
| Anxa1 | Atp5mg | Cat | Cox4i1 | Eef1a2 | Flot2 | Gstm1 | Mapt | Ndufb6 | Plin1 | Rpl26 | Serping1 | Tppp3 | |
| Anxa3 | Atp6v1g1 | Cav2 | Cox6c | Ehd2 | Fn3krp | Gstm2 | Mdh1 | Ndufc2 | Plin3 | Rpl29 | Sfn | Tsg101 | |
| Anxa7 | Bag3 | Cavin1 | Cp | Ehd4 | G6pd | Gstm3 | Me1 | Npc2 | Pls3 | Rpl30 | **Sgcd** | Tuba1c | |
| Aoc3 | Bag5 | Cavin2 | Csrp1 | Eif4a2 | Gfap | Gstp1 | Mrc1 | Ogn | Prnp | Rpl36 | Slc25a20 | Tuba8 | |
| Apoe | Bcam | Cd36 | Cst3 | Eno3 | Glud1 | Hadhb | Myh11 | Pacsin2 | Prph | Rps14 | Sncg | Twf2 | |
| Apoh | Blvrb | Ces1d | Dcn | Entpd2 | Gnai2 | Hspa1l | Myh4 | Pc | Psmc6 | Rps15 | Sord | Uchl1 | |
| Arl6ip5 | C3 | Cfb | Dctn2 | Ephx1 | Gng3 | Hspb1 | Myl12b | Pcmt1 | Pygm | Rps25 | Sri | Ugp2 | |

## U-shaped

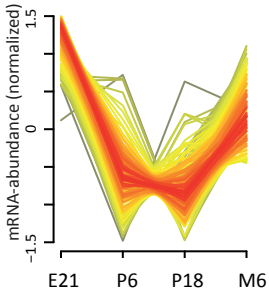


| | | | | | | | | | | |
|---|---|---|---|---|---|---|---|---|---|---|
| Acadl | Atp5f1b | Cycs | Gclm | Mat2a | Ppia | Rack1 | Rpl23 | Rpl9 | Rps8 | Tomm70 |
| Acot7 | Atp5mf | Dnm3 | Gnb1 | Mcts1 | Ppid | Ralb | Rpl23a | Rpn2 | Rpsa | Tpm3 |
| Actb | Avil | Dpysl4 | Gng12 | Ndufa12 | Ppp1cb | Rap1a | Rpl24 | Rps11 | S100a10 | Tuba4a |
| Actn1 | Cacybp | Dsp | Gpx1 | Ndufa3 | Ppp2r1b | Rap1b | Rpl27 | Rps15a | **Sept7** | Tubb3 |
| Actn4 | Calm1 | Dync1i2 | Hpcal1 | Ndufa4 | Ppp2r2a | **Rhoa** | Rpl27a | Rps20 | Skp1 | Ube2d1 |
| Adsl | Camk2d | Eef1a1 | Hsp90b1 | Ndufs1 | Prdx1 | Rhoc | Rpl28 | Rps23 | Slc25a24 | Uqcrc1 |
| Ahsa1 | Capza2 | Ehd1 | Hspa12b | Nxn | Prdx3 | Rpl10 | Rpl3 | Rps24 | Slc25a3 | Vapa |
| Akr1a1 | Cct4 | Emc1 | Hspa8 | Pacsin1 | Prps1 | Rpl11 | Rpl32 | Rps27a | Slc25a4 | Vdac3 |
| Anp32a | Cnn2 | Eno1 | Ina | Paics | Psma6 | Rpl14 | Rpl35 | Rps3 | Snx1 | Wdr1 |
| Anxa6 | Cnn3 | Erp29 | Kpna4 | Pcbp2 | Ptges3 | Rpl15 | Rpl4 | Rps3a | Snx2 | Ybx3 |
| Ap2b1 | Cox6a1 | Etf1 | Lasp1 | Pdia4 | Rab39a | Rpl17 | Rpl5 | Rps4x | Ssr4 | Ywhab |
| Arhgap1 | Cpne6 | Fbn1 | Ldha | Pgam1 | Rab6b | Rpl18 | Rpl6 | Rps5 | Stoml2 | Ywhag |
| Arpc1b | Cs | Fh | Lman2 | Pgk1 | Rab8a | Rpl21 | Rpl7 | Rps6 | Tagln2 | Ywhah |
| Arpc5 | **Ctnna1** | Fhl1 | Lxn | Phgdh | **Rac1** | Rpl22 | Rpl7a | Rps6ka3 | Thy1 | Zyx |

## Descending

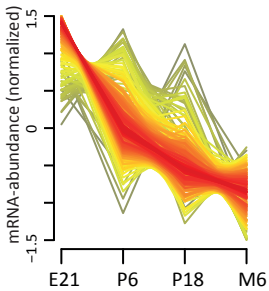


| | | | | | | | | | | | | | | |
|---|---|---|---|---|---|---|---|---|---|---|---|---|---|---|
| Abce1 | Apex1 | Calu | Col18a1 | Dnajb11 | Fermt2 | Hist1h1a | Ilk | Lrrc59 | Nid2 | Pdia3 | Psmb2 | Rps17 | Snd1 | Tomm40 | Ybx1 |
| Acly | Apoa1 | Cand1 | Copa | Dnm1l | Flna | Hist1h1b | Immt | Lum | Nipsnap1 | Pdia6 | Psmd13 | Rps18 | Snx6 | Tubb1 | Ykt6 |
| Actr1b | Arcn1 | Capn5 | Copb1 | Dpysl3 | Flnc | Hist1h1e | Ipo5 | **Mapk1** | Nipsnap3b | **Pfn1** | Psmd5 | Rps19 | Ssr1 | Tubb2b | Ywhae |
| Actr2 | Arf4 | Capza1 | Cope | Dpysl5 | Fn1 | Hist1h3a | Iqgap1 | Mapre1 | Nme1 | Phb2 | Psmd7 | Rrbp1 | Ssr3 | Tubb4b | Ywhaz |
| Add3 | Arf5 | **Car2** | Copg1 | Dync1li1 | Ganab | Hist1h3b | Islr | Marcks | Nme2 | Plcd1 | Ptpa | Sars | Stip1 | Tubb5 | Zc3hav1l |
| Agk | Arf6 | Cct2 | Coro1c | Eef1d | Gars | Hmgb1 | Isoc1 | **Mcam** | Nnt | Postn | Ran | Sec22b | Stx1b | Tubb6 | |
| Aifm1 | Aspn | Cct3 | Crmp1 | Eef1g | Glg1 | Hnrnpa2b1 | **Itgav** | Mthfd1 | Npm1 | Ppib | Rap2a | Sec23a | Stxbp6 | Tufm | |
| Ak2 | Atp2a2 | Cct5 | **Ctnnb1** | Eif2s1 | Glipr2 | Hnrnpa3 | **Itgb1** | Myadm | Nras | Ppic | Rap2b | Sec31a | Surf4 | Txndc5 | |
| Akap12 | Atp4a | Cct6a | Cttn | Eif3b | Glrx3 | Hnrnpd | Kif5a | Myh10 | Nsf | Ppp1ca | Rars | Sec61a1 | Syncrip | Uba1 | |
| Alad | Atp5f1a | Cct7 | Dad1 | Eif4a1 | Gnai3 | Hnrnpk | Kif5c | Nap1l1 | Ola1 | Ppp1cc | Rcn3 | Sec61b | Tcp1 | Ube2i | |
| Alcam | Basp1 | Cct8 | Ddost | Eif4h | Gnas | Hsp90aa1 | Kpnb1 | Nap1l4 | Otub1 | Prdx2 | **Rdx** | **Sept2** | Tgfbi | Ube2n | |
| Aldh7a1 | Bax | **Cfl1** | Ddx1 | Eif5a | Gnb2 | Hsp90ab1 | Kras | Ncam1 | P4hb | Prdx4 | Rpl10a | **Sept11** | Tln2 | Usp5 | |
| Anp32b | Bin1 | Ckap4 | **Dlg1** | **Epb41l3** | Gnb4 | Hspa5 | **Lama4** | Ncl | Pa2g4 | Prkaca | Rpl31 | Sept6 | Tm9sf3 | **Vcl** | |
| **Anxa2** | Bzw1 | Ckap5 | Dlst | Eprs | Gpd2 | Hspd1 | **Lamb1** | **Nedd4** | Pabpc1 | Psma1 | Rpl8 | Serpinh1 | Tmed2 | Vcp | |
| Ap2a2 | C1qbp | Cnrip1 | Dnaja1 | Fabp5 | Gpx7 | Idh2 | **Lamc1** | Nefh | Pafah1b2 | Psma5 | Rpn1 | Set | Tmed9 | Vdac1 | |
| Ap2s1 | Calr | Col14a1 | Dnaja2 | Fam129a | Hdlbp | Ikbip | Lpp | **Nid1** | Pcyox1 | Psma7 | Rps10 | Slk | Tmx1 | Yars | |

# B

| Cluster | #mRNA |
|---|---|
| **1** P6-up | 132 |
| **2** P18-up | 203 |
| **3** Late-up | 186 |
| **4** U-shaped | 154 |
| **5** Descending | 245 |
| **6** Unchanged | 126 |
| All | 1046 |

**Siems et al., Figure 4**

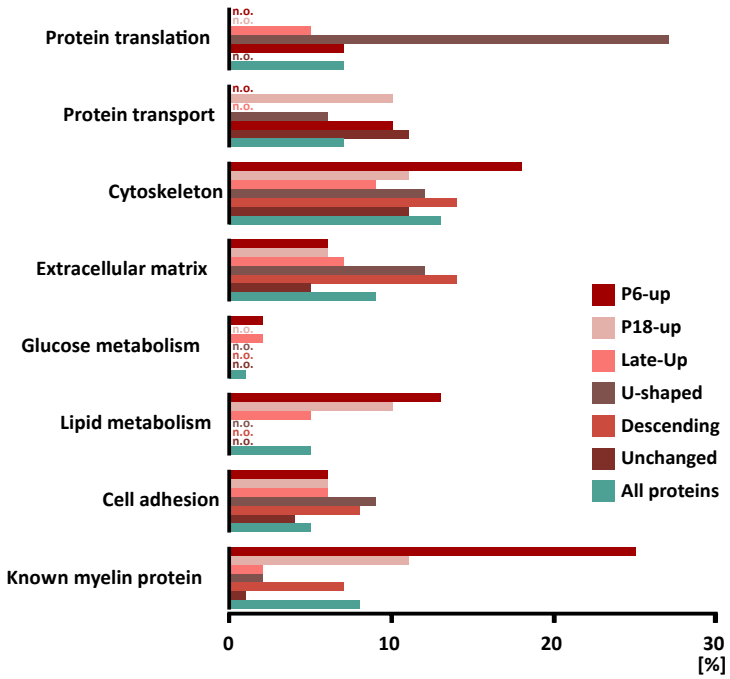

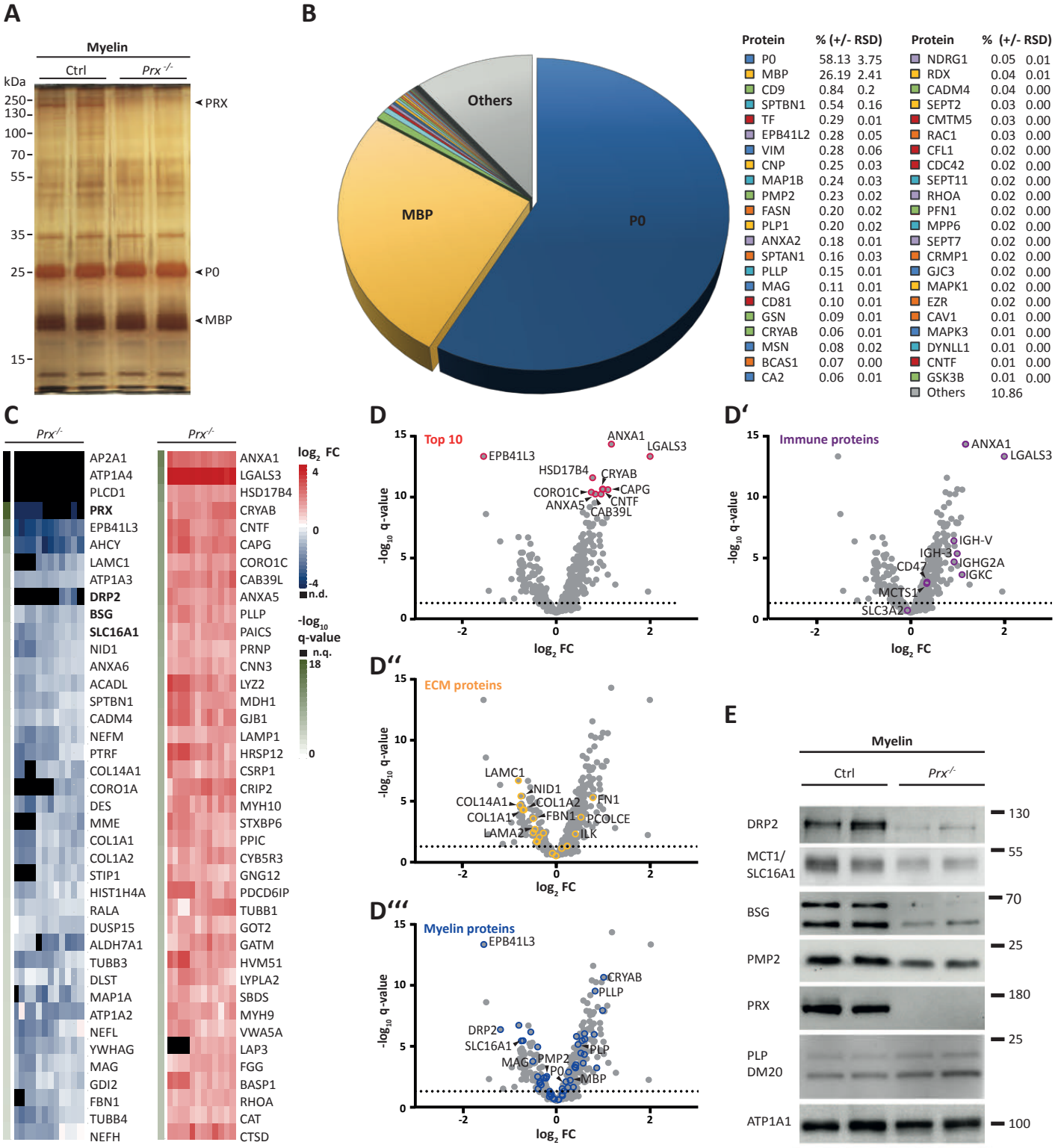


| Protein | % (+/- RSD) | | Protein | % (+/- RSD) | |
|---|---|---|---|---|---|
| P0 | 58.13 | 3.75 | NDRG1 | 0.05 | 0.01 |
| MBP | 26.19 | 2.41 | RDX | 0.04 | 0.01 |
| CD9 | 0.84 | 0.2 | CADM4 | 0.04 | 0.00 |
| SPTBN1 | 0.54 | 0.16 | SEPT2 | 0.03 | 0.00 |
| TF | 0.29 | 0.01 | CMTM5 | 0.03 | 0.00 |
| EPB41L2 | 0.28 | 0.05 | RAC1 | 0.03 | 0.00 |
| VIM | 0.28 | 0.06 | CFL1 | 0.02 | 0.00 |
| CNP | 0.25 | 0.03 | CDC42 | 0.02 | 0.00 |
| MAP1B | 0.24 | 0.03 | SEPT11 | 0.02 | 0.00 |
| PMP2 | 0.23 | 0.02 | RHOA | 0.02 | 0.00 |
| FASN | 0.20 | 0.02 | PFN1 | 0.02 | 0.00 |
| PLP1 | 0.20 | 0.02 | MPP6 | 0.02 | 0.00 |
| ANXA2 | 0.18 | 0.01 | SEPT7 | 0.02 | 0.00 |
| SPTAN1 | 0.16 | 0.03 | CRMP1 | 0.02 | 0.00 |
| PLLP | 0.15 | 0.01 | GJC3 | 0.02 | 0.00 |
| MAG | 0.11 | 0.01 | MAPK1 | 0.02 | 0.00 |
| CD81 | 0.10 | 0.01 | EZR | 0.02 | 0.00 |
| GSN | 0.09 | 0.01 | CAV1 | 0.01 | 0.00 |
| CRYAB | 0.06 | 0.01 | MAPK3 | 0.01 | 0.00 |
| MSN | 0.08 | 0.02 | DYNLL1 | 0.01 | 0.00 |
| BCAS1 | 0.07 | 0.00 | CNTF | 0.01 | 0.00 |
| CA2 | 0.06 | 0.01 | GSK3B | 0.01 | 0.00 |
| | | | Others | 10.86 | |

**A**

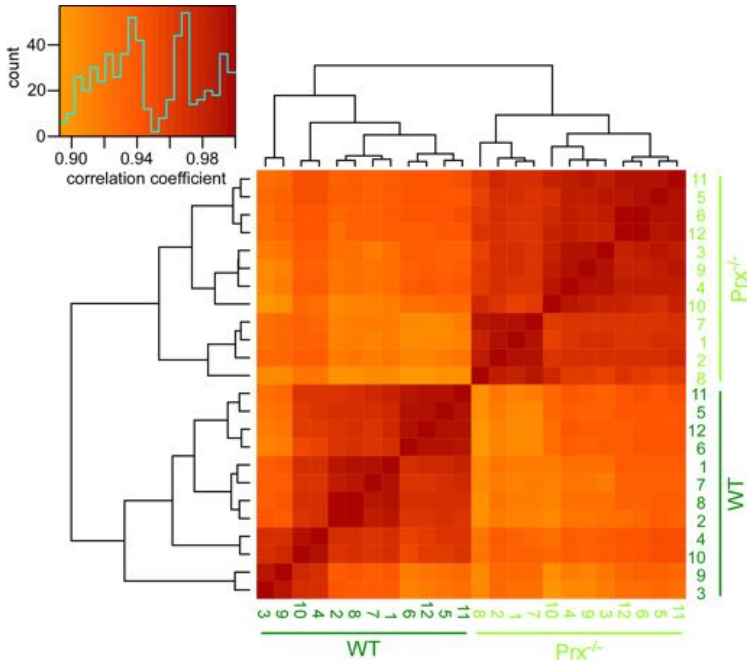
count
40
20
0
0.90
0.94
0.98
correlation coefficient
Prx-/-
WT
WT
Prx-/-

**B**

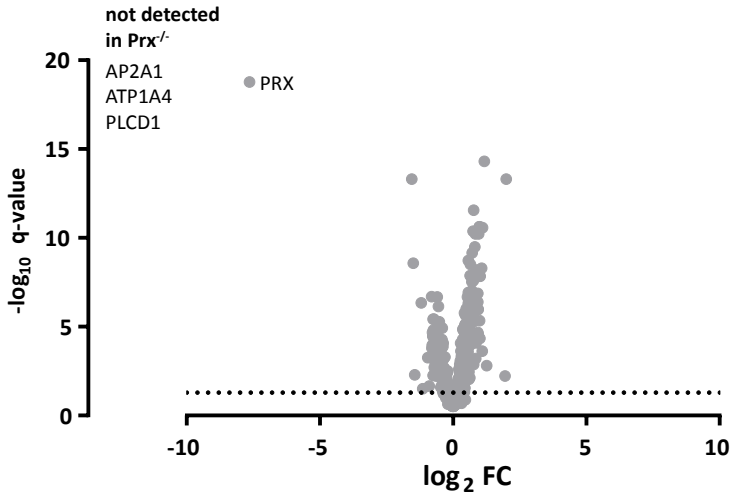
not detected
in Prx-/-
AP2A1
ATP1A4
PLCD1
PRX
-log10 q-value
20
15
10
5
0
-10
-5
0
5
10
log2 FC

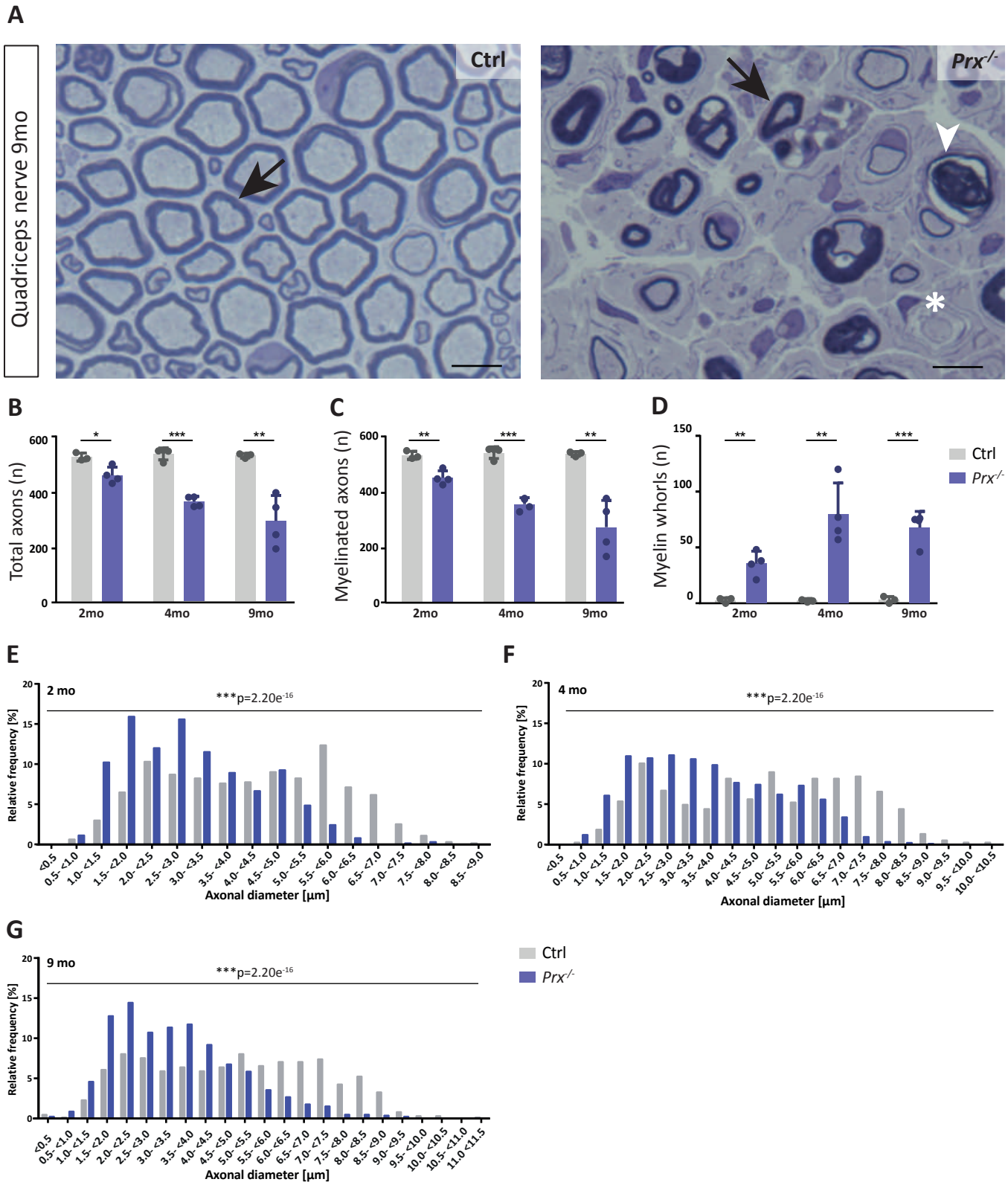
A
Quadriceps nerve 9mo
Ctrl
Prx-/-
B
Total axons (n)
C
Myelinated axons (n)
D
Myelin whorls (n)
Ctrl
Prx-/-
2mo
4mo
9mo
E
2 mo
***p=2.20e-16
Relative frequency [%]
Axonal diameter [µm]
F
4 mo
***p=2.20e-16
G
9 mo
***p=2.20e-16

***TOOLS AND RESOURCES***
*eLife-51406R2*

# Proteome profile of peripheral myelin in healthy mice and in a neuropathy model

Sophie B. Siems[1,7], Olaf Jahn[2,7], Maria A. Eichel[1], Nirmal Kannaiyan[3], Lai Man N. Wu[4], Diane L. Sherman[4], Kathrin Kusch[1], Dörte Hesse[2], Ramona B. Jung[1], Robert Fledrich[1,5], Michael W. Sereda[1,6], Moritz J. Rossner[3], Peter J. Brophy[4], Hauke B. Werner[1,*]

**Affiliations**
[1]Department of Neurogenetics, Max Planck Institute of Experimental Medicine, 37075 Göttingen, Germany
[2]Proteomics Group, Max Planck Institute of Experimental Medicine, 37075 Göttingen, Germany
[3]Department of Psychiatry and Psychotherapy, University Hospital, LMU Munich, 80336 Munich, Germany
[4]Centre for Discovery Brain Sciences, University of Edinburgh, Edinburgh, EH16 4SB, UK
[5]Institute of Anatomy, University of Leipzig, 04103 Leipzig, Germany
[6]Department of Clinical Neurophysiology, University Medical Center, 37075 Göttingen, Germany
[7]These authors contributed equally to this work

*** Corresponding author**
Dr. Hauke Werner
Max Planck Institute of Experimental Medicine
Department of Neurogenetics
Hermann-Rein-Str. 3
D-37075 Göttingen, Germany
Tel.: +49 (551) 3899-759; Fax.: +49 (551) 3899-758
E-mail: Hauke@em.mpg.de

**Key words**
Schwann cell, peripheral nervous system (PNS), myelin proteome, neuropathy, Charcot-Marie-Tooth disease (CMT4F), periaxin (PRX), MCT1/SLC16A1, demyelination, axon degeneration, transcriptome

**Word and figure count**
Abstract 149 words; Introduction/results/discussion 4786 words
6 main figures; 2 figure supplements; 2 main tables; 4 source data files

**ABSTRACT**

Proteome and transcriptome analyses aim at comprehending the molecular profiles of the brain, its cell-types and subcellular compartments including myelin. Despite the relevance of the peripheral nervous system for normal sensory and motor capabilities, analogous approaches to peripheral nerves and peripheral myelin have fallen behind evolving technical standards. Here we assess the peripheral myelin proteome by gel-free, label-free mass-spectrometry for deep quantitative coverage. Integration with RNA-Sequencing-based developmental mRNA-abundance profiles and neuropathy disease genes illustrates the utility of this resource. Notably, the periaxin-deficient mouse model of the neuropathy Charcot-Marie-Tooth 4F displays a highly pathological myelin proteome profile, exemplified by the discovery of reduced levels of the monocarboxylate transporter MCT1/SLC16A1 as a novel facet of the neuropathology. This work provides the most comprehensive proteome resource thus far to approach development, function and pathology of peripheral myelin, and a straightforward, accurate and sensitive workflow to address myelin diversity in health and disease.

## INTRODUCTION

The ensheathment of axons with myelin enables rapid impulse propagation, a prerequisite for normal motor and sensory capabilities of vertebrates (1,2). This is illustrated by demyelinating neuropathies of the Charcot-Marie-Tooth (CMT) spectrum, in which mutations affecting myelin genes as *MPZ, PMP22, GJB1* and *PRX* impair myelin integrity and reduce the velocity of nerve conduction in the peripheral nervous system (PNS) (3). Developmentally, myelination by Schwann cells in peripheral nerves is regulated by axonal neuregulin-1 (4,5) and the basal lamina (6–8) that is molecularly linked to the abaxonal Schwann cell membrane via integrins and the dystroglycan complex (9–12). In adulthood, the basal lamina continues to enclose all axon/myelin-units (13), probably to maintain myelin. Beyond regulation by extracellular cues, myelination involves multiple proteins mediating radial sorting of axons out of Remak bundles, myelin membrane growth and layer compaction (14–18). For example, the Ig-domain containing myelin protein zero (MPZ; also termed P0) mediates adhesion between adjacent extracellular membrane surfaces in compact myelin (19). At their intracellular surfaces, myelin membranes are compacted by the cytosolic domain of MPZ/P0 together with myelin basic protein (MBP; previously termed P1) (20,21). Not surprisingly, MPZ/P0 and MBP were early identified as the most abundant peripheral myelin proteins (22,23).

A system of cytoplasmic channels through the otherwise compacted myelin sheath remains non-compacted throughout life, i.e. the adaxonal myelin layer, paranodal loops, Schmidt-Lanterman incisures (SLI), and abaxonal longitudinal and transverse bands of cytoplasm termed bands of Cajal (14,24,25). Non-compacted myelin comprises cytoplasm, cytoskeletal elements, vesicles and lipid-modifying enzymes, and thus numerous proteins involved in maintaining the myelin sheath. The cytosolic channels probably also represent transport routes toward Schwann cell-dependent metabolic support of myelinated axons (26–31).

Considering that Schwann cells constitute a major proportion of the cells in the PNS, oligonucleotide microarray analyses have been used for mRNA abundance profiling of total sciatic nerves (32,33). Indeed, these systematic approaches allowed the identification of novel myelin constituents including non-compact myelin-associated protein (NCMAP/MP11) (34). Notwithstanding that the number of known peripheral myelin proteins has grown in recent years, a comprehensive molecular inventory has been difficult to achieve because applications of systematic ('omics') approaches specifically to Schwann cells and peripheral myelin remained comparatively scarce, different from studies addressing oligodendrocytes and CNS myelin (35–40). One main reason may be that the available techniques were not

sufficiently straightforward for general application. For example, the protein composition of peripheral myelin was previously assessed by proteome analysis (41). However, at that time the workflow of sample preparation and data acquisition (schematically depicted in **Figure 1A**) was very labor-intense and required a substantial amount of input material; yet the depth of the resulting datasets remained limited. In particular, differential myelin proteome analysis by 2-dimensional fluorescence intensity gel electrophoresis (2D-DIGE) requires considerable hands-on-time and technical expertise (41,42). While this method is powerful for the separation of proteoforms (43), it typically suffers from under-representation of highly basic and transmembrane proteins. It thus allows comparing the abundance of only few myelin proteins rather than quantitatively covering the entire myelin proteome. Because of these limitations and an only modest sample-to-sample reproducibility, 2D-DIGE analysis of myelin, although unbiased, has not been commonly applied beyond specialized laboratories.

The aim of the present study was to establish a straightforward and readily applicable workflow to facilitate both comprehensive knowledge about the protein composition of peripheral myelin and systematic assessment of differences between two states, e.g., pathological alterations in a neuropathy model. The major prerequisites were the biochemical purification of myelin, its solubilization with the detergent ASB-14 and the subsequent automated digestion with trypsin during filter-aided sample preparation (FASP). The tryptic peptides were fractionated by liquid chromatography and analyzed by mass spectrometry for gel-free, label-free quantitative proteome analysis. More specifically, we used nano-flow ultra-performance liquid chromatography (nanoUPLC) coupled to an electrospray-ionization quadrupole time-of-flight (ESI-QTOF) mass spectrometer with ion mobility option, providing an orthogonal dimension of peptide separation. The utilized data-independent acquisition (DIA) strategy relies on collecting data in an alternating low and elevated energy mode ($MS^E$); it enables simultaneous sequencing and quantification of all peptides entering the mass spectrometer without prior precursor selection (reviewed in (44,45)). With their high-duty cycle utilized for the acquisition of precursor ions, $MS^E$-type methods are ideally suited to reliably quantify proteins based on peptide intensities. Notably, these methods do not involve the use of spectral libraries in the identification of proteins, different from other DIA strategies. Instead, the achieved high-complexity fragmentation spectra are deconvoluted before submission to dedicated search engines for peptide and protein identification (46,47). In the $MS^E$ mode, this deconvolution involves precursor-fragment ion alignment solely on the basis of chromatographic elution profiles; on top, drift times of ion mobility-separated precursors are used in the high-definition (HD)$MS^E$ mode. An expansion of the latter referred to as the ultra-definition (UD)$MS^E$ mode, additionally implements drift time-dependent collision energy profiles for more effective precursor fragmentation (48,49).

Indeed, compared to the previously used manual handling and in-gel digestion, the current workflow (schematically depicted in **Figure 1A)** is considerably less labor-intense, and automated FASP increases sample-to-sample reproducibility. Moreover, differential analysis by quantitative mass spectrometry (MS) facilitates reproducible quantification of hundreds rather than a few distinct myelin proteins. Together, the present workflow increases the efficacy of assessing the peripheral myelin proteome while shifting the main workload from manual sample preparation and gel-separation to automated acquisition and processing of data. We propose that comprehending the expression profiles of all myelin proteins in the healthy PNS and in myelin-related disorders can contribute to advancing our understanding of the physiology and pathophysiology of peripheral nerves.

## RESULTS

### Purification of peripheral myelin

We biochemically enriched myelin as a light-weight membrane fraction from pools of sciatic nerves dissected from mice at postnatal day 21 (P21) using an established protocol of discontinuous sucrose density gradient centrifugation (41,50), in which myelin membranes accumulate at the interface between 0.29 and 0.85 M sucrose. By immunoblotting, proteins specific for both compact (MPZ/P0, MBP, PMP2) and non-compact (PRX) myelin were substantially enriched in the myelin fraction compared to nerve lysates (**Figure 1B**). Conversely, axonal (NEFH, KCNA1) and mitochondrial (VDAC) proteins and a marker for the Schwann cell nucleus (KROX20/EGR2) were strongly reduced in purified myelin. Together, these results imply that biochemically purified peripheral myelin is suitable for systematic analysis of its protein composition.

### Proteome analysis of peripheral myelin

It has long been difficult to accurately quantify the most abundant myelin proteins both in the CNS (PLP, MBP, CNP (51)) and the PNS (MPZ/P0, MBP, PRX; this work), probably owing to their exceptionally high relative abundance. For example, the major CNS myelin constituents PLP, MBP and CNP comprise 17, 8 and 4% of the total myelin protein, respectively (51). We have recently provided proof of principle (52) that the mass spectrometric quantification of these high-abundant myelin proteins is accurate and precise when data are acquired in the $MS^E$ data acquisition mode and proteins are quantified according to the TOP3 method, i.e. if their abundance values are obtained based on the proven correlation between the average intensity of the three peptides exhibiting the most intense mass spectrometry response and the absolute amount of their source protein (53,54). Using data acquisition by $MS^E$ we confirmed that CNP constitutes about 4% of the total CNS myelin proteome and that the abundance of CNP in myelin from mice heterozygous for the *Cnp* gene ($Cnp^{WT/null}$) compared to wild-type mice is 50.7% (±0.4%), in agreement with the halved gene dosage and gel-based quantification by silver staining or immunoblotting (52).

When applying the $MS^E$ mode to PNS myelin, we quantified 351 proteins with a false discovery rate (FDR) of <1% at peptide and protein level and an average sequence coverage of 35.5% (**Figure 1-source data 1**). While $MS^E$ (labeled in orange in **Figure 1C**) indeed provided a dynamic range of more than four orders of magnitude and thus quantitatively covered the exceptionally abundant myelin proteins MPZ/P0, MBP and PRX, the number of quantified proteins appeared limited when spectral complexity was deconvoluted solely on the basis of chromatographic elution profiles. Accordingly, by using the $UDMS^E$ mode, which

comprises ion mobility for additional peptide separation as well as drift time-specific collision energies for peptide fragmentation, proteome coverage was increased about three-fold (1078 proteins quantified; average sequence coverage 34.3%; **Figure 1-source data 1**). However, the dynamic range of UDMS$^E$ (labeled in blue in **Figure 1C**) was found to be somewhat compressed compared to that of MS$^E$, which can be considered an expectable feature of traveling wave ion mobility devices (55), where the analysis of pulsed ion packages leads to a temporal and spatial binning of peptides during ion mobility separation. Indeed, this manifests as a ceiling effect for the detection of exceptionally intense peptide signals, which results in an underestimation of the relative abundance of MPZ/P0, MBP and PRX by UDMS$^E$.

The complementary nature of the MS$^E$ and UDMS$^E$ data acquisition modes led us to conclude that a comprehensive analysis of the myelin proteome that facilitates both correct quantification of the most abundant proteins and deep quantitative coverage of the proteome would require analyzing the same set of samples with two different instrument settings for MS$^E$ and UDMS$^E$, respectively. Considering that instrument time is a bottleneck for the routine differential proteome analysis of myelin from mutant mice, we aimed to combine the strengths of MS$^E$ and UDMS$^E$ into a single data acquisition mode. Based on a gene ontology enrichment analysis for cellular components of the 200 proteins of highest and lowest abundance from the UDMS$^E$ dataset, we realized that the 'bottom' of the quantified proteome is probably largely unrelated to myelin but dominated by contaminants from other subcellular sources including mitochondria. We thus reasoned that for a myelin-directed data acquisition mode, proteome depth may be traded in for a gain in dynamic range and devised a novel method referred to as dynamic range enhancement (DRE)-UDMS$^E$, in which a deflection lens is used to cycle between full and reduced ion transmission during mass spectrometric scanning. Indeed, DRE-UDMS$^E$ quantified an intermediate number of proteins in PNS myelin (554 proteins; average sequence coverage 30.6%; **Figure 1-source data 1**) while providing an intermediate dynamic range (labeled in green in **Figure 1C**). We thus consider DRE-UDMS$^E$ as the data acquisition mode of choice most suitable for routine differential myelin proteome profiling (see below).

Overall, we found a high reproducibility between replicates and even among the different data acquisition modes as indicated by Pearson's correlation coefficients for protein abundance in the range of 0.765-0.997 (**Figure 1-supplement 1**). When comparing the proteins identified in PNS myelin using the three data acquisition modes, we found a very high overlap (**Figure 1D**). We also found a high overlap (**Figure 1E**) between the proteins identified in the present study by UDMS$^E$ and those detected in previous proteomic

approaches to PNS myelin (41,42), thus allowing a high level of confidence. Together, the three data acquisition modes exhibit distinct strengths in the efficient quantification of exceptionally abundant proteins ($MS^E$), establishing a comprehensive inventory ($UDMS^E$) and gel-free, label-free differential analysis of hundreds of distinct proteins ($DRE\text{-}UDMS^E$) in peripheral myelin (see **Figure 1A**). Yet, analyzing the same set of samples by different modes may not always be feasible in all routine applications when considering required instrument time.

**Relative abundance of peripheral myelin proteins**

Considering that $MS^E$ provides the high dynamic range required for the quantification of the most abundant myelin proteins, we calculated the relative abundance of the 351 proteins identified in myelin by $MS^E$ (**Figure 1-source data 1**). According to quantitative assessment of this dataset, the most abundant PNS myelin protein, myelin protein zero (MPZ/P0), constitutes 44% (+/-4% relative standard deviation (RSD)) of the total myelin protein (**Figure 2**). Myelin basic protein (MBP), periaxin (PRX) and tetraspanin-29 (CD9) constitute 18% (+/-1% RSD), 15% (+/-1%) and 1% (+/-0.2%) of the total myelin protein, respectively (**Figure 2**). For MPZ/P0 and MBP, our quantification by $MS^E$ is in agreement with but specifies prior estimations upon gel-separation and protein labeling by Sudan-Black, Fast-Green or Coomassie-Blue, in which they were judged to constitute 45–70% and 2–26% of the total myelin protein, respectively (22,56–58). However, gel-based estimates of the relative abundance of myelin proteins were not very precise with respect to many other proteins, including those of high molecular weight. Indeed, periaxin was identified as a constituent of peripheral myelin after the advent of gradient SDS-PAGE gels (59), which allowed improved migration of large proteins into gels. The present $MS^E$-based quantification of myelin proteins also extends beyond and partially adjusts an earlier mass spectrometric approach (41). Indeed, the current approach identified and quantified more myelin proteins, probably owing to improved protein solubilization during sample preparation and higher dynamic range of the used mass spectrometer. By $MS^E$, known myelin proteins (**Table 1**) collectively constitute over 85% of the total myelin protein (**Figure 2**) while proteins not yet associated with myelin account for the remaining 15% of the total myelin protein.

**Comprehensive compendium and comparison to the transcriptome**

To systematically elucidate the developmental abundance profiles of the transcripts that encode peripheral myelin proteins (**Figure 3**), we used our combined proteome inventory of peripheral myelin (**Figure 1-source data 1**) to filter mRNA abundance data of all genes expressed in sciatic nerves. By this strategy, **Figure 3** displays only those transcripts of which the protein product was identified in peripheral myelin rather than all transcripts in the

nerve, thereby discriminating myelin-related mRNAs from other mRNAs such as those present in peripheral axons, fibroblasts, immune cells etc. In this assessment we additionally included PMP22 although it was not detected by MS as well as 45 proteins exclusively identified by LC-MS of myelin separated by SDS-PAGE (**Figure 1-source data 1**). For mRNA abundance profiles, we exploited a recently established RNA sequencing analysis (RNA-Seq; platform Illumina HiSeq 2000) of sciatic nerves dissected form wild type Sprague Dawley rats at embryonic day 21 (E21), P6, P18 and 6 months (60). RNA-Seq provides reliable information about the relative abundance of all significantly expressed genes and is thus not limited to those represented on the previously used oligonucleotide microarrays (41). The raw data (accessible under GEO accession number GSE115930) were normalized (**Figure 3-source data 1**) and standardized. When comparing the proteome and transcriptome datasets, significant mRNA abundance was detected for all 1046 transcripts for which an unambiguous unique gene identifier was found (**Figure 3**). 126 transcripts displayed developmentally unchanged abundance levels, i.e., abundance changes below a threshold of 10% coefficient of variation (**Figure 3B; Figure 3-source data 1**).

By fuzzy c-means clustering, those 920 transcripts that showed developmental abundance changes were grouped into 5 clusters (**Figure 3A; Figure 3-source data 1**). Among those, one cluster corresponds to an mRNA-abundance peak coinciding with an early phase of myelin biogenesis (cluster ‘P6-UP‘), which includes the highest proportion of known myelin proteins (**Table 1**) such as MPZ/P0, MBP, PRX, cyclic nucleotide phosphodiesterase (CNP), fatty acid synthase (FASN), myelin-associated glycoprotein (MAG), proteolipid protein (PLP/DM20), cell adhesion molecule-4 (CADM4/NECL4), connexin-29 (GJC3), claudin-19 (CLDN19) and CKLF-like MARVEL-transmembrane domain containing protein-5 (CMTM5). However, many known myelin proteins clustered together according to their mRNA-abundance peak coinciding with a later phase of myelination (cluster ‘P18-UP‘), including peripheral myelin protein 2 (PMP2), tetraspanin-29 (CD9), tetraspanin-28 (CD81), connexin-32 (GJB1), plasmolipin (PLLP), junctional adhesion molecule-3 (JAM3), CD59 and dystrophin-related protein-2 (DRP2). The proportion of known myelin proteins was lower in the clusters corresponding to mRNA-abundance peaks in adulthood (clusters ‘late-UP‘, ‘U-shaped‘). Yet, a considerable number of transcripts displayed abundance peaks at the embryonic time-point (cluster ‘Descending‘), including carbonic anhydrase 2 (CA2), cofilin-1 CFL1), tubulin beta-4 (TUBB4b) and band 4.1-protein B (EPB41L3). Generalized, the clusters were roughly similar when comparing previous oligonucleotide microarray analysis of mouse sciatic nerves (41) and the RNA-Seq analysis of rat sciatic nerves (this study); yet, the latter provides information on a larger number of genes and with a higher level of

confidence. Together, clustering of mRNA abundance profiles allows categorizing peripheral myelin proteins into developmentally co-regulated groups.

When systematically assessing the proteins identified in myelin by gene ontology (GO)-term analysis, the functional categories over-represented in the entire myelin proteome included cell adhesion, cytoskeleton and extracellular matrix (labeled in turquoise in **Figure 4**). When analyzing the clusters of developmentally co-expressed transcripts (from **Figure 3**), proteins associated with the lipid metabolism were particularly enriched in the P6-UP and P18-UP clusters, while those associated with the extracellular matrix (ECM) were over-represented in the U-shaped and Descending clusters (**Figure 4**). For comparison, known myelin proteins (**Table 1**) were over-represented in the P6-UP and P18-UP clusters (**Figure 4**). Together, our proteome dataset provides comprehensive in-depth coverage of the protein constituents of peripheral myelin purified from the sciatic nerves of wild type mice, and comparison to the transcriptome allows identifying developmentally co-regulated and functional groups of myelin proteins. Our data thus supply a solid resource for the molecular characterization of myelin and for discovering functionally relevant myelin proteins.

**Neuropathy genes encoding myelin proteins**

Heritable neuropathies can be caused by mutations affecting genes preferentially expressed in neurons, Schwann cells or both (3,61–63). To systematically assess which neuropathy-causing genes encode peripheral myelin proteins, we compared our myelin proteome dataset with a current overview about disease genes at the NIH National Library of Medicine at https://ghr.nlm.nih.gov/condition/charcot-marie-tooth-disease#genes. Indeed, 31 myelin proteins were identified to be encoded by a proven neuropathy gene (**Table 2**), a considerable increase compared to eight disease genes found in a similar previous approach (41). Notably, this increase is owing to both the larger size of the current myelin proteome dataset (**Figure 1E**) and the recent discovery of numerous neuropathy genes by the widespread application of next generation sequencing.

**Pathological proteomic profile of peripheral myelin in a neuropathy model**

The results presented thus far were based on analyzing myelin of healthy wild type mice; yet we also sought to establish a straightforward method to systematically assess myelin diversity, as exemplified by alterations in a pathological situation. As a model we chose mice carrying a homozygous deletion of the periaxin gene (*Prx*$^{-/-}$) (26,64). Periaxin (PRX) is the third-most abundant peripheral myelin protein (**Figure 2**) and scaffolds the dystroglycan complex in Schwann cells. *Prx*$^{-/-}$ mice represent an established model of Charcot-Marie-Tooth disease type 4F (65–67). Aiming to assess the myelin proteome, we purified myelin

from pools of sciatic nerves dissected from *Prx*$^{-/-}$ and control mice at P21. Upon SDS-PAGE separation and silver staining the band patterns appeared roughly similar (**Figure 5A**), with the most obvious exception of the absence of the high-molecular weight band constituted by periaxin in *Prx*$^{-/-}$ myelin. Yet, several other bands also displayed genotype-dependent differences in intensity. As expected, PRX was also undetectable by MS$^{E}$ in *Prx*$^{-/-}$ myelin, in which most of the total myelin protein was constituted by MPZ/P0 and MBP (**Figure 5B; Figure 5-source data 1**).

Upon differential analysis by DRE-UDMS$^{E}$ (**Figure 5-source data 2**), multiple proteins displayed genotype-dependent differences as visualized in a heatmap displaying those 40 proteins of which the abundance was reduced or increased with the highest statistical significance in *Prx*$^{-/-}$ compared to control myelin (**Figure 5C**). For example, the abundance of the periaxin-associated dystrophin-related protein 2 (DRP2) was strongly reduced in *Prx*$^{-/-}$ myelin, as previously shown by immunoblotting (9). Notably, the abundance of multiple other proteins was also significantly reduced in *Prx*$^{-/-}$ myelin, including the extracellular matrix protein laminin C1 (LAMC1; previously termed LAMB2), the laminin-associated protein nidogen (NID1), Ig-like cell adhesion molecules (CADM4, MAG), the desmosomal junction protein desmin (DES), cytoskeletal and cytoskeleton-associated proteins (EPB41L3, MAP1A, CORO1A, SPTBN1, various microtubular and intermediate filament monomers), the monocarboxylate transporter MCT1 (also termed SLC16A1) and the MCT1-associated (68) immunoglobulin superfamily protein basigin (BSG, also termed CD147). On the other hand, proteins displaying the strongest abundance increase in *Prx*$^{-/-}$ myelin included immune-related proteins (LGALS3, LYZ2, CTSD), cytoskeletal and cytoskeleton-associated proteins (CAPG, CORO1C, CNN3, several myosin heavy chain subunits), peroxisomal enzymes (CAT, HSD17B4, MDH1) and known myelin proteins (PLLP/plasmolipin, CRYAB, GJB1/CX32). For comparison, the abundance of the marker proteolipid protein (PLP/DM20) (69) and the periaxin-associated integrin beta-4 (ITGB4) (12) in myelin was unaltered in *Prx*$^{-/-}$ myelin. Together, differential proteome analysis finds considerably more proteins and protein groups to be altered in *Prx*$^{-/-}$ myelin than previously known (**Figure 5C, D-D‘‘‘**), probably reflecting the complex pathology observed in this model (26,64).

The monocarboxylate transporter MCT1/SLC16A1 expressed by myelinating oligodendrocytes (70,71) and Schwann cells (28,72) has been proposed to supply lactate or other glucose breakdown products to axons, in which they may serve as substrate for the mitochondrial production of ATP (73–75). In this respect it was striking to find the abundance of MCT1 significantly reduced in peripheral myelin when PRX is lacking (**Figure 5C**), a result that we were able to confirm by immunoblotting (**Figure 5E**) and immunolabeling of teased

374 fiber preparations of sciatic nerves (**Figure 5F**). Notably, reduced expression of MCT1 in
375 *Slc16a1*$^{+/-}$ mice impairs axonal integrity at least in the CNS (70,76). The reduced abundance
376 of MCT1 thus represents an interesting novel facet of the complex pathology in *Prx*$^{-/-}$ mice.
377 Considering that the integrity of peripheral axons may be impaired in *Prx*$^{-/-}$ mice, we
378 assessed their quadriceps nerves. Indeed, *Prx*$^{-/-}$ mice displayed reduced axonal diameters, a
379 progressively reduced total number of axons and a considerable number of myelin whorls
380 lacking a visible axon (**Figure 6**), indicative of impaired axonal integrity (77). Yet we note that
381 molecular or neuropathological features other than the reduced abundance of MCT1
382 probably also contribute to the axonopathy in *Prx*$^{-/-}$ mice.
383
384 Together, gel-free, label free proteome analysis provides a cost- and time-efficient method
385 that provides an accurate, sensitive tool to gain systematic insight into the protein
386 composition of healthy peripheral myelin and its alterations in pathological situations. Indeed,
387 gel-free proteome analysis is particularly powerful and comprehensive compared to 2D-
388 DIGE; the workflow presented here appears readily applicable to other neuropathy models,
389 thereby promising discovery of relevant novel features of their neuropathology.
390
391

## DISCUSSION

We used gel-free, label-free quantitative mass spectrometry to assess the protein composition of myelin biochemically purified from the sciatic nerves of wild-type mice, thereby establishing a straightforward and readily applicable workflow to approach the peripheral myelin proteome. The key to comprehensiveness was to combine the strengths of three data acquisition modes, i.e., $MS^E$ for correct quantification of high-abundant proteins, $UDMS^E$ for deep quantitative proteome coverage including low-abundant proteins and DRE-$UDMS^E$ for differential analysis. We suggest that DRE-$UDMS^E$ provides a good compromise between dynamic range, identification rate and instrument run time for routine differential myelin proteome profiling as a prerequisite for a molecular understanding of myelin (patho)biology. We have also integrated the resulting compendium with RNA-Seq-based mRNA abundance profiles in peripheral nerves and neuropathy disease loci. Beyond providing the largest peripheral myelin proteome dataset thus far, the workflow is appropriate to serve as starting point for assessing relevant variations of myelin protein composition, e.g., in different nerves, ages, species and in pathological conditions. The identification of numerous pathological alterations of myelin protein composition in the *Prx*$^{-/-}$ neuropathy model indicates that the method is well suited to assess such diversity.

Aiming to understand nervous system function at the molecular level, multiple 'omics'-scale projects assess the spatio-temporal expression profiles of all mRNAs and proteins in the CNS including oligodendrocytes and myelin (35–39). Yet, peripheral nerves are also essential for normal sensory and motor capabilities. Prior approaches to the molecular profiles of Schwann cells and PNS myelin thus far, however, were performed >8 years ago (32–34,41,78–80), and the techniques have considerably advanced since. For example, current gel-free, label-free mass spectrometry can simultaneously identify and quantify the vast majority of proteins in a sample, thereby providing comprehensive in depth-information. Moreover, RNA-Seq technology has overcome limitations of the previously used microarrays for characterizing mRNA abundance profiles with respect to the number of represented genes and the suitability of the oligonucleotide probes. The present compendium thus provides high confidence with respect to the identification of myelin proteins, their relative abundance and their developmental mRNA expression profiles. This view is supported by the finding that over 80% of the total myelin proteome is constituted by approximately 50 previously known myelin proteins. We believe that the majority of the other identified proteins represent low-abundant myelin-associated constituents in line with the high efficiency of biochemical myelin purification. Doubtless, however, the myelin proteome also comprises

contaminants from other cellular sources, underscoring the need of independent validation for establishing newly identified constituents as true myelin proteins.

Do myelin proteins exist that escape identification by standard proteomic approaches? Indeed, some proteins display atypically distributed lysine and arginine residues, which represent the cleavage sites of the commonly used protease trypsin. The tryptic digest of these proteins leads to peptides that are not well suited for chromatographic separation and/or mass spectrometric detection/sequencing, as exemplified by the small hydrophobic tetraspan-transmembrane myelin proteins MAL (81) and PMP22 (82). We can thus not exclude that additional proteins with atypical tryptic digest patterns exist in peripheral myelin, which would need to be addressed by the use of alternative proteases. Moreover, potent signaling molecules including erbB receptor tyrosine kinases (83,84) and G-protein coupled receptors (GPRs) (85–87) display exceptionally low abundance. Such proteins may be identified when applying less stringent identification criteria, e.g., by requiring the sequencing of only one unique peptide per protein. However, lower stringency would also result in identifying false-positive proteins, which we wished to avoid for the purpose of the present compendium. We note that a truly comprehensive spatio-temporally resolved myelin proteome should preferentially also include systematic information about protein isoforms and post-translational modifications, which still poses technical challenges.

Mutations affecting the periaxin (*PRX*) gene in humans cause CMT type 4F (65,88–90); the neuropathology resulting from mutations affecting periaxin has been mainly investigated in the *Prx*$^{-/-}$ mouse model. Indeed, *Prx*$^{-/-}$ mice display a progressive peripheral neuropathy including axon/myelin-units with abnormal myelin thickness, demyelination, tomaculae, onion bulbs, reduced nerve conduction velocity (64), reduced abundance and mislocalization of the periaxin-associated DRP2 (9) and reduced internode length (26). Absence of SLIs (64) and bands of Cajal (26) imply that the non-compact myelin compartments are impaired when PRX is lacking. In the differential analysis of myelin purified from *Prx*$^{-/-}$ and control mice we find that the previously reported reduced abundance of DRP2 (9) represents one of the strongest molecular changes in the myelin proteome when PRX is lacking. Notably, the reported morphological changes in this neuropathy model (9,26,64) go along with alterations affecting the abundance of multiple other myelin-associated proteins, including junctional, cytoskeletal, extracellular matrix and immune-related proteins as well as lipid-modifying enzymes. Thus, the neuropathology in *Prx*$^{-/-}$ mice at the molecular level is more complex than previously anticipated. It is striking that the abundance of the monocarboxylate transporter MCT1/SLC16A1 that may contribute to the metabolic supply of lactate from myelinating cells to axons (27–31) is strongly reduced in *Prx*$^{-/-}$ myelin. Considering that

MCT1 in Schwann cells mainly localizes to Schmidt Lanterman incisures (SLI) (28) and that SLI are largely absent from myelin when PRX is lacking (64), the reduced abundance of MCT1 in *Prx*$^{-/-}$ myelin may be a consequence of the impaired myelin ultrastructure. Yet, considering that SLI are part of the cytosolic channels that may represent transport routes toward Schwann cell-dependent metabolic support of myelinated axons, the diminishment of MCT1 may contribute to reduced axonal diameters or axonal loss in *Prx*$^{-/-}$ mice, probably in conjunction with other molecular or morphological defects. Together, the in depth-analysis of proteins altered in neuropathy models can contribute to an improved understanding of nerve pathophysiology.

Compared to a previous approach (41), the number of proven neuropathy genes of which the encoded protein is mass spectrometrically identified in peripheral myelin has increased four-fold from eight to 32 in the present study. This reflects both that the number of proteins identified in myelin has approximately doubled and that more neuropathy genes are known due to the common use of genome sequencing. We note that our compendium comprises not only myelin-associated proteins causing (when mutated) demyelinating CMT1 (e.g., MPZ/P0, NEFL, PMP2) or intermediate CMT4 (GDAP1, NDRG1, PRX) but also axonal CMT2 (RAB7, GARS, HSPB1). Yet, the expression of genes causative of CMT2 is not necessarily limited to neurons, as exemplified by the classical myelin protein MPZ/P0. Indeed, a subset of *MPZ*-mutations causes axonal CMT2I or CMT2J (91–95), probably reflecting impaired axonal integrity as consequence of a mutation primarily affecting Schwann cells. We also note that the nuclear EGR2/KROX20 causative of demyelinating CMT1D has not been mass spectrometrically identified in myelin, reflecting that Schwann cell nuclei are efficiently removed during myelin purification.

While morphological analysis of peripheral nerves by light and electron microscopy is routine in numerous laboratories, systematic molecular analysis has been less straightforward. Using the sciatic nerve as a model, we show that systematic assessment of the myelin proteome and the total nerve transcriptome are suited to determine comprehensive molecular profiles in healthy nerves and in myelin-related disorders. Myelin proteome analysis can thus complement transcriptome analysis in assessing development, function and pathophysiology of peripheral nerves.

## MATERIALS AND METHODS

### Mouse models

*Prx*$^{-/-}$ mice (64) were kept on c57Bl/6 background in the animal facility of the University of Edinburgh (United Kingdom). Genotyping was by PCR on genomic DNA using the forward primers 5‘-CAGATTTGCT CTGCCCAAGT and 5‘-CGCCTTCTAT CGCCTTCTTGAC in combination with reverse primer 5‘-ATGCCCTCAC CCACTAACAG. The PCR yielded a 0.5 kb fragment for the wildtype allele and a 0.75 kb product for the mutant allele. The age of experimental animals is given in the figure legends. All animal work conformed to United Kingdom legislation (Scientific Procedures) Act 1986 and to the University of Edinburgh Ethical Review Committee policy; Home Office project license No. P0F4A25E9.

### Myelin purification

A light-weight membrane fraction enriched for myelin was purified from sciatic nerves of mice by sucrose density centrifugation and osmotic shocks as described (41,52). Myelin accumulates at the interface between 0.29 and 0.85 M sucrose. *Prx*$^{-/-}$ and wild type control C57Bl/6 mice were sacrificed by cervical dislocation at postnatal day 21 (P21). For each genotype, myelin was purified as three biological replicates (n=3); each biological replicate representing a pool of 20 sciatic nerves dissected from 10 mice. Protein concentration was determined using the DC Protein Assay Kit (Bio-Rad).

### Filter-aided sample preparation for proteome analysis

Protein fractions corresponding to 10 µg myelin protein were dissolved and processed according to a filter-aided sample preparation (FASP) protocol essentially as previously described for synaptic protein fractions (96) and as adapted to CNS myelin (52,97). Unless stated otherwise, all steps were automated on a liquid-handling workstation equipped with a vacuum manifold (Freedom EVO 150, Tecan) by using an adaptor device constructed in-house. Briefly, myelin protein samples were lysed and reduced in lysis buffer (7 M urea, 2 M thiourea, 10 mM DTT, 0.1 M Tris pH 8.5) containing 1% ASB-14 by shaking for 30 min at 37°C. Subsequently, the sample was diluted with ~10 volumes lysis buffer containing 2% CHAPS to reduce the ASB-14 concentration and loaded on centrifugal filter units (30 kDa MWCO, Merck Millipore). After removal of the detergents by washing twice with wash buffer (8 M urea, 10 mM DTT, 0.1 M Tris pH 8.5), proteins were alkylated with 50 mM iodoacetamide in 8 M urea, 0.1 M Tris pH 8.5 (20 min at RT), followed by two washes with wash buffer to remove excess reagent. Buffer was exchanged by washing three times with 50 mM ammonium bicarbonate (ABC) containing 10 % acetonitrile. After three additional washes with 50 mM ABC/10% acetonitrile, which were performed by centrifugation to ensure

quantitative removal of liquids potentially remaining underneath the ultrafiltration membrane, proteins were digested overnight at 37°C with 400 ng trypsin in 40 µl of the same buffer. Tryptic peptides were recovered by centrifugation followed by two additional extraction steps with 40 µl of 50 mM ABC and 40 µl of 1% trifluoroacetic acid (TFA), respectively. Aliquots of the combined flow-throughs were spiked with 10 fmol/µl of yeast enolase-1 tryptic digest standard (Waters Corporation) for quantification purposes and directly subjected to analysis by liquid chromatography coupled to electrospray mass spectrometry (LC-MS). A pool of all samples was injected at least before and after any sample set to monitor stability of instrument performance.

**Mass spectrometry**

Nanoscale reversed-phase UPLC separation of tryptic peptides was performed with a nanoAcquity UPLC system equipped with a Symmetry C18 5 µm, 180 µm × 20 mm trap column and a HSS T3 C18 1.8 µm, 75 µm × 250 mm analytical column (Waters Corporation) maintained at 45°C. Injected peptides were trapped for 4 min at a flow rate of 8 µl/min 0.1% TFA and then separated over 120 min at a flow rate of 300 nl/min with a gradient comprising two linear steps of 3-35% mobile phase B in 105 min and 35-60% mobile phase B in 15 min, respectively. Mobile phase A was water containing 0.1% formic acid while mobile phase B was acetonitrile containing 0.1% formic acid. Mass spectrometric analysis of tryptic peptides was performed using a Synapt G2-S quadrupole time-of-flight mass spectrometer equipped with ion mobility option (Waters Corporation). Positive ions in the mass range m/z 50 to 2000 were acquired with a typical resolution of at least 20.000 FWHM (full width at half maximum) and data were lock mass corrected post-acquisition. $UDMS^E$ and $DRE\text{-}UDMS^E$ analyses were performed in the ion mobility-enhanced data-independent acquisition mode with drift time-specific collision energies as described in detail by Distler et al. (48,49). Specifically, for $DRE\text{-}UDMS^E$ a deflection device (DRE lens) localized between the quadrupole and the ion mobility cell of the mass spectrometer was cycled between full (100% for 0.4 sec) and reduced (5% for 0.4 sec) ion transmission during one 0.8 sec full scan. Continuum LC-MS data were processed for signal detection, peak picking, and isotope and charge state deconvolution using Waters ProteinLynx Global Server (PLGS) version 3.0.2 (47). For protein identification, a custom database was compiled by adding the sequence information for yeast enolase 1 and porcine trypsin to the UniProtKB/Swiss-Prot mouse proteome and by appending the reversed sequence of each entry to enable the determination of false discovery rate (FDR). Precursor and fragment ion mass tolerances were automatically determined by PLGS 3.0.2 and were typically below 5 ppm for precursor ions and below 10 ppm (root mean square) for fragment ions. Carbamidomethylation of cysteine was specified as fixed and oxidation of methionine as variable modification. One missed trypsin cleavage

was allowed. Minimal ion matching requirements were two fragments per peptide, five fragments per protein, and one peptide per protein. The FDR for protein identification was set to 1% threshold.

**Analysis of proteomic data**

For each genotype (*Prx*$^{-/-}$ and wild type control mice sacrificed at P21), biochemical fractions enriched for PNS myelin were analyzed as three biological replicates (n=3 per condition); each biological replicate representing a pool of 20 sciatic nerves dissected from 10 mice. The samples were processed with replicate digestion and injection, resulting in four technical replicates per biological replicate and thus a total of 12 LC-MS runs per condition to be compared, essentially as previously reported for CNS myelin (36,97). The freely available software ISOQuant (www.isoquant.net) was used for post-identification analysis including retention time alignment, exact mass and retention time (EMRT) and ion mobility clustering, peak intensity normalization, isoform/homology filtering and calculation of absolute in-sample amounts for each detected protein (48,49,98) according to the TOP3 quantification approach (53,54). Only peptides with a minimum length of seven amino acids that were identified with scores above or equal to 5.5 in at least two runs were considered. FDR for both peptides and proteins was set to 1% threshold and only proteins reported by at least two peptides (one of which unique) were quantified using the TOP3 method. The parts per million (ppm) abundance values (i.e. the relative amount (w/w) of each protein in respect to the sum over all detected proteins) were log2-transformed and normalized by subtraction of the median derived from all data points for the given protein. Significant changes in protein abundance were detected by moderated t-statistics essentially as described (96,97) across all technical replicates using an empirical Bayes approach and false discovery (FDR)-based correction for multiple comparisons (100). For this purpose, the Bioconductor R packages "limma" (101) and "q-value" (102) were used in RStudio, an integrated development environment for the open source programming language R. Proteins identified as contaminants (e.g. components of blood or hair cells) were removed from the analysis. Proteins with ppm values below 100 which were not identified in one genotype were considered as just above detection level and also removed from the analysis. The relative abundance of a protein in myelin was accepted as altered if both statistically significant (q-value <0.05). Pie charts, heatmaps and volcano plots were prepared in Microsoft Excel 2013 and GraphPad Prism 7. Pearson's correlation coefficients derived from log2-transformed ppm abundance values were clustered and visualized with the tool heatmap.2 contained in the R package gplots (CRAN.R-project.org/package=gplots). Only pairwise complete observations were considered to reduce the influence of missing values on clustering behavior. The mass spectrometry proteomics data have been deposited to the ProteomeXchange Consortium

(proteomecentral.proteomexchange.org) via the PRIDE partner repository (103) with the dataset identifier PXD015960.

**Gel electrophoresis and silver staining of gels**

Protein concentration was determined using the DC Protein Assay kit (BioRad). Samples were separated on a 12% SDS-PAGE for 1 h at 200 V using the BioRad system, fixated overnight in 10% [v/v] acetic acid and 40 % [v/v] ethanol and then washed in 30% ethanol (2x 20 min) and dd$H_2O$ (1x 20 min). For sensitization, gels were incubated 1 min in 0.012% [v/v] $Na_2S_2O_3$ and subsequently washed with dd$H_2O$ (3x 20 sec). For silver staining, gels were impregnated for 20 min in 0.2 % [w/v] $AgNO_3$ / 0.04% formaldehyde, washed with dd$H_2O$ (3x 20 sec) and developed in 3% [w/v] $Na_2CO_3$ / 0.02% [w/v] formaldehyde. The reaction was stopped by exchanging the solution with 5% [v/v] acetic acid.

**Immunoblotting**

Immunoblotting was performed as described (104,105). Primary antibodies were specific for dystrophin-related-protein 2 (DRP2; Sigma; 1:1000), peripheral myelin protein 2 (PMP2; ProteinTech Group 12717-1-AP; 1:1000), proteolipid protein (PLP/DM20; A431 (106); 1:5000), Monocarboxylate transporter 1 (MCT1/SLC16A1; (107); 1:1000), periaxin (PRX; (59); 1:1000), sodium/potassium-transporting ATPase subunit alpha-1 (ATP1A1; 1:2000; Abcam #13736-1-AP), myelin protein zero (MPZ/P0; (108); kind gift by J. Archelos-Garcia; 1:10.000), voltage-dependent anion-selective channel protein (VDAC; Abcam #ab15895; 1:1000), basigin (BSG/CD147; ProteinTech Group #ab64616; 1:1000), neurofilament H (NEFH/NF-H; Covance #SMI-32P; 1:1000), voltage-gated potassium channel subunit A member 1 (KCNA1; Neuromab #73-007; 1:1000), EGR2/KROX20 ((109); kind gift by D. Meijer, Edinburgh; 1:1000) and myelin basic protein (MBP; 1:2000). To generate the latter antisera, rabbits were immunized (Pineda Antikörper Service, Berlin, Germany) with the KLH-coupled peptide CQDENPVVHFFK corresponding to amino acids 212-222 of mouse MBP isoform 1 (Swisprot/Uniprot-identifier P04370-1). Anti-MBP antisera were purified by affinity chromatography and extensively tested for specificity by immunoblot analysis of homogenate of brains dissected from wild-type mice compared to *Mbp*$^{shiverer/shiverer}$ mice that lack expression of MBP. Appropriate secondary anti-mouse or -rabbit antibodies conjugated to HRP were from dianova. Immunoblots were developed using the Enhanced Chemiluminescence Detection kit (Western Lightning® Plus, Perkin Elmer) and detected with the Intas ChemoCam system (INTAS Science Imaging Instruments GmbH, Göttingen, Germany).

**Immunolabelling of teased fibers**

Teased fibers were prepared as previously described (9,110). For each genotype, one male mouse was sacrificed by cervical dislocation at P17. Immunolabelling of teased fibers was performed as described (69). Briefly, teased fibers were fixed for 5 min in 4% paraformaldehyde, permeabilized 5 min with ice-cold methanol, washed in PBS (3x 5 min) and blocked for 1 h at 21°C in blocking buffer (10% horse serum, 0.25% Triton X-100, 1% bovine serum albumin in PBS). Primary antibodies were applied overnight at 4°C in incubation buffer (1.5% horse serum, 0.25% Triton X-100 in PBS). Samples were washed in PBS (3x 5 min) and secondary antibodies were applied in incubation buffer (1 h, RT). Samples were again washed in PBS (2x 5 min), and 4‘,6-diamidino-2-phenylindole (DAPI; 1:50 000 in PBS) was applied for 10 min at RT. Samples were briefly washed 2x with $ddH_2O$ and mounted using Aqua-Poly/Mount (Polysciences, Eppelheim, Germany). Antibodies were specific for myelin-associated glycoprotein (MAG clone 513; Chemicon MAB1567; 1:50) and MCT1/SLC16A1 (107). Secondary antibodies were donkey α-rabbit-Alexa488 (Invitrogen A21206; 1:1000) and donkey α-mouse-Alexa555 (Invitrogen A21202; 1:1000). Labeled teased fibers were imaged using the confocal microscope Leica SP5. The signal was collected with the objective HCX PL APO lambda blue 63.0.x1.20. DAPI staining was excited with 405 nm and collected between 417 nm - 480 nm. To excite the Alexa488 fluorophore an Argon laser with the excitation of 488 nm was used and the emission was set to 500 nm - 560 nm. Alexa555 was excited by using the DPSS561 laser at an excitation of 561 nm and the emission was set to 573 nm - 630 nm. To export and process the images LAS AF lite and Adobe Photoshop were used.

**mRNA abundance profiles**

Raw data were previously established (60) from the sciatic nerves of wild type Sprague Dawley rats at the indicated ages (E21, P6, P18; n=4 per time point). Briefly, sciatic nerves were dissected, the epineurium was removed, total RNA was extracted with the RNeasy Kit (Qiagen), concentration and quality (ratio of absorption at 260/280 nm) of RNA samples were determined using the NanoDrop spectrophotometer (ThermoScientific), integrity of the extracted RNA was determined with the Agilent 2100 Bioanalyser (Agilent Technologies) and RNA-Seq was performed using the Illumina HiSeq2000 platform. RNA-Seq raw data are available under the GEO accession number GSE115930 (60). For the present analysis, the fastqfiles were mapped to *rattus norvegicus* rn6 using Tophat Aligner and then quantified based on the Ensemble Transcripts release v96. The raw read counts were then normalized using the R package DESeq2. The normalized gene expression data was then standardized to a mean of zero and a standard deviation of one, therefore genes with similar changes in expression are close in the euclidian space. Clustering was performed on the standardized

682 data using the R package mfuzz. Transcripts displaying abundance differences of less than
683 10% coefficient of variation were considered developmentally unchanged.
684
685 **Venn diagrams**
686 Area-proportional Venn diagrams were prepared using BioVenn (111) at www.biovenn.nl/.
687
688 **GO-term**
689 For functional categorization of the myelin proteome the associated gene ontology terms
690 were systematically analyzed on the mRNA abundance cluster using the Database for
691 Annotation, Visualization and Integrated Discovery (DAVID; https://david.ncifcrf.gov). For
692 comparison known myelin proteins according to literature were added.
693
694 **Histological analysis**
695 *Prx*$^{-/-}$ and control mice were perfused at the indicated ages intravascularly with fixative
696 solution (2.5% glutaraldehyde, 4% paraformaldehyde, 0.1 M sodium cacodylate buffer, pH
697 7.4). Quadriceps nerves were removed, fixed for 2 h at room temperature, followed by 18 h
698 at 4°C in the same fixative, postfixed in $OsO_4$, dehydrated a graded series of ethanol,
699 followed by propylene oxide and embedded in Araldite. All axons not associated with a
700 Remak bundle were counted and categorized as myelinated or non-myelinated. All myelin
701 profiles lacking a recognizable axon were counted. The total number of axons were counted
702 on micrographs of toluidine blue stained Araldite sections (0.5 µm) of quadriceps nerves.
703 Precise p-values for the quantitative comparison between Ctrl and *Prx*$^{-/-}$ mice were: Total
704 number of axons (**Figure 6B**; Student's unpaired t-test): 2 mo p=0.01734; 4 mo p=2.1E-05; 9
705 mo p=0.007625; Number of myelinated axons (**Figure 6C**; Student's unpaired t-test): 2 mo
706 p=0.00444; 4 mo p=2.12E-05; 9 mo p=0.005766; Number of empty myelin profiles (**Figure**
707 **6D**; Student's unpaired t-test): 2 mo p=0.004445; 4 mo p=0.001461; 9 mo p=0.000695;
708 Axonal diameters (**Figure 6E-G**; two-sided Kolmogorow-Smirnow test): 2 mo p=2.20E-16; 4
709 mo p=2.20E-16; 9 mo p=2.20E-16.
710
711

**ACKNOWLEDGMENTS**

We thank J. Archelos-Garcia and D. Meijer for antibodies, T. Buscham and J. Edgar for discussions, L. Piepkorn for support in data analysis, K.-A. Nave for support made possible by a European Research Council Advanced Grant (‘MyeliNano‘ to K.-A.N.) and the International Max Planck Research School for Genome Science (IMPRS-GS) for supporting S.B.S..

**FUNDING**

Our work is supported by the Deutsche Forschungsgemeinschaft (DFG; Grants WE 2720/2-2, WE 2720/4-1 and WE 2720/5-1 to H.B.W. and RO 4076/3-2 to M.J.R.) and the Wellcome Trust (Grant No 0842424 to P.J.B.).

**CONFLICT OF INTEREST STATEMENT**

The authors declare no conflict of interest.

## REFERENCES


1. Weil M-T, Heibeck S, Töpperwien M, tom Dieck S, Ruhwedel T, Salditt T, et al. Axonal Ensheathment in the Nervous System of Lamprey: Implications for the Evolution of Myelinating Glia. J Neurosci [Internet]. 2018 Jul 18;38(29):6586–96. Available from: http://www.jneurosci.org/lookup/doi/10.1523/JNEUROSCI.1034-18.2018
2. Hartline DK, Colman DR. Rapid Conduction and the Evolution of Giant Axons and Myelinated Fibers. Curr Biol [Internet]. 2007 Jan;17(1):R29–35. Available from: https://linkinghub.elsevier.com/retrieve/pii/S0960982206025231
3. Rossor AM, Polke JM, Houlden H, Reilly MM. Clinical implications of genetic advances in Charcot–Marie–Tooth disease. Nat Rev Neurol [Internet]. 2013 Oct 10;9(10):562–71. Available from: http://www.nature.com/articles/nrneurol.2013.179
4. Michailov G V. Axonal Neuregulin-1 Regulates Myelin Sheath Thickness. Science (80- ) [Internet]. 2004 Apr 30;304(5671):700–3. Available from: http://www.sciencemag.org/cgi/doi/10.1126/science.1095862
5. Taveggia C, Zanazzi G, Petrylak A, Yano H, Rosenbluth J, Einheber S, et al. Neuregulin-1 Type III Determines the Ensheathment Fate of Axons. Neuron [Internet]. 2005 Sep;47(5):681–94. Available from: https://linkinghub.elsevier.com/retrieve/pii/S0896627305006926
6. Chernousov MA, Yu W-M, Chen Z-L, Carey DJ, Strickland S. Regulation of Schwann cell function by the extracellular matrix. Glia [Internet]. 2008 Nov 1;56(14):1498–507. Available from: http://doi.wiley.com/10.1002/glia.20740
7. Petersen SC, Luo R, Liebscher I, Giera S, Jeong S-J, Mogha A, et al. The Adhesion GPCR GPR126 Has Distinct, Domain-Dependent Functions in Schwann Cell Development Mediated by Interaction with Laminin-211. Neuron [Internet]. 2015 Feb;85(4):755–69. Available from: https://linkinghub.elsevier.com/retrieve/pii/S0896627314011660
8. Ghidinelli M, Poitelon Y, Shin YK, Ameroso D, Williamson C, Ferri C, et al. Laminin 211 inhibits protein kinase A in Schwann cells to modulate neuregulin 1 type III-driven myelination. Emery B, editor. PLOS Biol [Internet]. 2017 Jun 21;15(6):e2001408. Available from: https://dx.plos.org/10.1371/journal.pbio.2001408
9. Sherman DL, Fabrizi C, Gillespie CS, Brophy PJ. Specific Disruption of a Schwann Cell Dystrophin-Related Protein Complex in a Demyelinating Neuropathy. Neuron [Internet]. 2001 May;30(3):677–87. Available from: https://linkinghub.elsevier.com/retrieve/pii/S0896627301003270
10. Masaki T, Matsumura K, Hirata A, Yamada H, Hase A, Arai K, et al. Expression of Dystroglycan and the Laminin-α2 Chain in the Rat Peripheral Nerve during Development. Exp Neurol [Internet]. 2002 Mar;174(1):109–17. Available from: https://linkinghub.elsevier.com/retrieve/pii/S0014488601978562
11. Nodari A, Previtali SC, Dati G, Occhi S, Court FA, Colombelli C, et al. 6 4 Integrin and Dystroglycan Cooperate to Stabilize the Myelin Sheath. J Neurosci [Internet]. 2008 Jun 25;28(26):6714–9. Available from: http://www.jneurosci.org/cgi/doi/10.1523/JNEUROSCI.0326-08.2008

12. Raasakka A, Linxweiler H, Brophy PJ, Sherman DL, Kursula P. Direct Binding of the Flexible C-Terminal Segment of Periaxin to β4 Integrin Suggests a Molecular Basis for CMT4F. Front Mol Neurosci [Internet]. 2019 Apr 9;12. Available from: https://www.frontiersin.org/article/10.3389/fnmol.2019.00084/full
13. Hess A, Lansing AI. The fine structure of peripheral nerve fibers. Anat Rec. 1953;
14. Sherman DL, Brophy PJ. Mechanisms of axon ensheathment and myelin growth. Nat Rev Neurosci [Internet]. 2005 Sep;6(9):683–90. Available from: http://www.nature.com/articles/nrn1743
15. Pereira JA, Lebrun-Julien F, Suter U. Molecular mechanisms regulating myelination in the peripheral nervous system. Trends Neurosci [Internet]. 2012 Feb;35(2):123–34. Available from: https://linkinghub.elsevier.com/retrieve/pii/S0166223611001937
16. Grove M, Brophy PJ. FAK Is Required for Schwann Cell Spreading on Immature Basal Lamina to Coordinate the Radial Sorting of Peripheral Axons with Myelination. J Neurosci [Internet]. 2014 Oct 1;34(40):13422–34. Available from: http://www.jneurosci.org/cgi/doi/10.1523/JNEUROSCI.1764-14.2014
17. Monk KR, Feltri ML, Taveggia C. New insights on schwann cell development. Glia [Internet]. 2015 Aug;63(8):1376–93. Available from: http://doi.wiley.com/10.1002/glia.22852
18. Feltri ML, Poitelon Y, Previtali SC. How Schwann Cells Sort Axons. Neurosci [Internet]. 2016 Jun 16;22(3):252–65. Available from: http://journals.sagepub.com/doi/10.1177/1073858415572361
19. Giese KP, Martini R, Lemke G, Soriano P, Schachner M. Mouse P0 gene disruption leads to hypomyelination, abnormal expression of recognition molecules, and degeneration of myelin and axons. Cell [Internet]. 1992 Nov;71(4):565–76. Available from: https://linkinghub.elsevier.com/retrieve/pii/009286749290591Y
20. Martini R, Mohajeri MH, Kasper S, Giese KP, Schachner M. Mice doubly deficient in the genes for P0 and myelin basic protein show that both proteins contribute to the formation of the major dense line in peripheral nerve myelin. J Neurosci. 1995;
21. Nawaz S, Schweitzer J, Jahn O, Werner HB. Molecular evolution of myelin basic protein, an abundant structural myelin component. Glia [Internet]. 2013 Aug;61(8):1364–77. Available from: http://doi.wiley.com/10.1002/glia.22520
22. Greenfield S, Brostoff S, Eylar EH, Morell P. PROTEIN COMPOSITION OF MYELIN OF THE PERIPHERAL NERVOUS SYSTEM. J Neurochem [Internet]. 1973 Apr;20(4):1207–16. Available from: http://doi.wiley.com/10.1111/j.1471-4159.1973.tb00089.x
23. Brostoff SW, Karkhanis YD, Carlo DJ, Reuter W, Eylar EH. Isolation and partial characterization of the major proteins of rabbit sciatic nerve myelin. Brain Res [Internet]. 1975 Mar;86(3):449–58. Available from: https://linkinghub.elsevier.com/retrieve/pii/0006899375908951
24. Nave K-A, Werner HB. Myelination of the Nervous System: Mechanisms and Functions. Annu Rev Cell Dev Biol [Internet]. 2014 Oct 11;30(1):503–33. Available from: http://www.annualreviews.org/doi/10.1146/annurev-cellbio-100913-013101
25. Kleopa KA, Sargiannidou I. Connexins, gap junctions and peripheral neuropathy. Neurosci Lett

[Internet]. 2015 Jun;596:27–32. Available from: https://linkinghub.elsevier.com/retrieve/pii/S0304394014008453

26. Court FA, Sherman DL, Pratt T, Garry EM, Ribchester RR, Cottrell DF, et al. Restricted growth of Schwann cells lacking Cajal bands slows conduction in myelinated nerves. Nature [Internet]. 2004 Sep;431(7005):191–5. Available from: http://www.nature.com/articles/nature02841

27. Beirowski B, Babetto E, Golden JP, Chen Y-J, Yang K, Gross RW, et al. Metabolic regulator LKB1 is crucial for Schwann cell–mediated axon maintenance. Nat Neurosci [Internet]. 2014 Oct 7;17(10):1351–61. Available from: http://www.nature.com/articles/nn.3809

28. Domenech-Estevez E, Baloui H, Repond C, Rosafio K, Medard J-J, Tricaud N, et al. Distribution of Monocarboxylate Transporters in the Peripheral Nervous System Suggests Putative Roles in Lactate Shuttling and Myelination. J Neurosci [Internet]. 2015 Mar 11;35(10):4151–6. Available from: http://www.jneurosci.org/cgi/doi/10.1523/JNEUROSCI.3534-14.2015

29. Kim S, Maynard JC, Sasaki Y, Strickland A, Sherman DL, Brophy PJ, et al. Schwann Cell O-GlcNAc Glycosylation Is Required for Myelin Maintenance and Axon Integrity. J Neurosci [Internet]. 2016 Sep 14;36(37):9633–46. Available from: http://www.jneurosci.org/cgi/doi/10.1523/JNEUROSCI.1235-16.2016

30. Gonçalves NP, Vægter CB, Andersen H, Østergaard L, Calcutt NA, Jensen TS. Schwann cell interactions with axons and microvessels in diabetic neuropathy. Nat Rev Neurol [Internet]. 2017 Mar 30;13(3):135–47. Available from: http://www.nature.com/articles/nrneurol.2016.201

31. Stassart RM, Möbius W, Nave K-A, Edgar JM. The Axon-Myelin Unit in Development and Degenerative Disease. Front Neurosci [Internet]. 2018 Jul 11;12. Available from: https://www.frontiersin.org/article/10.3389/fnins.2018.00467/full

32. Nagarajan R, Le N, Mahoney H, Araki T, Milbrandt J. Deciphering peripheral nerve myelination by using Schwann cell expression profiling. Proc Natl Acad Sci [Internet]. 2002 Jun 25;99(13):8998–9003. Available from: http://www.pnas.org/cgi/doi/10.1073/pnas.132080999

33. Le N, Nagarajan R, Wang JYT, Araki T, Schmidt RE, Milbrandt J. Analysis of congenital hypomyelinating Egr2Lo/Lo nerves identifies Sox2 as an inhibitor of Schwann cell differentiation and myelination. Proc Natl Acad Sci [Internet]. 2005 Feb 15;102(7):2596–601. Available from: http://www.pnas.org/cgi/doi/10.1073/pnas.0407836102

34. Ryu EJ, Yang M, Gustin JA, Chang L-W, Freimuth RR, Nagarajan R, et al. Analysis of Peripheral Nerve Expression Profiles Identifies a Novel Myelin Glycoprotein, MP11. J Neurosci [Internet]. 2008 Jul 23;28(30):7563–73. Available from: http://www.jneurosci.org/cgi/doi/10.1523/JNEUROSCI.1659-08.2008

35. Zhang Y, Chen K, Sloan SA, Bennett ML, Scholze AR, O'Keeffe S, et al. An RNA-Sequencing Transcriptome and Splicing Database of Glia, Neurons, and Vascular Cells of the Cerebral Cortex. J Neurosci [Internet]. 2014 Sep 3;34(36):11929–47. Available from: http://www.jneurosci.org/cgi/doi/10.1523/JNEUROSCI.1860-14.2014

36. Patzig J, Erwig MS, Tenzer S, Kusch K, Dibaj P, Möbius W, et al. Septin/anillin filaments scaffold central nervous system myelin to accelerate nerve conduction. Elife. 2016;5:e17119.

37. Sharma K, Schmitt S, Bergner CG, Tyanova S, Kannaiyan N, Manrique-Hoyos N, et al. Cell

type– and brain region–resolved mouse brain proteome. Nat Neurosci [Internet]. 2015 Dec 2;18(12):1819–31. Available from: http://www.nature.com/articles/nn.4160

38. Thakurela S, Garding A, Jung RB, Müller C, Goebbels S, White R, et al. The transcriptome of mouse central nervous system myelin. Sci Rep [Internet]. 2016 May 13;6(1):25828. Available from: http://www.nature.com/articles/srep25828

39. Marques S, Zeisel A, Codeluppi S, van Bruggen D, Mendanha Falcao A, Xiao L, et al. Oligodendrocyte heterogeneity in the mouse juvenile and adult central nervous system. Science (80- ) [Internet]. 2016 Jun 10;352(6291):1326–9. Available from: http://www.sciencemag.org/cgi/doi/10.1126/science.aaf6463

40. De Monasterio-Schrader P, Jahn O, Tenzer S, Wichert SP, Patzig J, Werner HB. Systematic approaches to central nervous system myelin. Cellular and Molecular Life Sciences. 2012.

41. Patzig J, Jahn O, Tenzer S, Wichert SP, de Monasterio-Schrader P, Rosfa S, et al. Quantitative and Integrative Proteome Analysis of Peripheral Nerve Myelin Identifies Novel Myelin Proteins and Candidate Neuropathy Loci. J Neurosci [Internet]. 2011 Nov 9;31(45):16369–86. Available from: http://www.jneurosci.org/cgi/doi/10.1523/JNEUROSCI.4016-11.2011

42. Kangas SM, Ohlmeier S, Sormunen R, Jouhilahti E-M, Peltonen S, Peltonen J, et al. An approach to comprehensive genome and proteome expression analyses in Schwann cells and neurons during peripheral nerve myelin formation. J Neurochem [Internet]. 2016 Sep;138(6):830–44. Available from: http://doi.wiley.com/10.1111/jnc.13722

43. Kusch K, Uecker M, Liepold T, Möbius W, Hoffmann C, Neumann H, et al. Partial Immunoblotting of 2D-Gels: A Novel Method to Identify Post-Translationally Modified Proteins Exemplified for the Myelin Acetylome. Proteomes [Internet]. 2017 Jan 12;5(4):3. Available from: http://www.mdpi.com/2227-7382/5/1/3

44. Neilson KA, Ali NA, Muralidharan S, Mirzaei M, Mariani M, Assadourian G, et al. Less label, more free: Approaches in label-free quantitative mass spectrometry. Proteomics. 2011.

45. Distler U, Kuharev J, Tenzer S. Biomedical applications of ion mobility-enhanced data-independent acquisition-based label-free quantitative proteomics. Expert Rev Proteomics. 2014;

46. Geromanos SJ, Vissers JPC, Silva JC, Dorschel CA, Li GZ, Gorenstein M V., et al. The detection, correlation, and comparison of peptide precursor and product ions from data independent LC-MS with data dependant LC-MS/MS. Proteomics. 2009;

47. Li GZ, Vissers JPC, Silva JC, Golick D, Gorenstein M V., Geromanos SJ. Database searching and accounting of multiplexed precursor and product ion spectra from the data independent analysis of simple and complex peptide mixtures. Proteomics. 2009;

48. Distler U, Kuharev J, Navarro P, Tenzer S. Label-free quantification in ion mobility–enhanced data-independent acquisition proteomics. Nat Protoc [Internet]. 2016 Apr 24;11(4):795–812. Available from: http://www.nature.com/articles/nprot.2016.042

49. Distler U, Kuharev J, Navarro P, Levin Y, Schild H, Tenzer S. Drift time-specific collision energies enable deep-coverage data-independent acquisition proteomics. Nat Methods [Internet]. 2014 Feb 15;11(2):167–70. Available from:

http://www.nature.com/articles/nmeth.2767
50. Larocca JN, Norton WT. Isolation of Myelin. Curr Protoc Cell Biol [Internet]. 2006 Dec;33(1):3.25.1-3.25.19. Available from: http://doi.wiley.com/10.1002/0471143030.cb0325s33
51. Jahn O, Tenzer S, Werner HB. Myelin proteomics: Molecular anatomy of an insulating sheath. Molecular Neurobiology. 2009.
52. Erwig MS, Hesse D, Jung RB, Uecker M, Kusch K, Tenzer S, et al. Myelin: Methods for Purification and Proteome Analysis. In: Methods in Molecular Biology [Internet]. 2019. p. 37–63. Available from: http://link.springer.com/10.1007/978-1-4939-9072-6_3
53. Silva JC, Gorenstein M V., Li G-Z, Vissers JPC, Geromanos SJ. Absolute Quantification of Proteins by LCMS E. Mol Cell Proteomics [Internet]. 2006 Jan;5(1):144–56. Available from: http://www.mcponline.org/lookup/doi/10.1074/mcp.M500230-MCP200
54. Ahrné E, Molzahn L, Glatter T, Schmidt A. Critical assessment of proteome-wide label-free absolute abundance estimation strategies. Proteomics. 2013;
55. Dodds JN, Baker ES. Ion Mobility Spectrometry: Fundamental Concepts, Instrumentation, Applications, and the Road Ahead. J Am Soc Mass Spectrom. 2019;
56. Micko S, Schlaepfer WW. PROTEIN COMPOSITION OF AXONS and MYELIN FROM RAT and HUMAN PERIPHERAL NERVES. J Neurochem [Internet]. 1978 May;30(5):1041–9. Available from: http://doi.wiley.com/10.1111/j.1471-4159.1978.tb12397.x
57. Smith ME, Curtis BM. FROG SCIATIC NERVE MYELIN: A CHEMICAL CHARACTERIZATION. J Neurochem [Internet]. 1979 Aug;33(2):447–52. Available from: http://doi.wiley.com/10.1111/j.1471-4159.1979.tb05174.x
58. Whitaker JN. The protein antigens of peripheral nerve myelin. Ann Neurol [Internet]. 1981;9(S1):56–64. Available from: http://doi.wiley.com/10.1002/ana.410090710
59. Gillespie CS, Sherman DL, Blair GE, Brophy PJ. Periaxin, a novel protein of myelinating schwann cells with a possible role in axonal ensheathment. Neuron [Internet]. 1994 Mar;12(3):497–508. Available from: https://linkinghub.elsevier.com/retrieve/pii/0896627394902089
60. Fledrich R, Abdelaal T, Rasch L, Bansal V, Schütza V, Brügger B, et al. Targeting myelin lipid metabolism as a potential therapeutic strategy in a model of CMT1A neuropathy. Nat Commun [Internet]. 2018 Dec 2;9(1):3025. Available from: http://www.nature.com/articles/s41467-018-05420-0
61. Pareyson D, Marchesi C. Diagnosis, natural history, and management of Charcot–Marie–Tooth disease. Lancet Neurol [Internet]. 2009 Jul;8(7):654–67. Available from: https://linkinghub.elsevier.com/retrieve/pii/S1474442209701103
62. Baets J, De Jonghe P, Timmerman V. Recent advances in Charcot–Marie–Tooth disease. Curr Opin Neurol [Internet]. 2014 Oct;27(5):532–40. Available from: http://content.wkhealth.com/linkback/openurl?sid=WKPTLP:landingpage&an=00019052-201410000-00006
63. Brennan KM, Bai Y, Shy ME. Demyelinating CMT–what's known, what's new and what's in store? Neurosci Lett [Internet]. 2015 Jun;596:14–26. Available from: https://linkinghub.elsevier.com/retrieve/pii/S0304394015000725

64. Gillespie CS, Sherman DL, Fleetwood-Walker SM, Cottrell DF, Tait S, Garry EM, et al. Peripheral Demyelination and Neuropathic Pain Behavior in Periaxin-Deficient Mice. Neuron [Internet]. 2000 May;26(2):523–31. Available from: https://linkinghub.elsevier.com/retrieve/pii/S0896627300811848
65. Guilbot A. A mutation in periaxin is responsible for CMT4F, an autosomal recessive form of Charcot-Marie-Tooth disease. Hum Mol Genet [Internet]. 2001 Feb 1;10(4):415–21. Available from: https://academic.oup.com/hmg/article-lookup/doi/10.1093/hmg/10.4.415
66. Berger P, Niemann A, Suter U. Schwann cells and the pathogenesis of inherited motor and sensory neuropathies (Charcot-Marie-Tooth disease). Glia [Internet]. 2006 Sep;54(4):243–57. Available from: http://doi.wiley.com/10.1002/glia.20386
67. Marchesi C, Milani M, Morbin M, Cesani M, Lauria G, Scaioli V, et al. Four novel cases of periaxin-related neuropathy and review of the literature. Neurology [Internet]. 2010 Nov 16;75(20):1830–8. Available from: http://www.neurology.org/cgi/doi/10.1212/WNL.0b013e3181fd6314
68. Philp NJ, Ochrietor JD, Rudoy C, Muramatsu T, Linser PJ. Loss of MCT1, MCT3, and MCT4 Expression in the Retinal Pigment Epithelium and Neural Retina of the 5A11/Basigin-Null Mouse. Investig Opthalmology Vis Sci [Internet]. 2003 Mar 1;44(3):1305. Available from: http://iovs.arvojournals.org/article.aspx?doi=10.1167/iovs.02-0552
69. Patzig J, Kusch K, Fledrich R, Eichel MA, Lüders KA, Möbius W, et al. Proteolipid protein modulates preservation of peripheral axons and premature death when myelin protein zero is lacking. Glia [Internet]. 2016 Jan;64(1):155–74. Available from: http://doi.wiley.com/10.1002/glia.22922
70. Lee Y, Morrison BM, Li Y, Lengacher S, Farah MH, Hoffman PN, et al. Oligodendroglia metabolically support axons and contribute to neurodegeneration. Nature [Internet]. 2012 Jul 11;487(7408):443–8. Available from: http://www.nature.com/articles/nature11314
71. Fünfschilling U, Supplie LM, Mahad D, Boretius S, Saab AS, Edgar J, et al. Glycolytic oligodendrocytes maintain myelin and long-term axonal integrity. Nature [Internet]. 2012 May 29;485(7399):517–21. Available from: http://www.nature.com/articles/nature11007
72. Morrison BM, Tsingalia A, Vidensky S, Lee Y, Jin L, Farah MH, et al. Deficiency in monocarboxylate transporter 1 (MCT1) in mice delays regeneration of peripheral nerves following sciatic nerve crush. Exp Neurol [Internet]. 2015 Jan;263:325–38. Available from: https://linkinghub.elsevier.com/retrieve/pii/S0014488614003549
73. Morrison BM, Lee Y, Rothstein JD. Oligodendroglia: Metabolic supporters of axons. Trends in Cell Biology. 2013.
74. Saab AS, Tzvetanova ID, Nave K-A. The role of myelin and oligodendrocytes in axonal energy metabolism. Curr Opin Neurobiol [Internet]. 2013 Dec;23(6):1065–72. Available from: https://linkinghub.elsevier.com/retrieve/pii/S0959438813001888
75. Rinholm JE, Bergersen LH. White matter lactate – Does it matter? Neuroscience [Internet]. 2014 Sep;276:109–16. Available from: https://linkinghub.elsevier.com/retrieve/pii/S0306452213008464
76. Jha MK, Lee Y, Russell KA, Yang F, Dastgheyb RM, Deme P, et al. Monocarboxylate

transporter 1 in Schwann cells contributes to maintenance of sensory nerve myelination during aging. Glia. 2019;

77. Edgar JM, McLaughlin M, Werner HB, McCulloch MC, Barrie JA, Brown A, et al. Early ultrastructural defects of axons and axon-glia junctions in mice lacking expression of Cnp1. Glia. 2009;

78. Verheijen MHG. Local regulation of fat metabolism in peripheral nerves. Genes Dev [Internet]. 2003 Oct 1;17(19):2450–64. Available from: http://www.genesdev.org/cgi/doi/10.1101/gad.1116203

79. Buchstaller J. Efficient Isolation and Gene Expression Profiling of Small Numbers of Neural Crest Stem Cells and Developing Schwann Cells. J Neurosci [Internet]. 2004 Mar 10;24(10):2357–65. Available from: http://www.jneurosci.org/cgi/doi/10.1523/JNEUROSCI.4083-03.2004

80. D'antonio M, Michalovich D, Paterson M, Droggiti A, Woodhoo A, Mirsky R, et al. Gene profiling and bioinformatic analysis of Schwann cell embryonic development and myelination. Glia [Internet]. 2006 Apr 1;53(5):501–15. Available from: http://doi.wiley.com/10.1002/glia.20309

81. Schaeren-Wiemers N, Bonnet A, Erb M, Erne B, Bartsch U, Kern F, et al. The raft-associated protein MAL is required for maintenance of proper axon–glia interactions in the central nervous system. J Cell Biol [Internet]. 2004 Aug 30;166(5):731–42. Available from: http://www.jcb.org/lookup/doi/10.1083/jcb.200406092

82. Adlkofer K, Martini R, Aguzzi A, Zielasek J, Toyka K V., Suter U. Hypermyelination and demyelinating peripheral neuropathy in Pmp22-deficient mice. Nat Genet [Internet]. 1995 Nov;11(3):274–80. Available from: http://www.nature.com/articles/ng1195-274

83. Riethmacher D, Sonnenberg-Riethmacher E, Brinkmann V, Yamaai T, Lewin GR, Birchmeier C. Severe neuropathies in mice with targeted mutations in the ErbB3 receptor. Nature [Internet]. 1997 Oct;389(6652):725–30. Available from: http://www.nature.com/articles/39593

84. Woldeyesus MT, Britsch S, Riethmacher D, Xu L, Sonnenberg-Riethmacher E, Abou-Rebyeh F, et al. Peripheral nervous system defects in erbB2 mutants following genetic rescue of heart development. Genes Dev [Internet]. 1999 Oct 1;13(19):2538–48. Available from: http://www.genesdev.org/cgi/doi/10.1101/gad.13.19.2538

85. Ackerman SD, Luo R, Poitelon Y, Mogha A, Harty BL, D'Rozario M, et al. GPR56/ADGRG1 regulates development and maintenance of peripheral myelin. J Exp Med [Internet]. 2018 Mar 5;215(3):941–61. Available from: http://www.jem.org/lookup/doi/10.1084/jem.20161714

86. Monk KR, Oshima K, Jors S, Heller S, Talbot WS. Gpr126 is essential for peripheral nerve development and myelination in mammals. Development [Internet]. 2011 Jul 1;138(13):2673–80. Available from: http://dev.biologists.org/cgi/doi/10.1242/dev.062224

87. Monk KR, Naylor SG, Glenn TD, Mercurio S, Perlin JR, Dominguez C, et al. A G Protein-Coupled Receptor Is Essential for Schwann Cells to Initiate Myelination. Science (80- ) [Internet]. 2009 Sep 11;325(5946):1402–5. Available from: http://www.sciencemag.org/cgi/doi/10.1126/science.1173474

88. Kabzinska D, Drac H, Sherman DL, Kostera-Pruszczyk A, Brophy PJ, Kochanski A, et al.

Charcot-Marie-Tooth type 4F disease caused by S399fsx410 mutation in the PRX gene. Neurology [Internet]. 2006 Mar 14;66(5):745–7. Available from: http://www.neurology.org/cgi/doi/10.1212/01.wnl.0000201269.46071.35

89. Baránková L, Šišková D, Hühne K, Vyhnálková E, Sakmaryová I, Bojar M, et al. A 71-nucleotide deletion in the periaxin gene in a Romani patient with early-onset slowly progressive demyelinating CMT. Eur J Neurol [Internet]. 2008 Jun;15(6):548–51. Available from: http://doi.wiley.com/10.1111/j.1468-1331.2008.02104.x

90. Tokunaga S, Hashiguchi A, Yoshimura A, Maeda K, Suzuki T, Haruki H, et al. Late-onset Charcot–Marie–Tooth disease 4F caused by periaxin gene mutation. Neurogenetics [Internet]. 2012 Nov 1;13(4):359–65. Available from: http://link.springer.com/10.1007/s10048-012-0338-5

91. Gallardo E, García A, Ramón C, Maraví E, Infante J, Gastón I, et al. Charcot–Marie–Tooth disease type 2J with MPZ Thr124Met mutation: clinico-electrophysiological and MRI study of a family. J Neurol [Internet]. 2009 Dec 22;256(12):2061–71. Available from: http://link.springer.com/10.1007/s00415-009-5251-y

92. Leal A, Berghoff C, Berghoff M, Rojas-Araya M, Ortiz C, Heuss D, et al. A Costa Rican family affected with Charcot-Marie-Tooth disease due to the myelin protein zero (MPZ) p.Thr124Met mutation shares the Belgian haplotype. Rev Biol Trop [Internet]. 2014 Dec 1;62(4):1285. Available from: http://revistas.ucr.ac.cr/index.php/rbt/article/view/13473

93. Tokuda N, Noto Y, Kitani-Morii F, Hamano A, Kasai T, Shiga K, et al. Parasympathetic Dominant Autonomic Dysfunction in Charcot-Marie-Tooth Disease Type 2J with the *MPZ* Thr124Met Mutation. Intern Med [Internet]. 2015;54(15):1919–22. Available from: https://www.jstage.jst.go.jp/article/internalmedicine/54/15/54_54.4259/_article

94. Duan X, Gu W, Hao Y, Wang R, Wen H, Sun S, et al. A Novel Asp121Asn Mutation of Myelin Protein Zero Is Associated with Late-Onset Axonal Charcot-Marie-Tooth Disease, Hearing Loss and Pupil Abnormalities. Front Aging Neurosci [Internet]. 2016 Sep 22;8. Available from: http://journal.frontiersin.org/Article/10.3389/fnagi.2016.00222/abstract

95. Fabrizi GM, Tamburin S, Cavallaro T, Cabrini I, Ferrarini M, Taioli F, et al. The spectrum of Charcot-Marie-Tooth disease due to myelin protein zero: An electrodiagnostic, nerve ultrasound and histological study. Clin Neurophysiol [Internet]. 2018 Jan;129(1):21–32. Available from: https://linkinghub.elsevier.com/retrieve/pii/S1388245717310854

96. Ambrozkiewicz MC, Schwark M, Kishimoto-Suga M, Borisova E, Hori K, Salazar-Lázaro A, et al. Polarity Acquisition in Cortical Neurons Is Driven by Synergistic Action of Sox9-Regulated Wwp1 and Wwp2 E3 Ubiquitin Ligases and Intronic miR-140. Neuron [Internet]. 2018 Dec;100(5):1097-1115.e15. Available from: https://linkinghub.elsevier.com/retrieve/pii/S0896627318308961

97. Erwig MS, Patzig J, Steyer AM, Dibaj P, Heilmann M, Heilmann I, et al. Anillin facilitates septin assembly to prevent pathological outfoldings of central nervous system myelin. Elife [Internet]. 2019 Jan 23;8. Available from: https://elifesciences.org/articles/43888

98. Kuharev J, Navarro P, Distler U, Jahn O, Tenzer S. In-depth evaluation of software tools for data-independent acquisition based label-free quantification. Proteomics [Internet]. 2015 Sep;15(18):3140–51. Available from: http://doi.wiley.com/10.1002/pmic.201400396

99. Silva JC, Denny R, Dorschel C, Gorenstein M V., Li G-Z, Richardson K, et al. Simultaneous Qualitative and Quantitative Analysis of the Escherichia coli Proteome. Mol Cell Proteomics [Internet]. 2006 Apr;5(4):589–607. Available from: http://www.mcponline.org/lookup/doi/10.1074/mcp.M500321-MCP200
100. Kammers K, Cole RN, Tiengwe C, Ruczinski I. Detecting significant changes in protein abundance. EuPA Open Proteomics [Internet]. 2015 Jun;7:11–9. Available from: https://linkinghub.elsevier.com/retrieve/pii/S2212968515000069
101. Ritchie ME, Phipson B, Wu D, Hu Y, Law CW, Shi W, et al. limma powers differential expression analyses for RNA-sequencing and microarray studies. Nucleic Acids Res [Internet]. 2015 Apr 20;43(7):e47–e47. Available from: http://academic.oup.com/nar/article/43/7/e47/2414268/limma-powers-differential-expression-analyses-for
102. Storey JD. The positive false discovery rate: a Bayesian interpretation and the q -value. Ann Stat [Internet]. 2003 Dec;31(6):2013–35. Available from: http://projecteuclid.org/euclid.aos/1074290335
103. Vizcaíno JA, Csordas A, Del-Toro N, Dianes JA, Griss J, Lavidas I, et al. 2016 update of the PRIDE database and its related tools. Nucleic Acids Res [Internet]. 2016 Jan 4;44(D1):D447–56. Available from: https://academic.oup.com/nar/article-lookup/doi/10.1093/nar/gkv1145
104. Schardt A, Brinkmann BG, Mitkovski M, Sereda MW, Werner HB, Nave K-A. The SNARE protein SNAP-29 interacts with the GTPase Rab3A: Implications for membrane trafficking in myelinating glia. J Neurosci Res [Internet]. 2009 Nov 15;87(15):3465–79. Available from: http://doi.wiley.com/10.1002/jnr.22005
105. de Monasterio-Schrader P, Patzig J, Möbius W, Barrette B, Wagner TL, Kusch K, et al. Uncoupling of neuroinflammation from axonal degeneration in mice lacking the myelin protein tetraspanin-2. Glia. 2013;
106. Jung M, Sommer I, Schachner M, Nave KA. Monoclonal antibody O10 defines a conformationally sensitive cell- surface epitope of proteolipid protein (PLP): Evidence that PLP misfolding underlies dysmyelination in mutant mice. J Neurosci. 1996;16(24):7920–9.
107. Stumpf SK, Berghoff SA, Trevisiol A, Spieth L, Düking T, Schneider L V., et al. Ketogenic diet ameliorates axonal defects and promotes myelination in Pelizaeus–Merzbacher disease. Acta Neuropathol [Internet]. 2019 Jul 27;138(1):147–61. Available from: http://link.springer.com/10.1007/s00401-019-01985-2
108. Archelos JJ, Roggenbuck K, Scheider-Schaulies J, Linington C, Toyka K V., Hartung H-P. Production and characterization of monoclonal antibodies to the extracellular domain of P0. J Neurosci Res [Internet]. 1993 May 1;35(1):46–53. Available from: http://doi.wiley.com/10.1002/jnr.490350107
109. Darbas A, Jaegle M, Walbeehm E, van den Burg H, Driegen S, Broos L, et al. Cell autonomy of the mouse claw paw mutation. Dev Biol [Internet]. 2004 Aug;272(2):470–82. Available from: https://linkinghub.elsevier.com/retrieve/pii/S0012160604003616
110. Catenaccio A, Court FA. Teased Fiber Preparation of Myelinated Nerve Fibers from Peripheral Nerves for Vital Dye Staining and Immunofluorescence Analysis. In: Methods in Molecular

Biology [Internet]. 2018. p. 329–37. Available from: http://link.springer.com/10.1007/978-1-4939-7649-2_21

111. Hulsen T, de Vlieg J, Alkema W. BioVenn – a web application for the comparison and visualization of biological lists using area-proportional Venn diagrams. BMC Genomics [Internet]. 2008;9(1):488. Available from: http://bmcgenomics.biomedcentral.com/articles/10.1186/1471-2164-9-488

## FIGURE LEGENDS

### Figure 1. Proteome analysis of peripheral myelin

**(A)** Schematic illustration of a previous approach to the peripheral myelin proteome (41) compared with the present workflow. Note that the current workflow allows largely automated sample processing and omits labor-intense 2-dimensional differential gel-electrophoresis, thereby considerably reducing hands-on time. Nano LC-MS analysis by data-independent acquisition (DIA) using three different data acquisition modes provides efficient identification and quantification of abundant myelin proteins ($MS^E$; see **Figure 2**), a comprehensive inventory ($UDMS^E$; see **Figures 3-4**) and gel-free differential analysis of hundreds of distinct proteins (DRE-$UDMS^E$; see **Figure 5**). Samples were analyzed in three biological replicates.

**(B)** Immunoblot of myelin biochemically enriched from sciatic nerves of wild-type mice at postnatal day 21 (P21). Equal amounts of corresponding nerve lysate were loaded to compare the abundance of marker proteins for compact myelin (MPZ/P0, MBP, PMP2), non-compact myelin (PRX), the Schwann cell nucleus (KROX20/EGR2), axons (NEFH, KCNA1) and mitochondria (VDAC). Blots show n=2 biological replicates representative of n=3 biological replicates. Note that myelin markers are enriched in purified myelin; other cellular markers are reduced.

**(C)** Number and relative abundance of proteins identified in myelin purified from the sciatic nerves of wild-type mice using three different data acquisition modes ($MS^E$, $UDMS^E$, DRE-$UDMS^E$). Note that $MS^E$ (orange) provides the best information about the relative abundance of high-abundant myelin proteins (dynamic range of more than four orders of magnitude) but identifies comparatively fewer proteins in purified myelin. $UDMS^E$ (blue) identifies the largest number of proteins but provides only a lower dynamic range of about three orders of magnitude. DRE-$UDMS^E$ (green) identifies an intermediate number of proteins with an intermediate dynamic range of about four orders of magnitude. Note that $MS^E$ with very high dynamic range is required for the quantification of the exceptionally abundant myelin protein zero (MPZ/P0), myelin basic protein (MBP) and periaxin (PRX). ppm, parts per million.

**(D)** Venn diagram comparing the number of proteins identified in PNS myelin by $MS^E$, $UDMS^E$ and DRE-$UDMS^E$. Note the high overlap of identified proteins.

**(E)** Venn diagram of the proteins identified in PNS myelin by $UDMS^E$ in this study compared with those identified in two previous approaches (41,42).

### Figure 1-supplement 1. Clustered heatmap of Pearson's correlation coefficients for protein abundance comparing data acquisition modes.

The heatmap compares the $log_2$ transformed ppm protein abundance values to assess peripheral myelin purified from wild type mice using three data acquisition modes ($MS^E$, $UDMS^E$, DRE-$UDMS^E$). The inset shows the color key and the histogram for the values of the correlation coefficients. Note that the runs cluster with a high overall correlation (>0.75) into three conditions defined by the acquisition mode, in agreement with the experimental design. Among the samples analyzed by different acquisition modes, DRE-$UDMS^E$ similarly correlates with both $MS^E$ and $UDMS^E$, reflecting its intermediate nature.

**Figure 2. Relative abundance of peripheral myelin proteins**

$MS^E$ was used to identify and quantify proteins in myelin purified from the sciatic nerves of wild-type mice at P21; their relative abundance is given as percent with relative standard deviation (% +/- RSD). Note that known myelin proteins constitute >80% of the total myelin protein; proteins not previously associated with myelin constitute <20%. Mass spectrometric quantification based on 3 biological replicates per genotype with 4 technical replicates each (see **Figure 1-source data 1**).

**Figure 3. Developmental mRNA abundance profiles of myelin-associated genes**

**(A)** K-means clustering was performed for the mRNA profiles of those 1046 proteins in our myelin proteome inventory for which significant mRNA expression was found by RNA-Seq in the sciatic nerve of rats dissected at ages E21, P6, P18 and 6 months (M6). Note that this filtering strategy allows to selectively display the developmental abundance profiles of those transcripts that encode myelin-associated proteins rather than of all transcripts present in the nerve. Standardized mRNA abundance profiles are shown (n=4 biological replicates per age). Known myelin genes are displayed in red. For comparison, *Pmp22* mRNA was included although the small tetraspan protein PMP22 was not mass spectrometrically identified due to its unfavorable distribution of tryptic cleavage sites. Normalized counts for all mRNAs including those displaying developmentally unchanged abundance are provided in **Figure 3-Source data 1**.

**(B)** Numbers of mRNAs per cluster.

**Figure 4. Categorization of annotated protein functions**

All proteins identified in peripheral myelin by $UDMS^E$ (turquoise) and the respective developmental expression clusters (**Figure 3**; shades of red) were analyzed for overrepresented functional annotations using gene ontology (GO) terms. The graph displays

1182 the percentage of proteins in each cluster that were annotated with a particular function. For
1183 comparison, known myelin proteins were annotated. n.o., not over-represented.
1184
1185
1186 **Figure 5. Molecular analysis of myelin in the *Prx*$^{-/-}$ mouse model of CMT4F**
1187 **(A)** Myelin purified from sciatic nerves dissected from *Prx*$^{-/-}$ and control mice at P21 was
1188 separated by SDS-PAGE (0.5 µg protein load) and proteins were visualized by silver
1189 staining. Bands constituted by the most abundant myelin proteins (MPZ/P0, MBP, PRX) are
1190 annotated. Note that no band constituted by PRX was detected in *Prx*$^{-/-}$ myelin and that
1191 several other bands also display genotype-dependent differences in intensity. Gel shows n=2
1192 biological replicates representative of n=3 biological replicates.
1193 **(B)** The relative abundance of proteins in myelin purified from *Prx*$^{-/-}$ sciatic nerves as
1194 quantified by MS$^{E}$ is given as percent with relative standard deviation (% +/- RSD). Note the
1195 increased relative abundance of MPZ/P0 and MBP compared to wild-type myelin (see
1196 **Figure 2**) when PRX is lacking. Mass spectrometric quantification based on 3 biological
1197 replicates with 4 technical replicates each (see **Figure 5-source data 1**).
1198 **(C,D)** Differential proteome analysis by DRE-UDMS$^{E}$ of myelin purified from *Prx*$^{-/-}$ and wild-
1199 type mice. Mass spectrometric quantification based on 3 biological replicates per genotype
1200 with 4 technical replicates each (see **Figure 5-source data 2**). **(C)** Top 40 proteins of which
1201 the abundance is reduced (blue) or increased (red) in peripheral myelin purified from *Prx*$^{-/-}$
1202 compared to wild-type mice with the highest level of significance according to the -$\log_{10}$
1203 transformed q-value (green). In the heatmaps, each horizontal line corresponds to the fold-
1204 change (FC) of a distinct protein compared to its average abundance in wild-type myelin
1205 plotted on a $\log_2$ color scale. Heatmaps display 12 replicates, i.e. 3 biological replicates per
1206 genotype with 4 technical replicates each. **(D-D‘‘‘)** Volcano plots representing genotype-
1207 dependent quantitative myelin proteome analysis. Data points represent quantified proteins
1208 in *Prx*$^{-/-}$ compared to wild-type myelin and are plotted as the log2-transformed fold-change
1209 (FC) on the x-axis against the -log10-transformed q-value on the y-axis. Stippled lines mark a
1210 -log10-transformed q-value of 1.301, reflecting a q-value of 0.05 as significance threshold.
1211 Highlighted are the datapoints representing the Top 10 proteins displaying highest zdist
1212 values (Euclidean distance between the two points (0,0) and (x,y) with x = log2(FC) and y = -
1213 log10(q-value) (red circles in **D**), immune-related proteins (purple circles in **D‘**), proteins of
1214 the extracellular matrix (ECM; yellow circles in **D‘‘**) and known myelin proteins (blue circles in
1215 **D‘‘‘**). n.d., not detected; n.q., no q-value computable due to protein identification in one
1216 genotype only. Also see **Figure 5-supplement 1.**
1217 **(E)** Immunoblot of myelin purified from *Prx*$^{-/-}$ and control sciatic nerves confirms the reduced
1218 abundance of DRP2, SLC16A1/MCT1, BSG and PMP2 in *Prx*$^{-/-}$ myelin, as found by

differential DRE-UDMS$^{E}$ analysis (in **Figure 5C,D**). PRX was detected as genotype control; PLP/DM20 and ATP1A1 serve as markers. Blot shows n=2 biological replicates per genotype.

**(F)** Teased fiber preparations of sciatic nerves dissected from *Prx*$^{-/-}$ and control mice immunolabelled for MAG (red) and SLC16A1 (green). Note that SLC16A1 co-distributes with MAG in Schmidt-Lanterman incisures (SLI) in control but not in *Prx*$^{-/-}$ nerves, in accordance with the reduced abundance of SLC16A1 in *Prx*$^{-/-}$ myelin (**Figure 5C-E**). Also note that, in *Prx*$^{-/-}$ myelin, SLI were largely undetectable by MAG immunolabeling.

**Figure 5-supplement 1. Clustered heatmap of Pearson's correlation coefficients for protein abundance comparing genotypes.**

**(A)** The heatmap compares the $\log_2$ transformed ppm protein abundance values from the DRE-UDMS$^{E}$ runs to assess peripheral myelin purified from wild type and *Prx*$^{-/-}$ mice. The inset shows the color key and the histogram for the values of the correlation coefficients. Note that the runs cluster with a high overall correlation (>0.85) into two conditions defined by the genotype, in agreement with the experimental design.

**(B)** Volcano plot representing genotype-dependent quantitative myelin proteome analysis. Data points represent quantified proteins in *Prx*$^{-/-}$ compared to wild-type myelin plotted as the log2-transformed fold-change (FC) on the x-axis against the -log10-transformed q-value on the y-axis. Note the different axis scale compared to **Figure 5D**. Stippled line marks a -log10-transformed q-value of 1.301, reflecting a q-value of 0.05 as significance threshold. Highlighted is the datapoint for PRX to illustrate that only trace amounts of PRX were detected when assessing *Prx*$^{-/-}$ myelin. ATP2A1, ATP1A4 and PLCD1 were not detected in *Prx*$^{-/-}$ myelin.

**Figure 6. Progressive loss and reduced diameters of peripheral axons in *Prx*$^{-/-}$ mice**

**(A-D)** Genotype-dependent quantitative assessment of light micrographs of toluidine-stained semi-thin sectioned quadriceps nerve dissected at 2, 4 and 9 months of age reveals progressive loss of peripheral axons in *Prx*$^{-/-}$ compared to control mice.

**(A)** Representative micrographs. Arrows point at myelinated axons; asterisk denotes an unmyelinated axon; arrowhead points at a myelin whorl lacking a recognizable axon. Scale bars, 10 µm.

**(B)** Total number of axons per nerve that are not associated with a Remak bundle.

**(C)** Total number of myelinated axons per nerve.

**(D)** Total number per nerve of myelin whorls that lack a recognizable axon.

Mean +/ SD, n=3-4 mice per genotype and age; *P<0.05, **P<0.01, ***P<0.001 by Student's unpaired t-test.

(**E-G**) Genotype-dependent assessment of myelinated axons shows a shift toward reduced axonal diameters in quadriceps nerves of *Prx*$^{-/-}$ compared to control mice at 2 months **(E)**, 4 months **(F)** and 9 months **(G)** of age. Data are presented as frequency distribution with 0.5 µm bin width. ***, p<0.001 by two-sided Kolmogorow-Smirnow test. For precise p-values see methods section.

**Figure 1-source data 1. Label-free quantification of proteins in wild-type PNS myelin fractions by three different data acquisition modes**

Identification and quantification data of detected myelin-associated proteins. Tryptic peptides derived from four technical replicates (replicate digestion and replicate injection) per three biological replicate (20 sciatic nerves pooled from 10 animals) were analyzed by LC-MS (12 runs in total). Proteins (FDR < 1%; 2 peptides/protein) and peptides (FDR < 1%; ≥7 amino acids) were identified by database search against the UniprotKB/SwissProt mouse database using PLGS. Data were post-processed with the software package ISOQuant to calculate absolute in-sample amounts for each detected protein based on the TOP3 approach. Reported abundance values are defined as the relative amount of each protein in respect to the sum over all detected proteins (ppm: parts per million (w/w) of total protein). Typical contaminant proteins like keratins were filtered.

→ sheet 1: protein identification details

→ sheet 2: WT myelin proteome by MS$^{E}$

→ sheet 3: WT myelin proteome by UD-MS$^{E}$

→ sheet 4: WT myelin proteome by DRE UD-MS$^{E}$

→ sheet 5: 45 proteins additionally identified in WT myelin by 1D-gel-LC-MS

**Figure 3-source data 1. Normalized developmental mRNA abundance data**

→ sheet 1: normalized values for all individual 4 biological replicates per age

→ sheet 2: normalized values for biological replicates averaged to give mean per age

**Figure 5-source data 1. Label-free quantification of proteins in PNS myelin fractions from *Prx*$^{-/-}$ mice by MSe**

Identification and quantification data of detected myelin-associated proteins. Tryptic peptides derived from four technical replicates (replicate digestion and replicate injection) per three

biological replicate (20 sciatic nerves pooled from 10 animals) were analyzed by LC-MS (12 runs in total). Proteins (FDR < 1%; 2 peptides/protein) and peptides (FDR < 1%; ≥7 amino acids) were identified by database search against the UniprotKB/SwissProt mouse database using PLGS. Data were post-processed with the software package ISOQuant to calculate absolute in-sample amounts for each detected protein based on the TOP3 approach. Reported abundance values are defined as the relative amount of each protein in respect to the sum over all detected proteins (ppm: parts per million (w/w) of total protein). Typical contaminant proteins like keratins were filtered.

→ sheet 1: protein identification details

→ sheet 2: *Prx*$^{-/-}$ myelin proteome by MS$^{E}$

**Figure 5-source data 2. Label-free quantification of proteins in PNS myelin fractions from WT and *Prx*$^{-/-}$ mice by DRE-UDMSe**

Identification and quantification data of detected myelin-associated proteins by DRE-UDMSe. For each genotype, tryptic peptides derived from four technical replicates (replicate digestion and replicate injection) per three biological replicate (20 sciatic nerves pooled from 10 animals) were analyzed by LC-MS (24 runs in total). Proteins (FDR < 1%; 2 peptides/protein) and peptides (FDR < 1%; ≥7 amino acids) were identified by database search against the UniprotKB/SwissProt mouse database using PLGS. Data were post-processed with the software package ISOQuant to calculate absolute in-sample amounts for each detected protein based on the TOP3 approach. Reported abundance values are defined as the relative amount of each protein in respect to the sum over all detected proteins (ppm: parts per million (w/w) of total protein). Typical contaminant proteins like keratins were filtered. The -log10-transformed q-value was plotted against the log2-transformed fold change to obtain the volcano plot shown in Figure 5D. As no imputation of missing values was performed, proteins exclusive for only one of the conditions do not appear in the volcano plot, but are appended at the end of the list. Criteria for statistically significant regulation were as follows: fold change of at least 1.5 and q-value below 0.05.

→ sheet 1: protein identification details

→ sheet 2: comparison of WT vs. *Prx*$^{-/-}$ myelin proteome by DRE-UDMS$^{E}$

| Protein name | Gene | Reference | TMD | Cluster |
|---|---|---|---|---|
| 2-hydroxyacylsphingosine 1-beta-galactosyltransferase | *Ugt8* | Bosio et al., 1996 | 2 | P6-up |
| Syntrophin α1 | *Snta1* | Fuhrmann-Stroissnigg et al., 2012 | - | P18-up |
| Annexin A2 | *Anxa2* | Hayashi et al., 2007 | - | Descending |
| Band 4.1 protein B / 4.1B | *Epb41l3* | Ivanovic et al., 2012 | - | Descending |
| Band 4.1 protein G / 4.1G | *Epb41l2* | Ohno et al., 2006 | - | P6-up |
| Breast carcinoma-amplified sequence 1 | *Bcas1* | Ishimoto et al., 2017 | - | P6-up |
| Cadherin 1/ E-Cadherin | *Cdh1* | Fannon et al., 1995 | 1 | P18-up |
| Carbonic anhydrase 2 | *Ca2* | Cammer et al., 1987 | - | Descending |
| Catenin α1 | *Ctnna1* | Murata et al., 2006 | - | U-shaped |
| Catenin ß1 | *Ctnnb1* | Fannon et al., 1995 | - | Descending |
| Caveolin 1 | *Cav1* | Mikol et al., 2002 | 1 | P18-up |
| CD9, tetraspanin 29 | *Cd9* | Ishibashi et al., 2004 | 4 | P18-p |
| CD59A | *Cd59a* | Funabashi et al., 1994 | 1 | P18-up |
| CD47, integrin-associated signal transducer | *Cd47* | Gitik et al., 2011 | 5 | P6-up |
| CD81, tetraspanin 28 | *Cd81* | Ishibashi et al., 2004 | 4 | P18-up |
| CD82, tetraspanin 27 | *Cd82* | Chernousov et al., 2013 | 4 | P18-up |
| CD151, tetraspanin 24 | *Cd151* | Patzig et al., 2011 | 4 | P18-up |
| Cell adhesion molecule 4/ NECL4 | *Cadm4* | Spiegel et al., 2007 | 1 | P6-up |
| Cell division control protein 42 | *Cdc42* | Benninger et al., 2007 | - | P6-up |
| Cell surface glycoprotein MUC18 | *Mcam* | Shi et al., 1998 | 1 | Descending |
| Ciliary neurotrophic factor | *Cntf* | Rende et al., 1992 | - | Late-up |
| CKLF-like MARVEL TMD-containing 5 | *Cmtm5* | Patzig et al., 2011 | 4 | P6-up |
| Claudin-19 | *Cldn19* | Miyamoto et al., 2005 | 4 | P6-up |
| Cofilin 1 | *Cfl1* | Sparrow et al., 2012 | - | Descending |
| Crystallin α2 | *Cryab* | d'Antonio et al., 2006 | - | P18-up |
| Cyclic nucleotide phosphodiesterase | *Cnp* | Matthieu et al., 1980 | - | P6-up |
| Sarcoglycan δ | *Sgcd* | Cai et al., 2007 | 1 | Late-up |
| Dihydropyrimidinase related protein 1 | *Crmp1* | d'Antonio et al., 2006 | - | Descending |
| Disks large homolog 1 | *Dlg1* | Cotter et al., 2010 | - | Descending |
| Dynein light chain 1 | *Dynll1* | Myllykoski et al. 2018 | - | P6-up |
| Dystroglycan | *Dag1* | Yamada et al, 1994 | 1 | P6-up |
| Dystrophin/DP116 | *Dmd* | Cai et al., 2007 | - | P6-up |
| Dystrophin-related protein 2 | *Drp2* | Sherman et al., 2001 | - | P18-up |
| E3 ubiquitin-protein ligase NEDD4 | *Nedd4* | Liu et al., 2009 | - | Descending |
| Ezrin | *Ezr* | Scherer et al., 2001 | - | P6-up |
| Fatty acid synthase | *Fasn* | Salles et al., 2002 | - | P6-up |
| Flotillin 1 | *Flot1* | Lee et al., 2014 | - | P18-up |
| Gap junction ß1 protein / Cx32 | *Gjb1* | Li et al., 2002 | 4 | P18-up |
| Gap junction γ3 protein / Cx29 | *Gjc3* | Li et al., 2002 | 1 | P6-up |
| Gelsolin | *Gsn* | Gonçalves et al., 2010 | - | Late-up |
| Glycogen synthase kinase 3ß | *Gsk3b* | Ogata et al., 2004 | - | P6-up |
| Integrin α6 | *Itga6* | Nodari et al., 2008 | 1 | P6-up |
| Integrin αV | *Itgav* | Chernousov & Carey, 2003 | 1 | Descending |
| Integrin ß1 | *Itgb1* | Feltri et al., 2002 | 1 | Descending |
| Integrin ß4 | *Itgb4* | Quattrini et al., 1996 | 2 | P18-up |
| Junctional adhesion molecule C | *Jam3* | Scheiermann et al., 2007 | 1 | P18-up |
| Laminin α2 | *Lama2* | Yang et al., 2005 | - | P6-up |
| Laminin α4 | *Lama4* | Yang et al., 2005 | - | Descending |
| Laminin ß1 | *Lamb1* | LeBeau et al., 1994 | - | Descending |
| Laminin ß2 | *Lamb2* | LeBeau et al., 1994 | - | P18-up |
| Laminin γ1 | *Lamc1* | Chen & Strickland, 2003 | - | Descending |
| Membrane Palmitoylated Protein 6 | *Mpp6* | Saitoh et al., 2019 | - | P6-up |
| Microtubule-associated protein 1A | *Map1a* | Fuhrmann-Stroissnigg et al., 2012 | - | P18-up |
| Microtubule-associated protein 1B | *Map1b* | Fuhrmann-Stroissnigg et al., 2012 | - | P6-up |
| Mitogen-activated protein kinase 1/ ERK2 | *Mapk1* | Mantuano et al., 2015 | - | Descending |
| Mitogen-activated protein kinase 3/ ERK1 | *Mapk3* | Mantuano et al., 2015 | - | P18-up |
| Moesin | *Msn* | Scherer et al., 2001 | - | Unchanged |
| Monocarboxylate transporter 1 | *Slc16a1* | Domenech-Estevez et al., 2015 | 11 | P18-up |

| | | | | |
|---|---|---|---|---|
| Myelin associated glycoprotein | *Mag* | Figlewicz et al., 1981 | 1 | P6-up |
| Myelin basic protein | *Mbp* | Boggs, 2006 | - | P6-up |
| Myelin protein 2 | *Pmp2* | Trapp et al., 1984 | - | P18-up |
| Myelin protein zero/ P0 | *Mpz* | Giese et al., 1992 | 1 | P6-up |
| Myelin proteolipid protein | *Plp1* | Garbern et al., 1997 | 4 | P6-up |
| Myotubularin-related protein 2 | *Mtmr2* | Bolino et al., 2004 | - | P6-up |
| Noncompact myelin-associated protein | *Ncmap* | Ryu et al., 2008 | 1 | P18-up |
| NDRG1, N-myc downstream regulated | *Ndrg1* | Berger et al., 2004 | - | P18-uP |
| Neurofascin | *Nfasc* | Tait et al., 2000 | 2 | P18-up |
| Nidogen 1 | *Nid1* | Lee et al., 2007 | - | Descending |
| P2X purinoceptor 7 | *P2rx7* | Faroni et al., 2014 | - | P6-up |
| Paxillin | *Pxn* | Fernandez-Valle et al., 2002 | - | P6-up |
| Periaxin | *Prx* | Gillespie et al., 1994 | - | P6-up |
| Plasmolipin | *Pllp* | Bosse et al., 2003 | 4 | P18-up |
| Profilin 1 | *Pfn1* | Montani et al., 2014 | - | Descending |
| Lin-7 homolog C | *Lin7c* | Saitoh et al., 2017 | - | P6-up |
| Rac1 | *Rac1* | Benninger et al., 2007 | - | U-Shaped |
| Radixin | *Rdx* | Scherer et al., 2001 | - | Descending |
| RhoA | *Rhoa* | Brancolini et al., 1999 | - | U-Shaped |
| Septin 2 | *Sept 2* | Buser et al., 2009 | - | Descending |
| Septin 7 | *Sept 7* | Buser et al., 2009 | - | U-Shaped |
| Septin 8 | *Sept 8* | Patzig et al., 2011 | - | P18-up |
| Septin 9 | *Sept 9* | Patzig et al., 2011 | - | P6-up |
| Septin 11 | *Sept 11* | Buser et al., 2009 | - | Descending |
| Sirtuin 2, NAD-dependent deacetylase | *Sirt2* | Werner et al., 2007 | - | P18-up |
| Spectrin alpha chain, non-erythrocytic 1 | *Sptan1* | Susuki et al., 2018 | - | P18-up |
| Spectrin beta chain, non-erythrocytic 1 | *Sptbn1* | Susuki et al., 2018 | - | P18-up |
| Tight junction protein ZO-1 | *Tjp1* | Poliak et al., 2007 | - | P6-up |
| Tight junction protein ZO-2 | *Tjp2* | Poliak et al., 2007 | - | P6-up |
| Transferrin | *Tf* | Liu et al., 1990 | 2 | Late-up |
| Vimentin | *Vim* | Triolo et al., 2012 | - | Unchanged |
| Vinculin | *Vcl* | Beppu et al., 2015 | - | Descending |

**Table 1. Known myelin proteins in the myelin proteome.** Proteins mass-spectrometrically identified in peripheral myelin are compiled according to availability of prior references as myelin proteins. Given are the official gene name, one selected reference, the number of transmembrane domains (TMD) and the mRNA abundance profile cluster (see **Figure 3**).

| Protein name | Gene name | OMIM# | Gene Locus | Neuropathy |
|---|---|---|---|---|
| Monoacylglycerol lipase ABHD12 | *ABHD12* | 613599 | 20p11.21 | PHARC |
| Apoptosis-inducing factor 1 | *AIFM1* | 300169 | Xq26.1 | CMTX4, DFNX5 |
| Na+/K+ -transporting ATPase α1 | *ATP1A1* | 182310 | 1p13.1 | CMT2DD |
| Cytochrome c oxidase subunit 6A1 | *COX6A1* | 602072 | 12q24.31 | CMTRID |
| Dystrophin-related protein 2 | *DRP2* | 300052 | Xq22.1 | CMTX |
| Dynactin subunit 1 | *DCTN1* | 601143 | 2p13.1 | DHMN7B |
| Dynamin 2 | *DNM2* | 602378 | 19p13.2 | CMT2M, CMTDIB |
| Cytoplasmic dynein 1 heavy chain 1 | *DYNC1H1* | 600112 | 14q32.31 | CMT20, SMALED1 |
| E3 SUMO-protein ligase | *EGR2* | 129010 | 10q21.3 | CMT1D, CMT3, CMT4E |
| Glycine-tRNA ligase | *GARS* (Gart) | 600287 | 7p14.3 | CMT2D, HMN5A |
| Gap junction ß1 protein / Cx32 | *GJB1* | 304040 | Xq13.1 | CMTX1 |
| Guanine nucleotide-binding protein ß4 | *GNB4* | 610863 | 3q26.33 | CMTDIF |
| Histidine triad nucleotide-binding protein 1 | *HINT1* | 601314 | 5q23.3 | NMAN |
| Hexokinase 1 | *HK1* | 142600 | 10q22.1 | CMT4G |
| Heat shock protein ß1 | *HSPB1* | 602195 | 7q11.23 | CMT2F, DHMN2B |
| Kinesin heavy chain isoform 5A | *KIF5A* | 602821 | 12q13.3 | SPG10 |
| Prelamin A/C | *LMNA* | 150330 | 1q22 | CMT2B1 |
| Neprilysin | *MME* | 120520 | 3q25.2 | CMT2T, SCA43 |
| Myelin protein zero/ P0 | *MPZ* | 159440 | 1q23.3 | CHN2,CMT1B, CMT2I, CMT2J,CMT3, CMTDID, Roussy-Levy syndrome |
| Myotubularin-related protein 2 | *MTMR2* | 603557 | 11q21 | CMT4B1 |
| Alpha-N-acetylglucosaminidase | *NAGLU* (NAGA) | 609701 | 17q21.2 | CMT2V |
| NDRG1, N-myc downstream regulated | *NDRG1* | 605262 | 8q24.22 | CMT4D |
| Neurofilament heavy polypeptide | *NEFH* | 162230 | 22q12.2 | CMT2CC |
| Neurofilament light polypeptide | *NEFL* | 162280 | 8p21.2 | CMT2E, CMT1F, CMTDIG |
| Peripheral myelin protein 2 | *PMP2* | 170715 | 8q21.13 | CMT1G |
| Peripheral myelin protein 22 | *PMP22* | 601907 | 17p12 | CMT1A, CMT1E, CMT3, HNPP, Roussy-Levy syndrome |
| Ribose-phosphate pyrophosphokinase 1 | *PRPS1* | 311850 | Xq22.3 | Arts syndrome, CMTX5, DFNX1 |
| Periaxin | *PRX* | 605725 | 19q13.2 | CMT4F, CMT3 |
| Ras-related protein Rab 7a | *RAB7A* | 602298 | 3q21.3 | CMT2B |
| Septin 9 | *SEPT9* | 604061 | 17q25.3 | HNA |
| Transitional ER-ATPase | *VCP* | 601023 | 9p13.3 | CMT2Y |
| Tryptophan-tRNA ligase, cytoplasmic | *WARS* | 191050 | 14q32.32 | HMN9 |
| Tyrosine-tRNA ligase, cytoplasmic | *YARS* | 603623 | 1p35.1 | DI-CMTC |

**Table 2. Peripheral myelin proteins identified in PNS myelin involved in neuropathological diseases.** Proteins massspectrometically identified in peripheral myelin were analyzed regarding the involvement of the ortholog human gene in neuropathological diseases. PMP22 was added, though it was not identified by MS analyses due to its unfavorable distribution of tryptic cleavage sites. CMT, Charcot-Marie-Tooth disease; DHMN, distal hereditary motor neuropathy; DI-CMTC, dominant intermediate CMTC; DFN, X-linked deafness; HMN, hereditary motor neuropathy; HSAN, hereditary sensory and autonomic neuropathy; HNA, hereditary sensory and autonomic neuropathy; OMIM, Online Mendelian Inheritance in Man; PHARC, polyneuropathy, hearing loss, ataxia, retinitis pigmentosa and cataract; SCA, spinocerebellar ataxia; SPG, spastic paraplegia.